UCLouvain

École polytechnique de Louvain

Metamaterial antennas for medical imaging

Authors: **Thomas Clerbois, Antoine Rampelbergh**
Supervisors: **Christophe Craeye, Farzad Jabbari Gargari**
Readers: **Redha Abdeddaim, Dimitri Lederer**
Academic year 2021–2022
Master [120] in Electrical Engineering

Acknowledgements

This master thesis is the accomplishment of our journey at the Ecole Polytechnique de Louvain. During the master thesis, as has been the case during the past years, we have always found an open door at the EPL to receive advice and deeper explanation. We would like to thank each member of the EPL for the help and knowledge offered to us.

More specifically, we would like to express our deepest gratitude to our supervisor, Prof. Christophe Craeye, for his guidance, the sharing of his intuitions, and his deep explanation of the diverse topics. We have benefited considerably from his extensive knowledge and previous work on communication and medical antennas.

We are deeply indebted to Farzad Jabbari Gargari for his permanent availability, his advice, his explanation of the MoM code, and the different Birdcages he has designed. We could not have undertaken this journey without his expertise and dedication to the M-One Project. We wish him the best for his Ph.D. and the continuation of the project.

Many thanks to Chan-Sun Park for his explanation of the octree and the optimization step of the MoM code.

We are also thankful to Xavier Dardenne and Xavier Radu, their Ph.D. theses were the base of our thesis.

We would like to extend our sincere thanks to the members of the Jury, Prof. Redha Abdeddaim and Prof. Dimitri Lederer, for taking the time to read this thesis, give constructive criticism about it, and participate in the final presentation.

We warmly thank our extraordinary families for their support from the first to the last day of our studies. The journey to becoming an engineer is challenging, we could never have done it without them, and words cannot express our gratitude to them.

Finally, we would like to express our deepest appreciation to Prof. Claude Oestges for his kindness, his permanent availability, and for the numerous encouragements he gave us during our Bachelor's and Master's degrees.

Abstract

Nuclei's magnetic properties are the basis for Nuclear Magnetic Resonance (NMR). The properties of subatomic particles are determined by quantum physics. The medical use of NMR is referred to as Magnetic Resonance Imaging (MRI). Innovations such as this have proven to be essential and extremely useful in the medical field.

When applying NMR, RF coils are needed. The choice of these RF coils and their design is essential if a quality image is expected. In the case of Birdcages, volume coils are generally used as transceiver coils. However, surface coils have been used as receiver coils, especially at UHF MRI. Over the past 30 years, since the invention of the Birdcage, the literature shows a huge number of variants of the basic model known as the conventional Birdcage. These variants were designed to solve specific problems. There are however several issues that could be solved going back to the conventional Birdcage: (i) The non-central location of the region of interest (ROI) (ii) The increase in homogeneity in this ROI. To this day, little literature provides numerical and experimental data on these subjects. The medical world has stated its interest, and therefore this thesis aims to provide more insights into the possibilities offered by the Birdcage.

In order to define the ROI and the desired field, Gaussian distributed weight matrices are used. Therefore, different versions of Gaussians as well as their specific definition are presented. To the authors' knowledge, such analysis has never been proposed before. A Method of Moments (MoM) based numerical simulation code is adapted to incorporate and take into account the weight matrix. Its main goal is to simulate and optimize the components value of the Birdcage in order to increase the homogeneity in the ROI. Based on the results, a more complex and concrete medical application of the approach, Functional imaging, is presented. The interest not only in the homogeneity but also in the shape of the fields leads to the introduction of a new metric and possibilities.

Nomenclature

Abbreviations

ADC	Analog-to-digital converter
CT-scan	Computerized Tomography scan
DNG	Double negative materials
FID	Free Induction Decay
HP	High pass
LHMs	Left-Handed Materials
LP	Low pass
M-One	Metamaterial head coil for ultra- high field MR
MoM	Method of Moments
MRI	Magnetic Resonance Imaging
NIMS	Negative-index materials
NMR	Nuclear Magnetic Resonance
PET-scan	Positron Emission Tomography scan
RF	Radio frequency
ROA	Region of all
ROI	Region of interest
SAR	Specific absorption rate
SD	Standard deviation

SNR	Signal-to-noise ratio
SRR	Split-ring resonators
UHF	Ultra-High Field

Mathematical and physical abbreviations

ϵ	Permittivity
μ	Permeability
μ_m	Magnetic moment
ω_0	Resonance frequency
σ	Conductivity
φ	Azimuthal angle
B_0	External magnetic field
B_1	Polarized magnetic field
D_e	Distance between the edge of the brain and the center of the torus
f_0	Larmor frequency
G	Magnetic field gradient
M_0	Magnetization
M_z	Longitudinal magnetization
M_{xy}	Transverse magnetization
N_l	Number of legs of the Birdcage
w	Weight
a	Attenuation factor
C	Capacitor
CBC	Connected Birdcage
dB	Decibel

E	Electric field
F	Frequency
h	Planck's constant
I	Spin quantum number
J	Surface current
k	Boltzmann's constant
L	Self-Inductance
l	Length
M	Mutual inductance
N	Number of points inside the mesh
n	Refractive index
p	Point
S	S-parameters
V	Volume
W	Weight matrix
w	Width
Z	Impedance Matrix

Units

cm	Centimeter
F	Farad
Hz	Hertz
Kg	Kilogram
m	Meter
MHz	Megahertz

S	Siemens
T	Tesla
V	Volt
W	Watt

Contents

Acknowledgements i

Abstract ii

Nomenclature iii

1 Introduction 1
- 1.1 Context . . . 1
- 1.2 Expectations of the medical sector . . . 2
- 1.3 Research issues and objectives . . . 2
- 1.4 Metamaterials . . . 5
  - 1.4.1 Definition . . . 5
  - 1.4.2 Realization of Unusual Material Characteristics . . . 5
  - 1.4.3 Applications of metamaterials . . . 6
- 1.5 MRI . . . 7
  - 1.5.1 Nuclear Magnetic Resonance . . . 7
  - 1.5.2 Magnetic Resonance Imaging . . . 10
  - 1.5.3 Ultra-high field MRI . . . 12
  - 1.5.4 Principle of Functional imaging . . . 13
- 1.6 Basic Birdcage design . . . 13
  - 1.6.1 Surface coils . . . 13
  - 1.6.2 Volume coils . . . 14
  - 1.6.3 Performance assessment . . . 15
  - 1.6.4 Birdcage principle and design . . . 15
  - 1.6.5 Electrical representation of a Birdcage . . . 16
  - 1.6.6 Impact of dimensions . . . 17
- 1.7 Structure of the thesis . . . 18

2 Methodology 20
- 2.1 Global approach . . . 20
- 2.2 Design in GMSH . . . 20

2.3 Weight matrix . . . 21
2.3.1 Gaussian . . . 22
2.3.2 Octree . . . 25
2.4 MoM code . . . 27
2.4.1 Method of Moments . . . 27
2.4.2 Surface equivalent and fields equivalent principle for dielectric material . . . 29
2.4.3 Optimization . . . 30
2.4.4 Open circuit pattern . . . 30
2.5 Weighted SD and other metrics . . . 32
2.5.1 Normalized standard deviation . . . 32
2.5.2 Weighted standard deviation . . . 32
2.5.3 Normalized field difference . . . 33
2.5.4 Hybrid weighted difference . . . 34
2.5.5 Comparison of results . . . 34
2.6 Symmetry . . . 34
2.7 Verification using S-parameters . . . 36

3 Weight matrix used on the Conventional Birdcage 38
3.1 8-legged Conventional Birdcage . . . 39
3.2 Symmetric case . . . 40
3.2.1 Basic symmetric case . . . 40
3.2.2 Analysis of the Torus-shaped weight matrix case . . . 42
3.2.3 Conclusion . . . 49
3.3 Asymmetric case . . . 50
3.3.1 Basic asymmetric case . . . 50
3.3.2 Analysis of the Torus-shaped weight matrix case . . . 53
3.3.3 Analysis of the first Gaussian weight matrix case . . . 59
3.3.4 Analysis of the Second Gaussian weight matrix case . . . 65
3.3.5 Analysis of the third Gaussian weight matrix case . . . 70
3.3.6 Conclusion - Comparison between cases . . . 75

4 Functional Imaging 77
4.1 Introduction . . . 77
4.2 Low and high inflow regions . . . 77
4.3 Shape of the field . . . 79
4.4 Analysis of ellipse-shaped weight matrix . . . 80
4.5 Analysis of Region 1 . . . 83
4.6 Analysis of Region 2 . . . 85
4.7 Conclusion . . . 88

5 Connected Birdcage **89**
5.1 Introduction 89
5.2 Connected Birdcage 89
5.3 Analysis of the weight matrix on a Connected Birdcage 90
5.3.1 Basic symmetric case 90
5.3.2 Analysis of the Torus-shaped weight matrix case 92
5.3.3 Conclusion 95

6 Conclusions and perspectives **96**

Appendices **97**

A Simplified electrical representation of a Birdcage **99**

B Transmission line-based approach **103**

Bibliography **105**

Chapter 1

Introduction

1.1 Context

Medical imaging dates back to 1895 with Wilhelm Conrad Röntgen's picture of his wife's hand. It has evolved with several types of imaging processes involved in a variety of medical applications. These range not only from radiology to neurology, but also dentistry or gynecology. Each of these applications has a specific method best suited for it. Some of those methods include ionizing radiation (X-ray or CT-scans), radiotracers like PET-scans, soundwaves (Ultrasound), or magnetic waves in Magnetic Resonance Imaging, more commonly referred to as MRI. The latter relies on the phenomenon of Nuclear Magnetic Resonance (NMR) discovered in 1946 and mainly used by chemists and physicists. It was however quickly adapted to be used in the medical world for various applications. The first use of NMR in medical imaging came thirty years later, resulting in the first (medical) image of a human using MRI. Innovations such as this have proven to be essential and extremely useful in the medical field.

Whatever the application, the basic physical principle can be summarized as follows: a strong magnetic field and radio waves are used to polarize and tilt respectively the nuclei of the hydrogen atoms inside the human body. The non-ionizing radiation created is used as a non-invasive method to obtain medical images. The magnetic field is created by the surface or volume radio frequency (RF) coils. The most famous volume coil is the Birdcage coil, which was invented by Cecil Hayes in 1985. The Birdcage coil has been used in the human body and mainly in head imaging since it could provide a very homogeneous magnetic field distribution inside its volume. This thesis focuses on its usage for the brain. Different designs with different power levels (0.5T-11.7T) have been presented over the years.

M-One This Master thesis was realized in parallel with the European M-One (Metamaterial head coil for ultra- high field MRI) project [28]. This project gathers different universities and commercial partners from all over Europe. The different teams of experts and physicists working in the cutting-edge domain of electrodynamic-metamaterials are working together to solve fundamental issues in ultra-high field (UHF) MRI.

1.2 Expectations of the medical sector

The use of medical imaging is well established in the medical world. However, there is room for various improvements to address persistent problems. The designation and homogenization of certain regions of interest (ROI) is one of them. The use of the Birdcage design and Metamaterial antennae is a major asset in this approach. The ability to define precise areas of homogeneity opens the door to many future applications. One of them is Functional imaging. In this application, the shape of the field is of interest to focus on localised regions. Localised improved homogeneity helps analyzing local activity in the brain. A deeper explanation of Functional imaging can be found in section 1.5.4.

1.3 Research issues and objectives

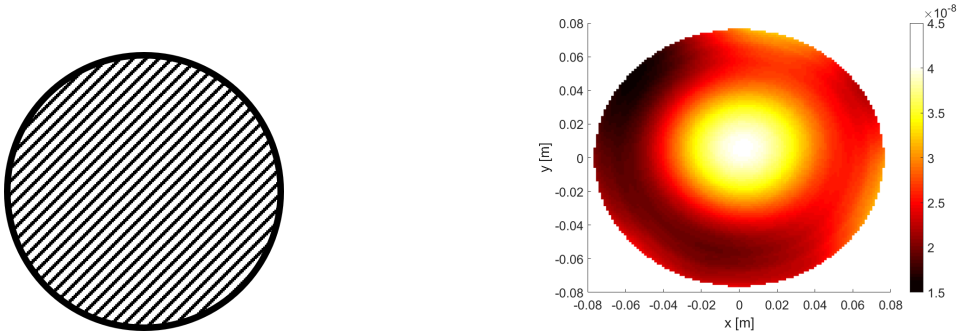
Over the past 30 years, since the invention of the Birdcage, the literature shows a huge number of variants of the basic model known as the conventional Birdcage. These variants were designed to solve specific problems. Several methods like parallel transmission, dielectric pads, and HMA method have been used to improve the homogeneity at UHF MRI [29] [52] [12]. However, the conventional Birdcage reaches its limits. This thesis focuses on the realization of:

- The non-central location of the region of interest (ROI).
- The increase in homogeneity in this ROI.

At this point, very few papers provide numerical and experimental data on these subjects. The medical world has stated its interest, and therefore this thesis aims to provide more insight into the possibilities offered by the Birdcage.

For now, a Method of Moments (MoM) code was provided by the members of the M-one project of UCLouvain that improves the homogeneity of the Birdcage. This code takes as parameters the characteristics of the Birdcage such as its dimensions, the location of the components and the simulation frequency. Component values are selected by the code and the resulting fields are computed. The optimization

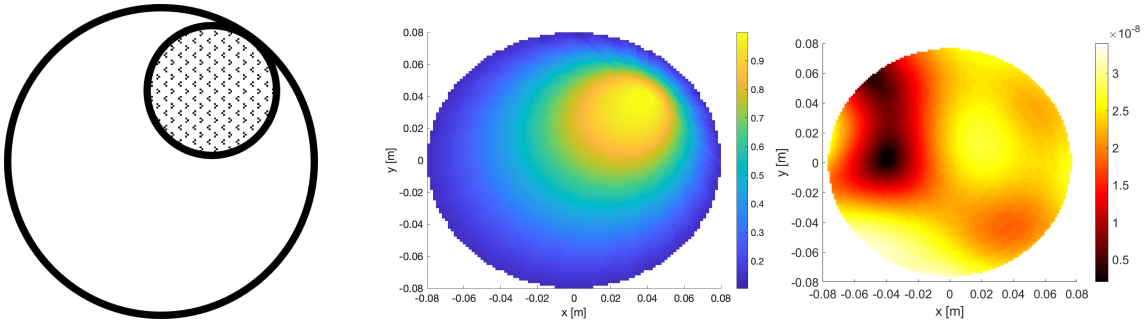
step of the code selects the components giving the best homogeneity, assessed as the normalized standard deviation (SD). Figure 1.1 shows the basic case, as it is used before this thesis. The code will optimize the homogeneity in the whole brain, represented by a phantom shown in Figure 1.1a. The obtained field is shown in Figure 1.1b. Despite the complexity, this case is considered as a basic case in this thesis. This code is the basis of the thesis and will be modified to achieve the objectives.



(a) Phantom (b) Obtained field

Figure 1.1: Basic use of MoM code

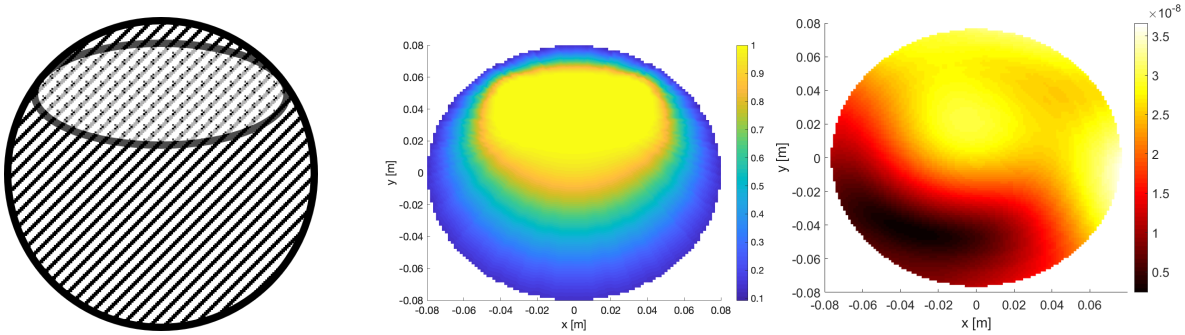
The first objective of the thesis is to define a region in which the homogeneity must be optimal. This way the conventional Birdcage can be adapted and optimized to be able to fit the homogeneity field to an objective distribution defined by weight matrices. The definition of those regions of interest will be first applied to a symmetric Birdcage and an asymmetric Birdcage afterwards. This new input tells the code which part of the phantom should have the best homogeneity when selecting the optimal case. The use of weight matrices is an intuitive way to give more weight or importance to those regions. Since the homogeneity will be multiplied by the weight matrix in the objective function, a high weight imposes a high homogeneity. An example case is shown in Figure 1.2. The ROI is well translated by the weight matrix since the higher weights are located in the ROI (yellow region). This weight matrix has a great impact on the fields since the field looks more homogeneous in the ROI. In fact the measurement of the magnetic field in the ROI is between 2.4 and 2.8 $10^{-8}\left[\frac{T}{\sqrt{W/Kg}}\right]$ which is a smaller gap than in the basic case. A more mathematical approach and a deeper explanation of the results will be presented in the thesis but this example introduces the expected results.



(a) ROI in phantom (b) Weight matrix (c) Obtained field

Figure 1.2: First objective

The second goal of this thesis will be to apply the results of the first step to more concrete examples. This part of the thesis will be a first approach towards the use of the localized ROI in functional imaging and will introduce the notion of "shape" of a field. Indeed, a desired field shape is now pursuit. In a similar way as for the first objective, and based on the difference between the obtained and desired field, the code is slightly adapted. The desired field is also described using weight matrices. Nevertheless, it defines the desired shape of the field in the whole phantom and not only a favored region. The normalization of both the desired and obtained field are needed for a meaningful comparison. Figure 1.3 shows an example of the use of a weight matrix to define a field with an ellipse-shaped area distinguishable. The obtained field is shown in Figure 1.3c and gets closer to the shape of the desired field compared to the basic case.



(a) Shape of field (b) Weight matrix (c) Obtained field

Figure 1.3: Second objective

1.4 Metamaterials

1.4.1 Definition

Technological and scientific areas are more and more involved in the use of Metamaterials and the different opportunities they offer. As explained in [10], metamaterials are artificial materials with electromagnetic properties that are not observed:

- in the constituent materials, and/or
- in nature.

The original idea of metamaterials however refers to the so-called left-handed materials (LHMs) or negative-index materials (NIMS) [10]. The negative (refractive) index brings us back to the basic concepts of optical physics [10] [43]. The refractive index n describes refraction or the bending of the path of waves in a material, characterized by a change in speed and wavelength of the waves. Besides the refractive index (n), a material is also defined by Z, its impedance. Z is the ratio of the transverse components of the electric and magnetic fields in this material. Besides this optical point of view, a better suited definition of this refractive index n can be found in the electromagnetic area. In this case it is expressed in terms of the permittivity ϵ which is the response of a medium to an electric field, and the permeability μ which is the response to a magnetic field [10]:

$$n = \sqrt{\epsilon\mu} \text{ with } \epsilon > 0 \text{ and } \mu > 0 \tag{1.1}$$

Coming back the definition above for metamaterials, it is expected to have negative indexes for both the permittivity and permeability. However, this contradicts common values found in nature that are in general greater than or equal to 1. The feasibility to have a negative permittivity and a negative permeability simultaneously was first studied and demonstrated in 1968 by Veselago [50].

1.4.2 Realization of Unusual Material Characteristics

Until 1999, it was not physically possible to realize a material with simultaneously negative permittivity and permeability. [40]

Negative Permittivity J.B. Pendry was the first researcher who published a paper about the realization of negative permittivity [40] [37]. He proposed an artificial structure made of a three-dimensional cubic mesh. This mesh was made of thin metallic wires with a periodicity smaller than the wavelength as shown in Figure 1.4. This structure is able to reproduce the response of a diluted plasma.

Like this plasma, the proposed 3D cubic mesh has a negative permittivity for frequencies lower than the plasma frequency. The response is given by:

$$\epsilon \cong 1 - \frac{\omega_p^2}{\omega^2} \text{ and } \omega < \omega_p \tag{1.2}$$

where ω_p is the so-called plasma frequency.

Negative Permeability To reproduce a negative permeability, another three-dimensional mesh is necessary. This time it consists of an array of split-ring resonators (SRR). Again, the mesh's periodicity is smaller than the wavelength of the exciting electromagnetic field [38]. Each SRR is made of two concentric circles of metal, each of them being split. So the induced current cannot flow within one ring but rather in the other ring which is capacitively coupled. The periodic structure is illustrated in Figure 1.4 [10] [40]. This structure can be considered a resonant structure with its own resonance frequency. Because the SRR have a small size compared to the wavelength, the negative permeability μ is only obtained in a narrow bandwidth. This bandwidth is just below the resonance frequency. Finally, the permeability can be expressed as a function of the frequency [38]:

$$\mu(\omega) = 1 - \frac{F\omega^2}{\omega^2 - \omega_0^2 + j\nu\omega} \tag{1.3}$$

where ω_0 is the resonance frequency of the SRR's, ν is a loss term and F depends on geometrical parameters of the lattice.

Combination of both structures J.B. Pendry proposed two separate solutions to get a negative permittivity and a negative permeability. The first solution to visualize a metamaterial was proposed by D.R. Smith and his team by interlacing both structures seen above [45]. Interlacing an array of rods with an array of SRRs is shown in Figure 1.4. This structure accomplishes a negative index of refraction over a narrow bandwidth as it has been shown experimentally for different frequencies [45] [44].

1.4.3 Applications of metamaterials

To end this brief introduction to metamaterials, let us mention a variety of applications. Those include high-gain Antennas, frequency selective surfaces, and High Impedance Surfaces, Cloaking, Strongly Anisotropic Material as well as DNG materials for small antennas [40] [10].

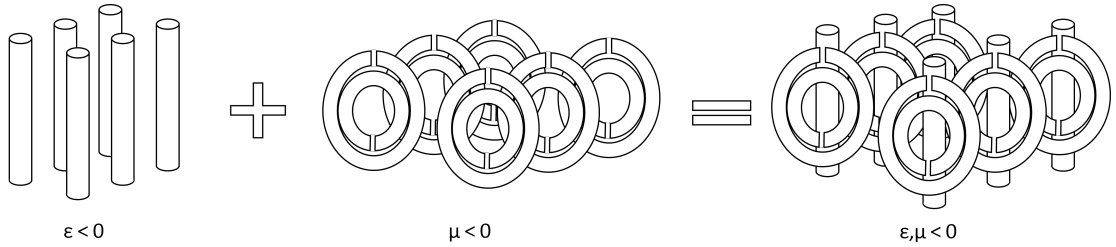


Figure 1.4: Structures of metamaterials [25]

1.5 MRI

The phenomenon of Nuclear Magnetic Resonance (NMR) was discovered in 1946 and was mainly used by chemists and physicists. It was however quickly adapted to be used in the medical world for various applications. The first use of NMR in medical imaging came thirty years later, resulting in the first (medical) image of a human. This medical use of NMR, which creates a signal, is referred to as Magnetic Resonance Imaging (MRI). Innovations such as this have proven to be essential and extremely useful in the medical field.
The following paragraphs are greatly inspired and are a summary of a course on Medical Imaging taught by Prof. Frank Peeters at UCLouvain [36].

1.5.1 Nuclear Magnetic Resonance

Nuclei's magnetic properties are the basis for Nuclear Magnetic Resonance (NMR). The properties of subatomic particles are determined by quantum physics. There are often simpler classical vector models that can be used to explain the principles of MRI since this process deals with a huge number of nuclei present in the macroscopic object being studied. There are, nonetheless, some quantum mechanical concepts to consider.

Magnetic properties of nuclei Protons and neutrons make up the nucleus of an atom. A nonzero spin quantum number I is a quantum-mechanical property of nuclei with uneven atomic mass or number and characterizes such nuclei. When I≠0, a particle is referred to as a "spin," which is defined by its magnetic moment $\boldsymbol{\mu_m}$. Magnetic moments are randomly oriented, however by applying an external magnetic field $\boldsymbol{B_0}=B_0\mathbf{1}_z$, they will be aligned in the same direction as the applied magnetic field. In the presence of the magnetic field, a spin can take only a discrete number of 2I+1 orientations. Spin 1/2 particles, for instance, can be oriented either up or down (parallel or antiparallel), and spin 3/2 particles can be oriented in four different ways as illustrated in Figure 1.5 in the center. Figure 1.5 on the right

shows the torque experienced by a magnetic moment $\boldsymbol{\mu_m}$ in a magnetic field $\boldsymbol{B_0}$, which precesses around $\boldsymbol{B_0}$ with a frequency $f_0 = \gamma B_0$ called the Larmor frequency (in Hz). The gyromagnetic ratio γ depends on the nucleus.

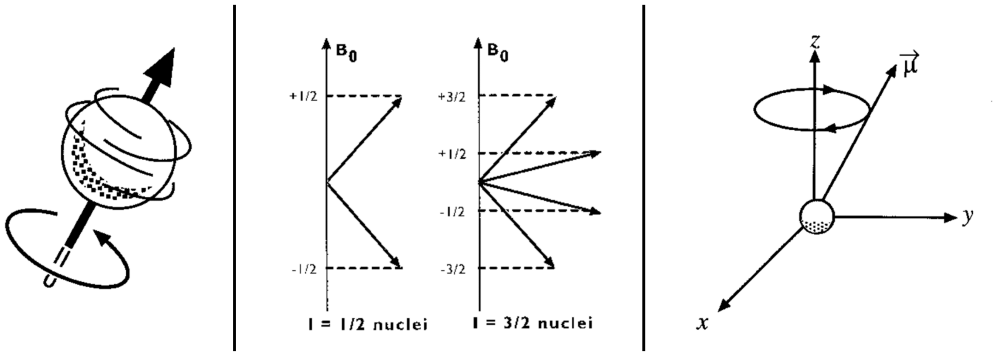


Figure 1.5: Characteristics of a spin [36]

Magnetization Instead of dealing with a single isolated spin, we deal with a collection of spins. The system consists of a vast collection of spins, each possessing a magnetic moment $\boldsymbol{\mu_m}$. To describe such a collection, we refer to its macroscopic magnetization:

$$\boldsymbol{M} = \frac{1}{V} \sum_i \boldsymbol{\mu}_{mi} \tag{1.4}$$

with V the volume of the ensemble. It is important to note that the vector sum [1.4] takes into account all spins inside V. As explained before, spins are usually randomly oriented unless an external field $\boldsymbol{B_0}$ is introduced. For a spin $I = 1/2$ there is a higher $E_\downarrow$ and lower $E_\uparrow$ energy level, corresponding respectively to spin down and spin up orientations. The following equation computes the energy for the whole collection of spins:

$$\Delta E \equiv E_\downarrow - E_\uparrow = h\gamma B_0 = h f_0 \tag{1.5}$$

with h Planck's constant. Hence, there is a proportionality between the energy difference and the Larmor frequency f_0. Furthermore, the occupation of both orientations and their ratio can be calculated using the Boltzmann distribution:

$$\frac{N_\uparrow}{N_\downarrow} = \exp\left(\frac{\Delta E}{kT}\right) \tag{1.6}$$

with T the absolute temperature and k Boltzmann's constant. There are therefore more spins that point upward (lower energy) instead of downward. Therefore, the magnetization presented in equation 1.4 is defined by a nonzero equilibrium value $\boldsymbol{M_0}$=$M_0\mathbf{1}_{\boldsymbol{z}}$. There are actually only small population differences at the field strengths of interest: only a few parts per million. This leads to NMR being classified as a low-sensitive technique.

Magnetic resonance A thermally equilibrated spin system has a magnetization $\boldsymbol{M_0}$ that points along the external field $\boldsymbol{B_0}$. Each spin is precessing around $\boldsymbol{B_0}$ at the Larmor frequency f_0, but their phases are randomly distributed. This $\boldsymbol{B_0}$ field however, is not the one needed to detect MR signals. Indeed, an oscillating RF-pulse will create a linearly polarized magnetic field $\boldsymbol{B_1}$ with a fixed orientation. During the excitation, $\boldsymbol{B_1}$ is referred to as B_1^+. This RF-pulse, characterized by its frequency f_{RF} and phase φ, will modify the resonance condition that becomes $f_{RF} = f_0$.

$$\boldsymbol{B_1}(t) = 2B_1(t)\cos(2\pi f_{RF}t + \varphi)\mathbf{1}_{xy} \tag{1.7}$$

The newly created $\boldsymbol{B_1}$ field is oriented in a perpendicular plane to $\boldsymbol{B_0}$. We find a definition of the angle of the magnetization using the new rotating frame [36] and taking into account the finite duration of the RF-pulse with time-varying amplitude $B_1(t)$:

$$\alpha = \gamma \int_{T_{RF}} B_1(t)dt \tag{1.8}$$

Such RF-pulses are called α-pulses, with 90°- and 180°-pulses common examples. Those different pulses are obtained by varying amplitude and duration. RF-pulses will transmit energy to the spins, inducing a change in energy level (from lower to higher). After this energy transmission, or excitation, the magnetization $\boldsymbol{M}$ will be tilted away from $\boldsymbol{B_0}$. In this new position it can be described as follows:

$$\boldsymbol{M} = M_z\mathbf{1}_{\boldsymbol{z}} + M_{xy}\mathbf{1}_{\boldsymbol{xy}} \tag{1.9}$$

with its decomposition into a longitudinal M_z and transverse M_{xy} magnetization.

Relaxation Spin systems try to return to their equilibrium state after being excited (i.e. $\boldsymbol{M_0}$). M_z will therefore return to M_0 and M_{xy} will vanish as shown in Figure 1.6. During this process, the spins generate an echo at f_0. This echo, i.e., a RF field, is referred to as B_1^-. This involves two separate processes. They are referred to as relaxations; T_1, also referred to as spin-lattice or longitudinal relaxation, and T_2, also referred to as spin-spin or transverse relaxation. A more

detailed definition of these processes is given by Peeters [36]. T_1 describes how much time M_z needs to return to its equilibrium state $\boldsymbol{M_0}$. According to a quantum mechanical interpretation, field fluctuations are responsible for the relaxation of T_1. Like for T_1, T_2 relaxation is caused by field fluctuations but also static inhomogeneities. The combination of them results in the disappearance of M_{xy}. Furthermore, the spins tend to dephase from each other when the external static field $\boldsymbol{B_0}$ exhibits spatial non-uniformities, which is taken into account by introducing a relaxation period T_2^*. The equations of motion of the magnetization $\boldsymbol{M}$ in the rotating frame are described by the Bloch equations [4] [24].

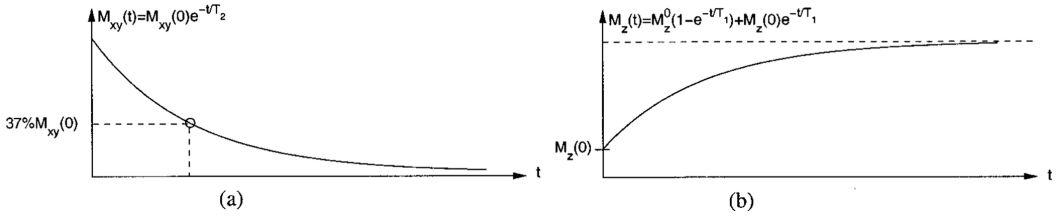


Figure 1.6: Relaxation curves [36]

MR-signal Let us take a spin system in thermal equilibrium. When applying a resonant 90°-pulse, the transverse magnetization with an oscillating behavior will appear as explained before. As a result, a signal known as the Free Induction Decay (FID) will be induced and B_1^- at frequency f_0 will be produced in a pick-up coil. This is based on Faraday's law and expects the pick-up coil to have its axis in the transverse plane. This MR-signal is sampled by an analog-to-digital converter (ADC). The use of heterodyning and quadrature detection by the RF-receivers means that both phase and magnitude of the transverse magnetization are measured.

1.5.2 Magnetic Resonance Imaging

Previous paragraphs described the NMR phenomena and the creation of MR-signals using RF-pulses. The definition of those MR-signals however, corresponds to the excitation of the whole sensitivity volume of the receiver coil. In MRI the goal is to get an image of a specific part of the human body. Magnetic field gradients will be used to accomplish this by localizing MR-signals in space.

Gradients Magnetic field gradients are linearly dependent and are defined as $G_x = \partial B_z/\partial x$ for a variation along the x-axis. The same applies to defining gradients G_y and G_z. Applying them to the static field $\boldsymbol{B_0}$ induces two main changes. First

of all, a new, total, field is created taking into account the magnetic field gradient $\boldsymbol{G} = (G_x, G_y, G_z)$:

$$\boldsymbol{B} = \boldsymbol{B_0} + (G_x x + G_y y + G_z z)\mathbf{1_z} = \boldsymbol{B_0} + (\boldsymbol{G}\cdot\boldsymbol{r})\mathbf{1_z} \tag{1.10}$$

with $\boldsymbol{r} = (x, y, z)$ the position. Secondly, not only the field becomes position dependent but also the Larmor frequency:

$$f_0(\boldsymbol{r}) = \gamma B(\boldsymbol{r}) = \gamma[B_0 + \boldsymbol{G}\cdot\boldsymbol{r}] \tag{1.11}$$

Slice selection Using the above-described gradients, it is possible to excite spins in a specific slice of the whole volume. To define the thickness of this slice, for example Δz in the z-direction using a gradient G_z, the RF-pulse has to be of bandwidth $\Delta f = \gamma G_z \Delta z$. Indeed, because of G_z, the new Larmor frequency is:

$$f(z) = \gamma[B_0 + G_z z] \tag{1.12}$$

Exciting a slice around position z_0 requires shifting the carrier frequency from the Larmor frequency to $f_c = f_0 + \gamma G_z z_0$. It becomes clear that varying the gradient but using the same RF-pulse will result in varying thicknesses. By taking the Fourier transform, the waveform of the RF-pulse is obtained, which corresponds to the sinc-function. However, sinc-pulses do not have an infinite duration. This results in a phase shift, linear with position, leading to signal loss. As seen during the Medical Imaging classes [36], using a refocusing z-gradient will compensate this phase-shift. Truncation and the use of window functions to try to minimize the side lobes are also mentioned [36]. Last but not least, the use of the Fourier transform description is valid for small flip angles ($\alpha > 30°$) but not bigger ones. Using the Bloch equations would be more accurate. It does, however, provide at least a qualitative description.

Phase and frequency encoding in Fourier domain For the spins to be localized, spatial information has to be encoded into the MR signals after the slice has been excited. There are two directions along which spatial information must be encoded. This is done through two different methods, phase and frequency encoding.

In order to encode spatial information, it needs to be encoded along the y-axis first. Let us apply for a short time T_y after the excitation, a gradient G_y in the y-direction. This will induce a phase shift and the transverse magnetization becomes:

$$\varphi(y) = -\gamma G_y y T_y \tag{1.13}$$

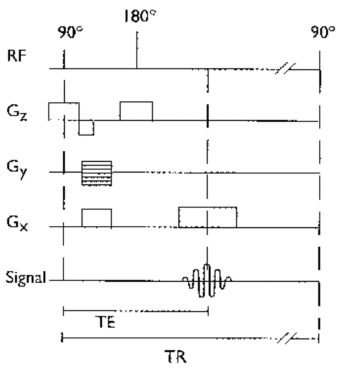


Figure 1.7: Frequency and phase encoding using gradients [36]

with G_y the phase encoding gradient. Hence the signal is phase encoded with its linear phase in the y-direction. The second step is spatial encoding along the x-direction. After using G_z for slice selection and G_y for phase encoding, G_x is now used for frequency encoding. This will make the Larmor frequency dependent on x:

$$f(x) = f_0 + \gamma G_x x \tag{1.14}$$

with G_x the frequency encoding or read out gradient. Hence the signal is frequency encoded with its linear frequency in the x-direction.
In Figure 1.7 G_z is used to create a spin-echo sequence and for slice selection. After excitation different G_y create different phases. For each different G_y frequency encoding takes place using G_x. This way the signal is both frequency- and phase-encoded in the Fourier domain.

1.5.3 Ultra-high field MRI

The last part of this chapter concerning MRI is an overview of recent and future technologies in this field. The strength of magnetic fields has evolved greatly since the advent of MRI in the medical world. They have gone from less than 0.5T in the beginning to 3T in the current medical world [47]. The next generations of scanners are going up to 11.7T, but it is the 7T field levels that are the most promising for the moment[47]. Scanners are classified according to their fields. There are currently 3 groups; moderate fields (1.5T), high fields (3T) and ultra-high fields (UHF),the latter being mentioned before (7T-11.7T). Table 1.1 summarizes those three groups.

Moderate fields	1.5 [T]	63.86 [MHz]
High fields	3 [T]	127.74 [MHz]
UHF	7-11.7 [T]	298-498 [MHz]

Table 1.1: Classification by fields

UHF has one main advantage; improved SNR [39] [20]. This allows obtaining better quality images. Note, as mentioned by [34], that factors other than the B_0 field strength also come into play in the SNR improvement.
Unfortunately UHF also has an important defect; the homogeneity of the B_1 field. This is mainly due to the inverse proportionality between field strength and wavelength. The decrease in wavelength is a problem, as it is becoming comparable to the size of the human head (12 [cm] at 7T) [48]. Indeed, short wavelengths are influenced by constructive and destructive interferences in human tissues. As a result, their transmit profiles become complex and nonuniform [13].

1.5.4 Principle of Functional imaging

The main use of Functional MR imaging (fMRI) is the analysis of local blood supply in the brain. This blood supply is activated by specific stimuli and is using the BOLD (Blood Oxygen Level Dependent) contrast. This contrast exploits the changes in the oxygen content of the blood. This change in oxygen content is influenced by iron in the blood. Two states of hemoglobin (red blood cells) exist in which much of the iron is: oxyhemoglobin (diamagnetic) and deoxyhemoglobin (paramagnetic). While brain tissue in an activated state only has a 5% increase of oxygen consumption, the blood flow in activated regions increases by 20-40%. As a result, the decreased susceptibility of oxygenated blood results in a longer $T2^*$ for activated brain tissue than non-activated brain tissue. This longer $T2^*$ means an increase of signal intensity in activated brain areas can be shown using heavily $T2^*$-weighted sequences. The last step is to subtract non-activated from activated images to show the area of activation. It is important to mention that this is not a direct measure of brain activity, but a measurement of the changes of blood flow [36].

1.6 Basic Birdcage design

As described above, RF coils are needed to excite the nuclei. The choice of these RF coils and their design is essential if a quality image is expected. Besides using the RF coils only in the transmission mode, they also have been used only in the reception mode. We speak of a transceiver coil if a single coil performs both steps. If, on the contrary, two separate coils are used for each step, we speak of transmit only and receive only coils, however using one RF coil in the transceiver mode is also possible [2] [34]. A classification of different RF coils can be found in a work by Nikulin [34] and is summarized below. Generally, the plurality of RF coils can be classified into two groups depending on the application: surface coils and volume coils. In the case of Birdcages, volume coils are generally used as transceiver coils. However, surface coils have been used as receiver coils, especially at UHF MRI.

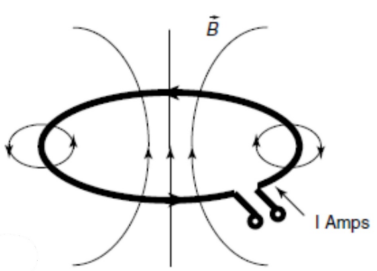
1.6.1 Surface coils

Surface coils, loop coils more precisely, are the basic coils used in MRI imaging. An example of the loop coil is shown in Figure 1.8a. Instead of focusing on having a high SNR from the whole sample, in many types of observations, it is more important to acquire as much signal as possible from a small region of interest (ROI) [17]. It was first used in 1970 to measure blood velocity [32]. Nowadays, loop coils can be used both as transmit and receive coils as well as receive only and are widely available commercially for any field strength [26] [33]. For example,

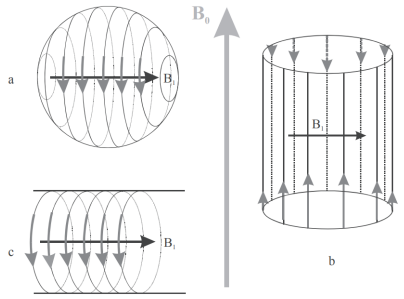
preclinical imaging of small animals' organs; clinical imaging at 1.5T and 3T of wrist, joints of toes and fingers, skin, temporomandibular joints imaging, and knees [34].

1.6.2 Volume coils

For the case of brain and body imaging, volume coils are well suited as they give the best homogeneity of spin flip angles within the imaging sample [51]. More precisely, cylindrical volume coils producing a transverse field. Another kind of cylindrical volume coils or resonators can also produce an axial field, but this is not useful for brain imaging. Indeed, the transverse field is perpendicular to the axis of the cylinder as wished [31]. Both resonator types are presented in Figure 1.8b, with axial resonators left and a transverse resonator on the right.



(a) Surface loop coil [34]



(b) Surface currents of axial and transverse resonators [31]

Figure 1.8: RF coils

In order to create a homogeneous magnetic field B_1 inside the cylinder, surface currents $J(\varphi)$ are used flowing parallel to the cylinder axis. A homogeneous field B_1 will be created when the phase of the current equals the azimuthal angle φ. As mentioned by Mispelter et. al. [30] in the case of brain imaging this can be exploited for scanners up to 4T.

Birdcage coils C. Hayes invented the Birdcage, a transverse volume coil allowing the generation of a homogeneous magnetic field in the cylinder, in 1985 [19]. It can be used for the whole body [19], however different cases with different powers have been presented over the years [5] [27] [23]. The historical development of the Birdcage in 2009 by Hayes [18] and the recent progress in this field described in 2020 by Ahmad et. al. [1] perfectly contextualize the world of the Birdcagecoils. Logically, the increase in homogeneity goes hand in hand with an increase in

complexity. A Birdcage has a number k of resonant modes with k depending on the number of legs N_l. The homogeneous field is obtained for mode $k = 1$. Increasing N_l will increase the homogeneity but will reduce the amplitude of the field at the center of the cylinder [46]. As mentioned by Mispelter, there is a limit for the number of legs compromising homogeneity and manufacturing difficulties. With 32 legs possible for large resonators at low frequency, the limit sits at 12-16 legs [30]. In the case of a well equipped electronic lab however, a 64 to 128 leg Birdcage is ideally the best compromise that is still accessible [31].

1.6.3 Performance assessment

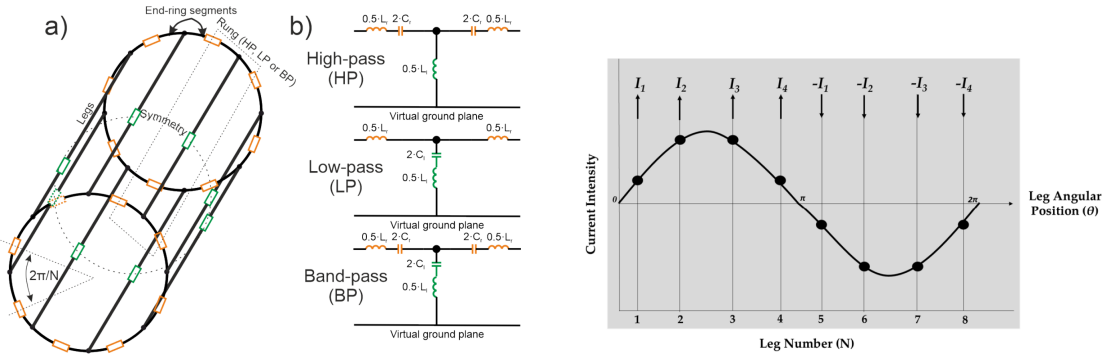
The main parameters are used in this thesis to asses performances of the Birdcage. They are used and mentioned throughout the thesis, it is therefore appropriate to introduce them.

- The homogeneity of the B_1^+ field is obtained using the normalized standard deviation.
- The specific absorption rate (SAR) is the amount of energy absorbed by the patient, in this thesis represented by a phantom. A phantom responds the same way human tissues and organs would act and is defined by its conductivity (σ) and relative permittivity (ϵ_r). Different values are used to approach different organs or tissues. During an MRI examination, the SAR is constantly controlled to avoid excessive heating of the patient limited to 4 [W/kg] in European countries.
- The SAR efficiency defined as $(B^+/(SAR)^{1/2})$

1.6.4 Birdcage principle and design

As mentioned earlier, a Birdcage consists of N_l equally distributed legs. In general N_l is between 4 and 32. For a radius r a leg is positioned every $\varphi = 2\pi/N_l$. These N_l legs are connected, at the top and at the bottom, by two end-rings as shown in Figure 1.9a. Besides the legs and end-rings, there are also different components. Inductances are located on each leg and between each leg on the end-rings. The second type of components are the capacitors. There are 3 possibilities for the placement of the capacitors which correspond to a low-pass, high-pass or band-pass filter. The capacitors are placed, respectively, on the legs, on the end-rings or on both. These 3 different topologies are represented, in the form of unit-cell, in Figure 1.9a and each has different properties and specificities. As mentioned by [14], coils used for UHF MRI are high-pass, but lower field MRI requires low-pass

coils because the fundamental (k=1) mode of the LP coil is lower in frequency in comparison to the HP Birdcage coil of similar size.



(a) Conventional Birdcage coil [34] (b) Sinusoidal current profile [22]

Figure 1.9: Birdcage principle and design

In addition to these different properties, the components define the ladder network whose resonance drives the currents. The resonant modes of this ladder network correspond to stationary states created when waves combine constructively. Ideally, for the fundamental mode the current going through the legs has a sinusoidal intensity profile realized by adjusting the inductance (L) and capacitance (C) parameters. When such a current, as shown in Figure 1.9b, is reached, the magnetic field distribution theoretically reaches the optimal homogeneity. At lower frequencies this field can be defined by the Biot-Savart law [49] [21]. Finally, it is possible to define the value of the components that reach the Larmor frequency by analyzing the unit-cells.

1.6.5 Electrical representation of a Birdcage

As described in the previous section, we can analyze a Birdcage by focusing on a unit cell. Indeed, a Birdcage is a closed electrical system with the last leg connected to the first one; it corresponds therefore to several LC circuits put together. A LC circuit, or unit cell, is represented with the capacitors C_r and C_l and its self-inductances L_r and L_l respectively for the ring and leg. The values of the capacitors are chosen to respect a resonance condition [22]. The expression of the self-inductances can be deduced from references [16] [7] [35].

$$L^s = 2l \cdot ln\left(\frac{2 \cdot l}{w + t}\right) \tag{1.15}$$

where l is its length, w is its width, t is its thickness. In addition to the self-inductances, two unit cells will induce a mutual inductance M_{ij}. This is expressed as follows:

$$M_{ij} = 2l \cdot ln\left(\frac{l}{d} + \sqrt{1 + \frac{l^2}{d^2}} + \sqrt{1 + \frac{d^2}{l^2}} + \frac{d}{l}\right) \tag{1.16}$$

Where l is the length of the parallel wires and d the distance between them. Lupu et. al. described the mutual inductance between end-rings but this is more complex [27]. In the case of vertically symmetrical Birdcages with the current flowing in the opposite direction in the end-rings, a simplification is possible. The horizontal plane in the middle of the Birdcage becomes the ground and the values of the components are adapted as in Figure 1.10 on the right.

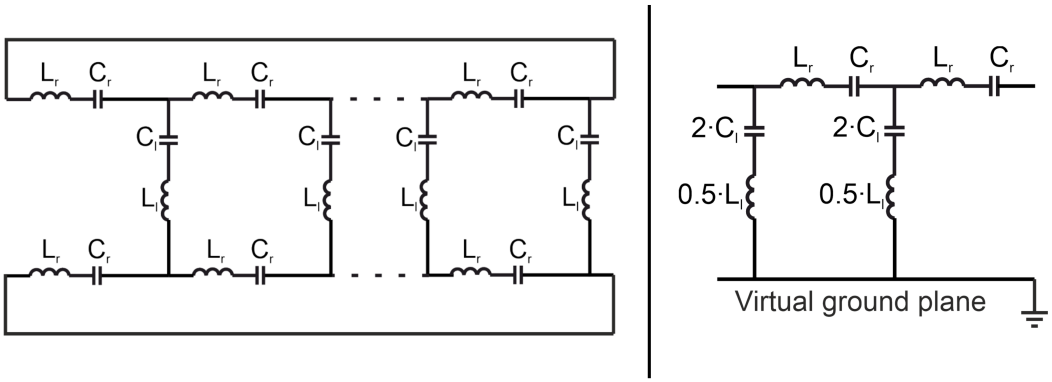


Figure 1.10: Simplified electrical representation of a Birdcage coil's unit cell [34]

Two interesting approaches to define the values of the capacitors are given in appendix A and B. The first one uses a simplified electrical representation of a Birdcage while the second one uses a transmission line-based approach.

1.6.6 Impact of dimensions

To finish this section about the Birdcage, let us discuss the impact of the length and radius of a Birdcage. After discussion and some simulations, it appeared that a general statement could be as follows: increasing the radius will increase the homogeneity but will decrease the maximum field, while increasing the length will impact, positively, the vertical homogeneity.
A more precise and theoretically funded discussion however can be given going back to the Biot-Savart law. As described in [31] [11] B_{mean} is given by:

$$B_{mean} = \frac{2\mu_0 I\zeta}{\pi d} \frac{l}{\sqrt{l^2 + d^2}} \left(1 + \frac{d^2}{l^2 + d^2}\right) \tag{1.17}$$

with l the length, d the diameter and I the current in the Birdcage. ζ is related to N_l. Using equation 1.17, [51] deducts following relation between l, d and the SNR:

$$SNR \propto \frac{1}{d} \frac{l}{\sqrt{l^2 + d^2}} \left(1 + \frac{d^2}{l^2 + d^2}\right) \tag{1.18}$$

It can be deduced that there is an inverse proportionality between the SNR and d and that the maximum SNR occurs at $\frac{d}{l} = \frac{1}{\sqrt{2}}$.

1.7 Structure of the thesis

In order to achieve the objectives mentioned in previous section, the thesis is divided into 4 chapters:

- **Chapter 2 : Methodology**

  Chapter 2 is dedicated to the methodology, more precisely the global approach and the numerical methods and tools used to implement it. First, the use of GMSH [15] to design the Birdcage and retrieve its mesh will be introduced. In order to define the ROI and the desired field, Gaussian distributed weight matrices will be used. Therefore, different versions of Gaussians as well as their specific definition will be presented. A Method of Moments (MoM) based numerical simulation code will be adapted to incorporate the weight matrix. A global understanding and the main steps of this code will be described. Its main goal is to simulate and optimize the values of the components presented in section 1.6.5. The objective function of the optimization step is the standard deviation. The last part of Chapter 2 will be the modification of this objective function to ensure that the weight matrix is taken into account.

- **Chapter 3 : Weight matrix used on the conventional Birdcage**

  In Chapter 3, the focus will be on the comparison of several cases and an explanation of the different results. In a first step, the conventional Birdcage will be used in a symmetric mode, and to confirm the feasibility of the approach. A variety of weight matrices and objective functions will be carried out exploring the (dis)advantages and limits of the symmetrical design. In a second step, the asymmetric mode of the conventional Birdcage will be used. Again, a variation of objective functions and weight matrices will allow us to explore the possibilities offered by the Birdcage. This asymmetric case is more interesting from a medical point of view.

- **Chapter 4 : Functional imaging**

  Chapter 4 tackles a more complex and concrete medical application of the approach; Functional imaging. The interest not in the homogeneity but more in the shape of the fields will lead to the introduction of a new metric in this chapter.

- **Chapter 5 : Weight matrix used on the Connected Birdcage**

  The last chapter looks into tailoring of the approach and the process to the use of a connected Birdcage [9]. More complex configurations of the Birdcage provide different results. Identical weight matrices and objective functions will be used. A comparison with the case in Chapter 3 will be provided.

Chapter 2

Methodology

2.1 Global approach

The goal of this Master Thesis is to adapt a conventional Birdcage in order to reach a better homogeneity in the region of interest (ROI). Several regions and adaptations are studied. However, the same methodology is used in each case. This second chapter presents this methodology through different sections. First, the morphology of the Birdcage is designed and adapted using the open-source GMSH meshing software. Once the 3D-version of the Birdcage is created, a weight matrix is defined to highlight the ROI. After that, the mesh and the weight matrix are used in the MoM code to compute the value of the electronic components to optimize the weighted homogeneity in the ROI. Those component values will then be used to simulate the obtained fields. Finally, in order to compare the different results and analyze the effect of each specific case, a standard metric is used to compare those results. The metric used is a normalized standard deviation (SD) and will be presented in the last section of this chapter.

2.2 Design in GMSH

GMSH [15] is a three-dimensional finite-element mesh generator with built-in pre- and post-processing facilities. It provides a fast and light mesh of the Birdcage. GMSH is used to design the complete structure of the Birdcage, but not the values of its components. Different morphologies of Birdcages are obtained by changing the height and the radius. Besides this, additional legs and structure elements can be added. Although the values of the components are not defined, GMSH requires the position of all components to be present in the design. The position will also be specified in the MoM code but has to match the mesh designed in GMSH. However, the type (capacitance or inductance) of those components is only

defined in the MoM code. An example of the Birdcage design in GMSH can be found in Figure 2.1. Let us note that only $1/N_l$ of the Birdcage is designed. This comes as a result of the symmetry of this problem and improves the computation time and complexity as described later in this chapter.

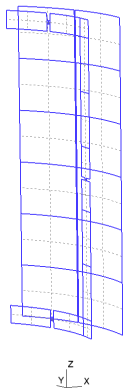
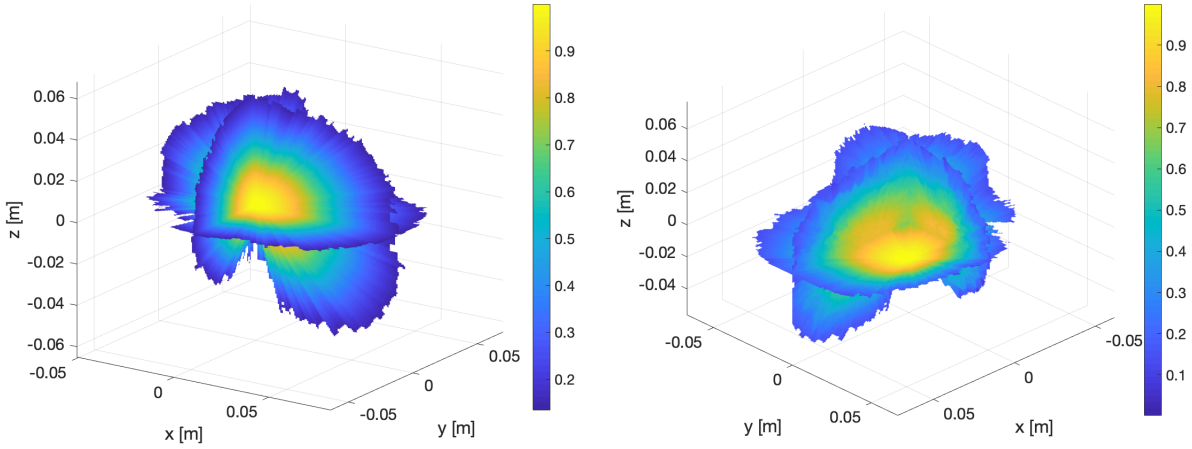


Figure 2.1: Design in GMSH

2.3 Weight matrix

As described above, the main objective of this thesis is to improve the homogeneity of the SAR efficiency in the ROI. The weight matrix is used in two ways in this thesis. First, it is used to define the ROI in which the homogeneity value has the highest importance when trying to optimize the Birdcage. The second one is to define the desired field shape. Note that when the weight matrix is used later on, it will always be normalized.

In MRI simulations, and throughout this thesis, the brain is represented by a phantom of similar dimensions. As mentioned in the previous chapter, a phantom responds the same way human tissues and organs would act and is defined by its conductivity (σ) and relative permittivity (ϵ_r). Figure 2.2 shows two examples of weight matrices computed in an asymmetric phantom representing the brain. The weights clearly define regions of interest. These areas are indicated by higher weight values (in yellow). We can see that the closer the ROI, the closer the weights are to 1. Moreover, the weights are never zero to limit the appearance of fluctuations outside the ROI and to ensure an acceptable global homogeneity. The weight matrix defines the ROI using a Gaussian distribution as it will be explained in the following section. The definition of those weight matrices is adapted for the



(a) Centered ROI (b) Non-centered ROI

Figure 2.2: Weight matrices

representation of many organs. Indeed, the code [1] is defined for any star-convex 3D volume.

2.3.1 Gaussian

As mentioned before, the weight matrices are defined using an adapted version of the Gaussian function. A Gaussian function is described as follows:

$$f(x) = a \exp\left(-\frac{(x-b)^2}{2c^2}\right) \tag{2.1}$$

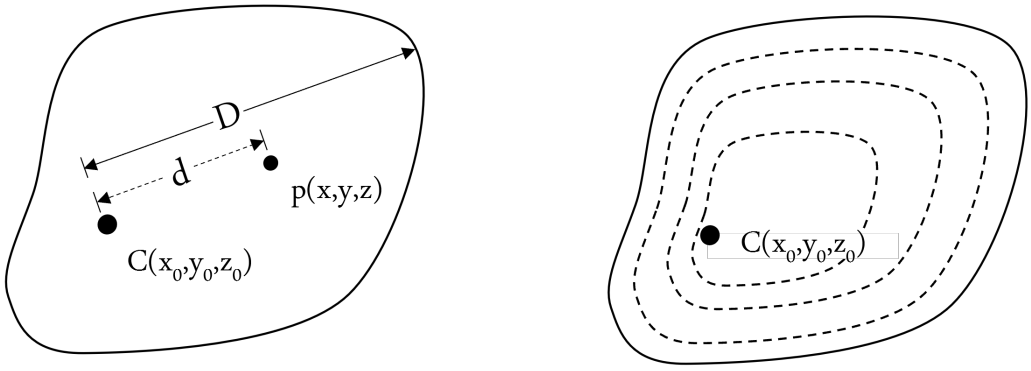
With real constants a, b and non-zero c. Gaussians are widely used in the world of statistics, with the Gaussian distribution as its best-known example.

The interesting aspect of a Gaussian is its maximum at the center and its attenuation (characterized by c). This behavior is used in the weight matrix to have weights that decrease when moving away from the center. The center here will indicate the center of the ROI, which contrary to the classical case is therefore off-centered. Starting from equation (2.1), the definition of the weights used in the weight matrix is given as follows:

$$W(x, y, z) = e^{-\frac{1}{2a}(\frac{d}{D})^2} \tag{2.2}$$

[1] MATLAB code, written by the authors of this thesis: Thomas Clerbois and Antoine Rampelbergh

Where a is called the attenuation factor, d is the distance between the point $p(x, y, z)$ and the center $C(x_0, y_0, z_0)$ of the ROI, and D is the distance between C and the edge of the organ in the direction of p. An explanatory image can be found in Figure 2.3a. Due to the definition given by equation 2.2, the Gaussian "fits" the shape of the organ in addition to being off-centered. Indeed, each direction has its specific value D. Therefore, 2 points in the same direction but at a different distance d will have a different weight. The second case of interest is two points with the same distance d but in a different direction. These points have a different value D, hence a different weight although they are equidistant from the center C of the ROI. Figure 2.3b represents the weights as a level set, to get a more intuitive understanding.



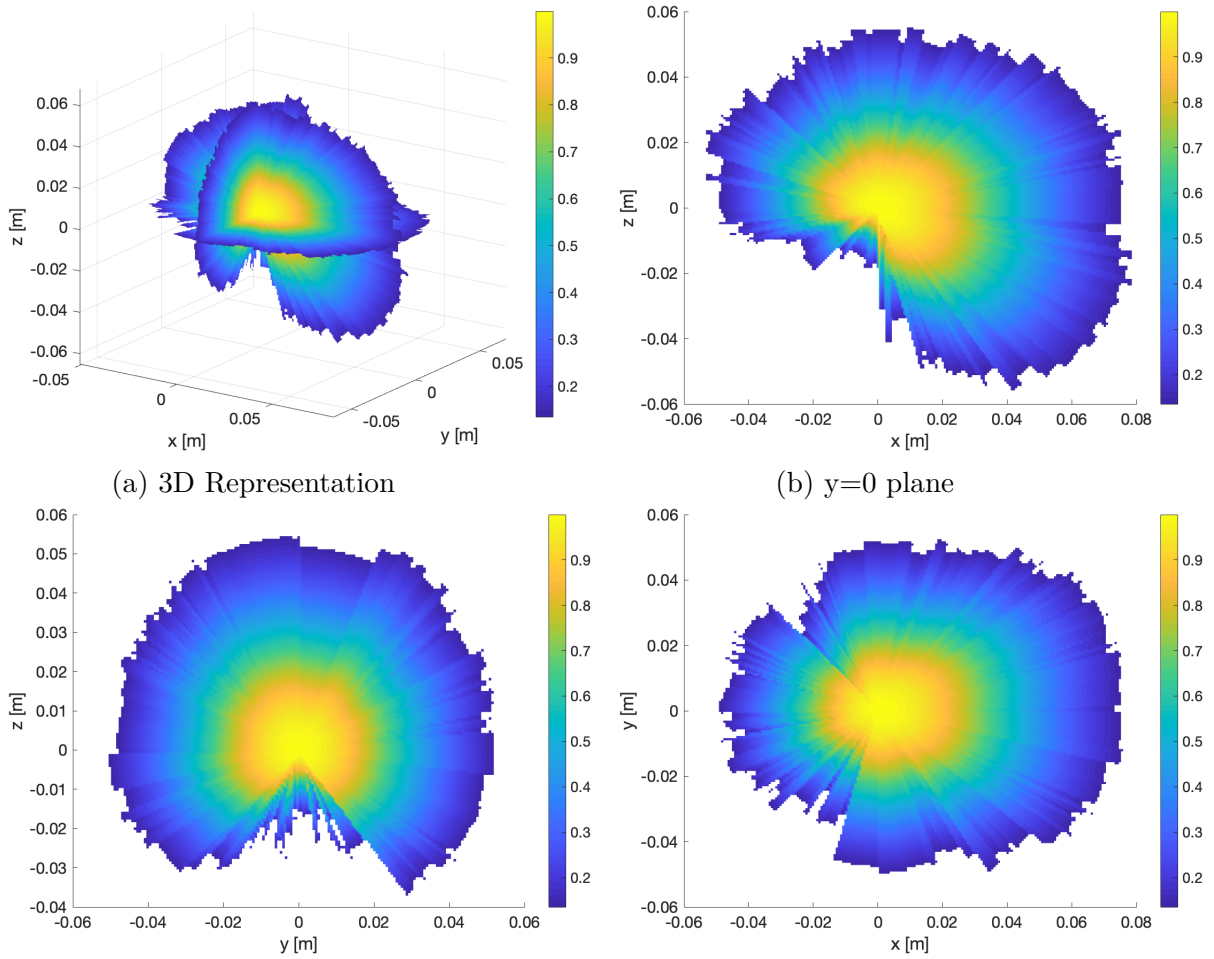
(a) Schematic representation of d and D (b) Level set of weights

Figure 2.3: Schematic representation of weights

The Gaussian weights:

- equal 1 in the center of the ROI, thus highlighting the homogeneity in this region.
- decrease with the distance d, giving more importance to points closer to the center of the ROI.
- are non-zero on the whole phantom volume and decrease with a slope inversely proportional to the distance D, ensuring acceptable global homogeneity, a smooth decrease, and a fit of the organ.

An example, already mentioned before, of a weighted matrix centered in (0,0,0) in a brain can be found in Figure 2.4.



(a) 3D Representation

(b) y=0 plane

(c) x=0 plane

(d) z=0 plane

Figure 2.4: Weight matrix example in brain

The evolution of the weights in 3 distinct directions from the center C is represented in Figures 2.5 and 2.6.

Last but not least, this definition of the weights is valid for "simple" cases with only one center (and therefore maximum). More complex shapes, like a torus or ellipse, have adapted definitions. However, the attenuation defined by a Gaussian is always present. When used in this thesis, an additional explanation will be present. This is valid for weight matrices defining both an ROI or a desired field.

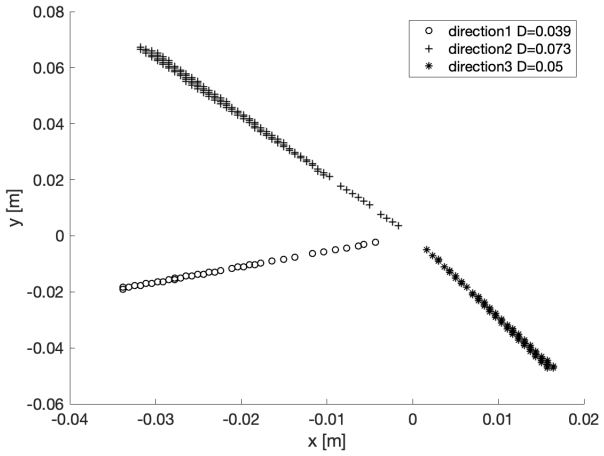


Figure 2.5: Spatial representation in plane z=0

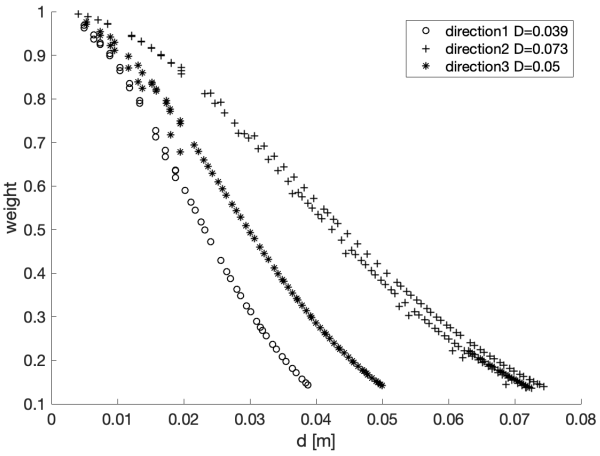


Figure 2.6: Weights in three directions

Influence of attenuation factor a The influence of parameters d and D have been discussed above. This last paragraph will come back to the impact of the attenuation factor a. As the name suggests, a describes the attenuation of the value of the weights with d. A higher a means a higher or faster attenuation and thus a faster decrease in the weights values. The influence of a is represented, for a fixed D, in Fig 2.7. Those are theoretical values, and do not represent any case of this thesis.

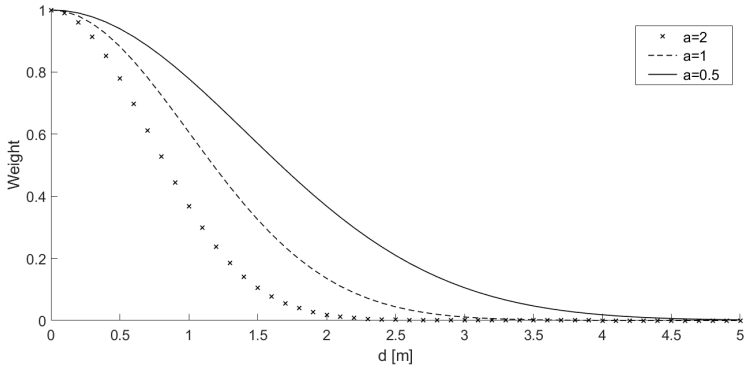


Figure 2.7: Impact of a for fixed D

2.3.2 Octree

Computing the weight matrices takes time and heavy calculations. To compute the Gaussian, D (the distance between the center of the ROI and the edge of

the phantom in the direction of p) has to be computed for every point inside the phantom. Octrees are used to accelerate the computation of the weight matrices. This space optimization divides a sample into subgroups called branches. In this case, the points of the edge of the organ are divided into 64 groups with respect to their spherical coordinates. The subdivision is shown in Figure 2.8, the branches can be distinguished by the colors.

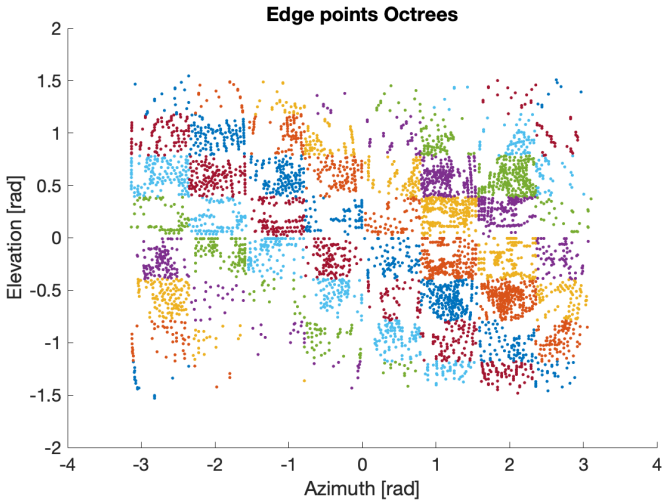


Figure 2.8: Spherical octree for k=8

As a result, the calculations can be done on a single branch of interest instead of on the entire sample. Since the edge of the phantom is a sample of points $p(x_e, y_e, z_e)$, every point inside the phantom has to be linked to the edge point that is the closest to its direction. Using the spherical coordinates, this is equivalent to computing:

$$\min_{x_e,y_e,z_e} \sqrt{\Big(Az(x_e,y_e,z_e) - Az(x,y,z)\Big)^2 + \Big(El(x_e,y_e,z_e) - El(x,y,z)\Big)^2} \qquad (2.3)$$

for every $p(x, y, z)$ inside the phantom. This algorithm is so to have $\mathcal{O}(N_e N)$, where N_e and N are respectively the number of edge points and the number of points inside the mesh. The complexity is therefore proportional to the density of the mesh and the precision of the edge of the phantom. Having a precise weight matrix is thus very time-consuming.
By dividing the spherical domain into k^2 subgroups, and attributing a branch to each point of the domain, the complexity can be reduced to $\mathcal{O}(\frac{N_e N}{k^4})$.
There must stand at least one edge point in each branch for the algorithm to work. The number of branches is therefore limited.

2.4 MoM code

As explained in the general section, the MoM code computes the values of the electronic components of the Birdcage that optimize the homogeneity in the ROI. The code has two main steps. First, the electric and the magnetic field are computed for an initial set of values for the electronic components. The equivalent surface currents are computed through the Method of Moments, and the fields are predicted in the phantom thanks to the field equivalent principle. Then, the values are optimized with respect to the local homogeneity using the open circuit pattern to save computing time.

2.4.1 Method of Moments

This explanation of the Method of Moments is an abstract of the thesis of Radu [40]. Therefore, the equations, the Figures and a deeper explanation can be found in his work. The papers by Dardenne [10] and Sabet [41] were used to complete the explanation. This step is already implemented in the code provided. It has therefore not been redeveloped. The Method of Moments (MoM) can be used to predict the fields behaviors in open boundary electromagnetic problems. It is based on the integral form of Maxwell's equations which is faster and less demanding in terms of computing resources [41]. The goal of the method is to compute the surface currents that will be used by the equivalent surface currents and equivalent fields theorems. Those theorems are explained in the next section.

First, the surface current is sampled into a set of expansion functions. Each expansion function, called basis function ($\bar{f}_n$), is associated with a specific vertex and is defined as :

$$\bar{\mathbf{f}}_{\mathbf{n}}(\bar{\mathbf{r}}) \begin{cases} \frac{\bar{\rho}_n^+}{h_n^+} & \text{if } \bar{r} \text{ is in } S_n^+, \\ \frac{\bar{\rho}_n^-}{h_n^-} & \text{if } \bar{r} \text{ is in } S_n^-, \\ 0 & \text{elsewhere .} \end{cases}$$

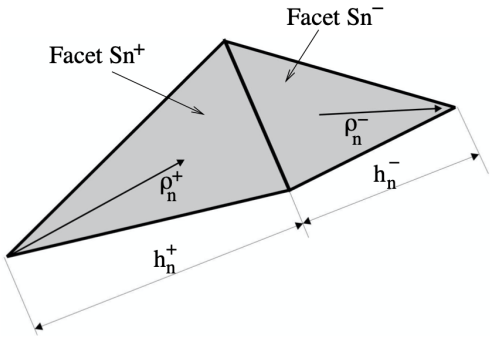


Figure 2.9: Geometry of the RWG basis function [40]

Then, the surface current $\bar{J}$ is approximated as the weighted vectorial sum of these elementary currents :

$$\bar{J} = \sum_{n=1}^{N} I_n \bar{f}_n \tag{2.4}$$

Where N is the total number of internal vertices in the mesh of the surface, $\bar{f}_n$ is the basis function associated to the vertex n, and I_n is a weighting coefficient.

In order to find the weighting coefficient I_n, the current generated by an incident electromagnetic wave $\bar{E}^{inc}$ is calculated with the electric-field integral equation (EFIE). EFIE enforces the total electric field on the surface to be null. The surface current, $\bar{J}$, induced by $\bar{E}^{inc}$, creates a scattered field $\bar{E}^{sc}$. Therefore, the EFIE becomes :

$$\bar{E}^{sc}_{tan} = \bar{E}^{inc}_{tan} \tag{2.5}$$

The expression of $\bar{E}^{sc}$ is demonstrated by Dardenne [10] and rewritten by Radu [40] as :

$$\bar{E}^{sc} = -j\omega\bar{A} + \frac{1}{j\omega\epsilon\mu}\nabla(\nabla \cdot \bar{A}) \tag{2.6}$$

where ϵ and μ are respectively the permittivity and the permeability of the medium and ω is the angular frequency. $\bar{A}$ is a mathematical tool called vector potential. Its definition is so that its rotation equals the magnetic field. In this situation, it can be rewritten as:

$$\bar{A}(\bar{r}) = \frac{\mu}{4\pi}\int_S \bar{J}(\bar{r}')\frac{e^{-jk|\bar{r}-\bar{r}'|}}{|\ \bar{r}-\bar{r}'\ |}\,dS \tag{2.7}$$

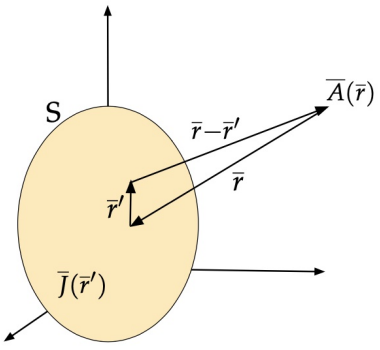


Figure 2.10: Vector potential $\bar{A}$ created by a surface current $\bar{J}$ on a metallic surface S [40]

By combining the equations 2.4 to 2.7, the EFIE becomes :

$$\sum_{n=1}^{N} \Big(- j\omega\mu + \frac{1}{j\omega\epsilon}\nabla\nabla \Big) \cdot \int_S I_n \frac{e^{-jk|\bar{r}-\bar{r}'|}}{4\pi \mid \bar{r} - \bar{r}' \mid} \bar{f}_n \, dS = \bar{E}^{inc}_{tan} \tag{2.8}$$

The unknown weighting coefficients are then calculated with the Galerkin testing, i.e. the basis functions are used as testing functions. Equation 2.8 becomes a system of N equations with N unknowns :

$$\begin{bmatrix} & \vdots & \\ \dots & Z_{mn} & \dots \\ & \vdots & \end{bmatrix} \begin{bmatrix} \vdots \\ I_n \\ \vdots \end{bmatrix} = \begin{bmatrix} \vdots \\ V_m \\ \vdots \end{bmatrix} \tag{2.9}$$

with m,n=[1,2,...,N]
where,

$$Z_{m,n} = \int_S \bar{f}_m(\bar{r}) \Big(- j\omega\mu + \frac{1}{j\omega\epsilon}\nabla\nabla \Big) \cdot \int_{S'} \frac{e^{-jk|\bar{r}-\bar{r}'|}}{4\pi \mid \bar{r} - \bar{r}' \mid} \bar{f}_n(\bar{r}') \, dS' \, dS$$

$$V_m = \int_S \bar{f}_m(\bar{r}) \cdot \bar{E}^{inc}(\bar{r}) \, dS$$

Once the unknown weighting coefficients are computed, the surface currents are calculated with equation 2.4 and the impedance matrix Z is known. The fields can be obtained by knowing the equivalent surface currents as explained in the following section.

2.4.2 Surface equivalent and fields equivalent principle for dielectric material

This explanation of the Surface equivalent principle is an abstract of the thesis of Radu [40]. Therefore, the equations, the Figures, and a deeper explanation can be found in his work.
When an electromagnetic field is emitted on a dielectric body of permittivity ϵ_{in} and permeability μ_{in}, the field can be represented with equivalent sources. Thus, two fictive equivalent currents are created: the equivalent surface current density $\bar{J}$ linked to the magnetic field $\bar{H}$ and the magnetic surface current density $\bar{M}$ linked to the electric field $\bar{E}$. Taking $\hat{n}$, the external normal pointing outward of the body, the expression of the surface currents are :

$$\bar{J} = \hat{n} \times \bar{H} \tag{2.10}$$

$$\bar{M} = \bar{M} \times \hat{n} \tag{2.11}$$

The equivalent surface currents generate fields that add up to the incident field. Assuming homogeneous mediums inside and outside the volume, $\bar{J}$ and $\bar{M}$ can be set such as the theoretical resultant field is equal to the original field outside the volume and is null inside the volume. Imposing the continuity of tangential electromagnetic fields along the surface of the dielectric object:

$$\hat{n} \times \bar{E}^{in} = \hat{n} \times \bar{E}^{out} \tag{2.12}$$

$$\hat{n} \times \bar{H}^{in} = \hat{n} \times \bar{H}^{out} \tag{2.13}$$

the free-space Green's function can be used to calculate the surface currents. The full demonstration is presented in the thesis [40].
In the case of this section, the fields outside the volume can be computed from $\bar{J}$ and $\bar{M}$ thanks to the field equivalence principle : *"Two sources producing the same field within a given region of space are said to be equivalent within that region"* [10]. The uniqueness theorem ensures that fields are the initial emitted ones.

2.4.3 Optimization

Using previous steps, the MoM code computes initial values for the electric components. Those values result in a field, for which a metric that represents the local homogeneity, is computed. These three steps of value selection, field calculation and metric calculation are repeated several times in order to minimize the objective function which is one of the metrics presented in Section 2.5. However, the Method of Moments is time consuming, and the optimization is done over several steps. In order to keep an acceptable computation time, the fields of the optimization steps are calculated with the open circuit pattern, explained in Section 2.4.4. The optimization ends when no improvement is booked or after a certain amount of iterations.

The objective metric is the only part that will be modified in this thesis for the optimization step. The initial objective function of this optimization reflects the homogeneity over the whole region, defined by a normalized standard deviation (SD). In order to improve the local homogeneity in the region of interest, different standard deviations are used in this thesis to include the weight matrix in the objective function.

2.4.4 Open circuit pattern

This explanation of the Open circuit pattern is an abstract of the paper of C. Craeye and D. González Ovejero [8]. Therefore, the equations, the definitions, and the Figures come from their work. A deeper explanation of the open circuit pattern,

its history and its usage in telecommunication can be found in this paper.
The open circuit pattern can be used to quickly calculate the fields inside the phantom when the values of the electronic components have been modified. By definition, the open circuit pattern, $\bar{f}_n^{o.c}(\hat{u})$, is the radiation pattern obtained when the elements of the array are left open except the element of interest which is excited with a unit current source, as represented in Figure 2.11. In the near field, the open circuit pattern can be set as:

$$\bar{E}_n(x, y, z) = \bar{f}_n^{o.c}(x, y, z) \tag{2.14}$$

where n is the port number [8].

Thanks to unicity, all the outside fields are uniquely determined when the Thevenin currents are known at the edge of the antennas (horizontal arrows in Figure 2.11).

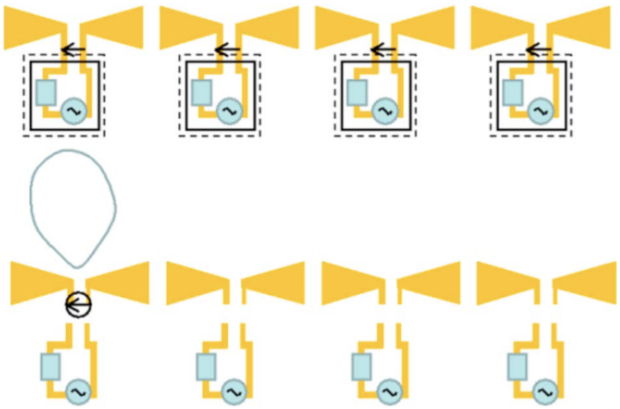


Figure 2.11: Array with (top) generators model and (bottom) open circuit pattern model [8]

Denoting the port currents by e_n, the corresponding voltage sources become :

$$v_0^n = (Z + Z_L)e_n \tag{2.15}$$

Because all elements of e_n are zero, except for a unit entry at element n, Z_L is a diagonal matrix composed by the array terminations. The open circuit pattern is rewritten :

$$f_p^{o.c}(x, y, z) = (Z + Z_L)f_p^e(x, y, z) \tag{2.16}$$

with p referring to the polarization and f_p an N-element column vector (one entry per antenna) [8].

Once the open circuit pattern for the initial step of the optimization is calculated, the fields of the following steps can be calculated based on the impedance matrix

$$f_p^e(x, y, z) = (Z + Z_L)^{-1} f_p^{o.c}(x, y, z) \tag{2.17}$$

The computation of the new impedance matrix of the Birdcage, with the electronic components of the step, is much less time-consuming than the Method of Moments.

2.5 Weighted SD and other metrics

Understanding how the weighted matrices are created and the different steps of the MoM code is key in understanding how the main objective of this thesis is implemented. However, the metric or objective function which must be optimized has not been described yet. This is what this last section is; a mathematical and intuitive description of the four different metrics used throughout this thesis. Their impact and effectiveness will be discussed in Chapter 3.

It is important to note that the metrics definitions are note changed or optimized during the optimization step. Only the components values can be chosen, resulting in different fields and different metric value. The MoM code will not optimize the field itself, it will choose the option with the lowest value.

2.5.1 Normalized standard deviation

The first metric is the one used until now in the MoM code; the normalized standard deviation, described as:

$$s_N = \sqrt{\frac{\sum_{i=1}^{N}(x_i^n - \bar{x^n})^2}{N}} \tag{2.18}$$

with x_i^n the value of the obtained normalized field at index i. And with $\bar{x^n}$ the average value of the obtained normalized field. The SD is widely used in statistics and measures the amount of variation or dispersion of a set of values [3].
In a more intuitive phrasing, this metric gives the homogeneity of a cut in the brain without any distinction for local regions of the brain. When using this metric as objective function in the optimization step, it will be referred to as $SD0$.

2.5.2 Weighted standard deviation

The second metric takes the weight matrix into account. As we can see below each element i has its normalized weight w_i^n taken into account when computing the

standard deviation:

$$s_N = \sqrt{\frac{\sum_{i=1}^{N} w_i^n (x_i - \bar{x})^2}{N}} \tag{2.19}$$

Again, a more intuitive description is given. Using weights, a term of the SD will have a bigger (smaller) impact when its weight w_i^n is bigger (smaller) than another term. This way, field values inside the ROI will impact the SD in a more important way. Hence, this metric is more representative of the homogeneity in the ROI than in the whole region. Therefore, a lower metric indicates a more homogeneous ROI. When using this metric as objective function in the optimization step, it will be referred to as $SD1$.

2.5.3 Normalized field difference

This time, instead of taking the normalized standard deviation with the mean as reference, the desired field-value F_d is introduced. This desired field F_d is represented by the weight matrix. Using the normalized values of both the obtained field and weight matrix is important, otherwise the weight matrix would have almost no impact at all due to the important difference in order of magnitude. Instead of looking at the homogeneity, it is now the desired field values, and its shape, that are of interest. The problem can be described as follows:

$$\min \int (F - F_d)^2 dV \tag{2.20}$$

Indeed, over the whole volume V, the difference between the obtained field F and the desired field F_d has to be minimized. The integral can be rewritten as:

$$\int (F - F_d)^2 dV = \int |F|^2 dV + \int -2FF_d dV + \int F_d^2 dV \tag{2.21}$$

The obtained field is normalized to have the same energy as the desired distribution and becomes $F' = \alpha F_d$. This leads to:

$$\int |F'|^2 dV = \int |F_d|^2 dV \cdot \alpha^2 \tag{2.22}$$

The problem is then described as:

$$\max \int F' F_d dV \tag{2.23}$$

The implementation of it follows the style from previous metrics:

$$s_N = \sqrt{\frac{\sum_{i=1}^{N} (x_i^n - x_i^{nd})^2}{N}} \tag{2.24}$$

with x_i^{nd} the normalized value of the desired field at index i. And with x_i^n the normalized value of the obtained field at index i. When using this metric as objective function in the optimization step, it will be referred to as $SD2$.

2.5.4 Hybrid weighted difference

Finally, the last metric is an hybrid version of the two newly introduced metrics above. The normalized weights add an importance to define the ROI in which the obtained field has to suit the desired field as much as possible.

$$s_N = \sqrt{\frac{\sum_{i=1}^{N} w_i \cdot (x_i^n - x_i^{nd})^2}{N}} \tag{2.25}$$

with x_i^{nd} the normalized value of the desired field x_i^d at index i. And with x_i^n the normalized value of the obtained field x_i at index i. When using this metric as the objective function in the optimization step, it will be referred to as $SD3$.

2.5.5 Comparison of results

The previous sections presented the four versions of metrics that are used to pick the best suited values of the components. But once those are chosen, a general definition valid for each case (identical for each case) to compare the results is needed. This metric was already present in the MoM code and was used to assess the homogeneity. The normalized SD divided by the average, referred to as SD throughout this thesis, is used.

$$s_N = \sqrt{\frac{\sum_{i=1}^{N} (x_i - \bar{x})^2}{N}} \tag{2.26}$$

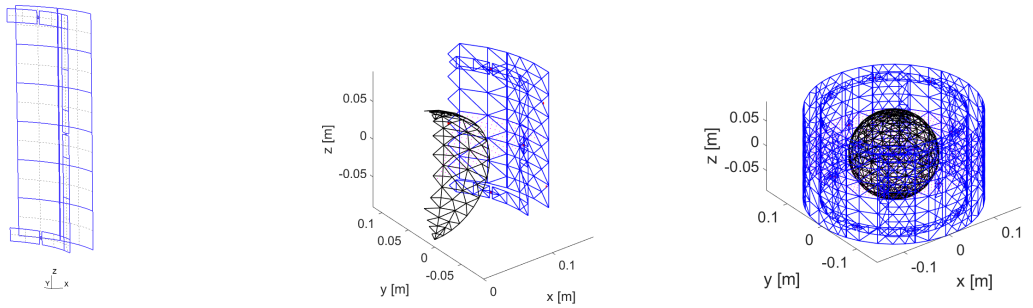
$$s_{avg} = \frac{s_N}{avg} \tag{2.27}$$

The mathematical definition of SD and $SD0$ are similar ($SD0$ has no division by the average however), but there are two important distinction. $SD0$ is used in the optimization step to chose the best field, while SD is used to compare the fields obtained using the different metrics. Besides this, $SD0$ is always defined over the whole region. SD on the contrary can be used in specific regions as well to get the localized homogeneity value.

2.6 Symmetry

As mentioned in previous sections, the use of the symmetry of the problem can be handy. The symmetry of the problem is a consequence of the symmetry of the Birdcage structure. As seen in Section 1.6, the Birdcage is a repetition of N_l legs making it symmetrical. When taking the same values for both capacitors on each leg, an extra symmetry plane appears as well as the notion of the unit cell. It is however the first symmetry that is the most used to simplify the computations, but

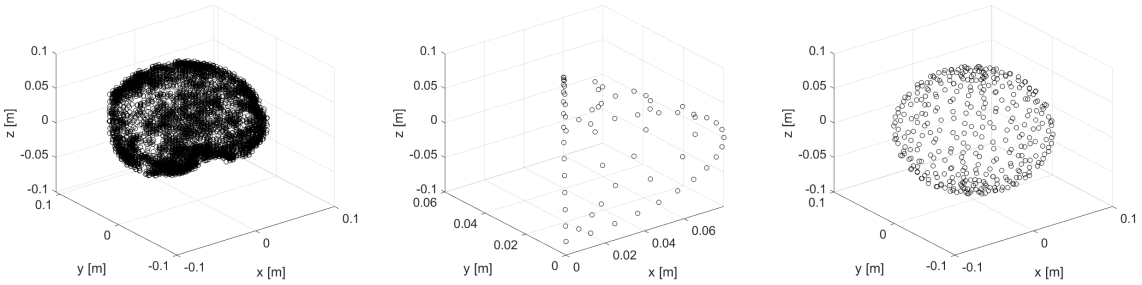
also designing steps in GMSH as seen in Figure 2.12 on the left. Indeed, each time only $1/N_l$ of the whole Birdcage has to be drawn or computed. This simplification will however lead to generalization; the use of a symmetric phantom to represent the brain is the biggest approximation. This is visible in Figure 2.12 and is discussed in a paragraph below.



(a) GMSH (b) Symmetry in Mesh (c) Complete Mesh

Figure 2.12: Symmetry exploited in the MoM code

Simplified brain representation The first example, given in Figure 2.4, of the weight matrix adapted to the shape of the brain is a non-symmetric brain. As mentioned just before, this is now not possible anymore as a symmetric phantom is needed. Instead of a brain representation, as used for Figure 2.4 and presented left in Figure 2.13, a perfect sphere is now used. As shown in Figure 2.13 at the center and right, this sphere is made of N_l (8 in this case) symmetric parts. This can also be seen in Figure 2.12.

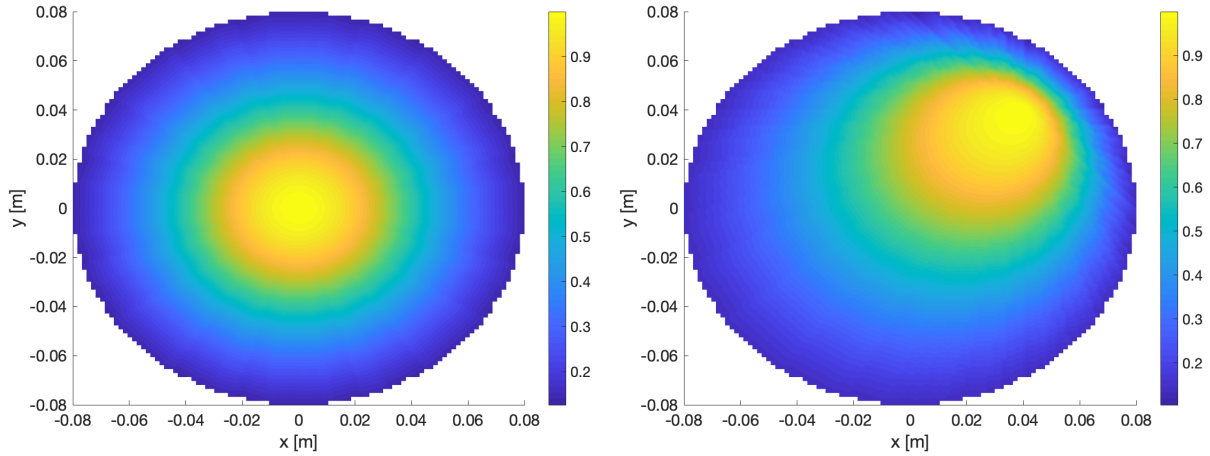


(a) Complete Brain (b) Symmetry in sphere (c) Complete sphere

Figure 2.13: Symmetry in phantom

Weight matrix in sphere In this last paragraph about symmetry, the symmetric sphere is used when applying the Gaussian weight matrix. Both centered and

not-centered versions are given to show the changes in weight values when changing the center of the ROI.



(a) Centered Gaussian (b) Off centered Gaussian

Figure 2.14: Weight matrix in sphere

2.7 Verification using S-parameters

To validate the obtained results, their S-parameters are analyzed. Those Scattering-parameters describe the electrical behavior. S-parameters analysis helps to see the main mode of the Birdcage and simultaneously other resonant modes of this LC-resonator. When an antenna is matched three possible outcomes arise: a perfectly matched case, a high couple effect and lastly sometimes a frequency shift appears. Those three cases are presented in the following sections using Figure 2.15.

Optimal case An optimized case is distinguished by a local minimum both for S_{11} and S_{12}. Indeed, a low S_{11} means the antenna is matched. Without a matched antenna, no resonance is present. Adding to this a low S_{12} indicates a low coupling. As made clear during discussions with Farzad Jabbari Gargari, coupling issues are mainly considered for the SAR evaluation. In this example, the optimal frequency is 300 [MHz]. In such cases, the results are considered acceptable and suited for the problem. It is however important to clarify that no correlation exists between the homogeneity and the S-parameters. A case with acceptable S-parameters does not automatically have improved homogeneity.

Coupled case When an antenna is matched, i.e. S_{11} is low, there is no certainty of an optimal case. Indeed, coupling appears when a high value for S_{12} is present. On Figure 2.15 a frequency of 250 [MHz] is a perfect example. A low S_{11} indicates resonance, but the high S_{12} means coupling is present. Again, no correlation between homogeneity and S-parameters exists. This will be confirmed in Chapter 3.

Frequency shift The last possibility is to have a frequency shift, with 290 [MHz] or 310 [MHz] as perfect example. In MRI it is expected for the RF coil to have its sharp frequency similar to the Larmor frequency (around 64 [MHz] for 1.5 [T], 200 [MHz] for 4.7 [T], 300 [MHz] for 7 [T], ...). For those frequencies the optimal case is required. However, a frequency shift around 10 [MHz] is acceptable as it can be compensated with tuning. The amelioration of these cases can be an interesting perspective for the future.

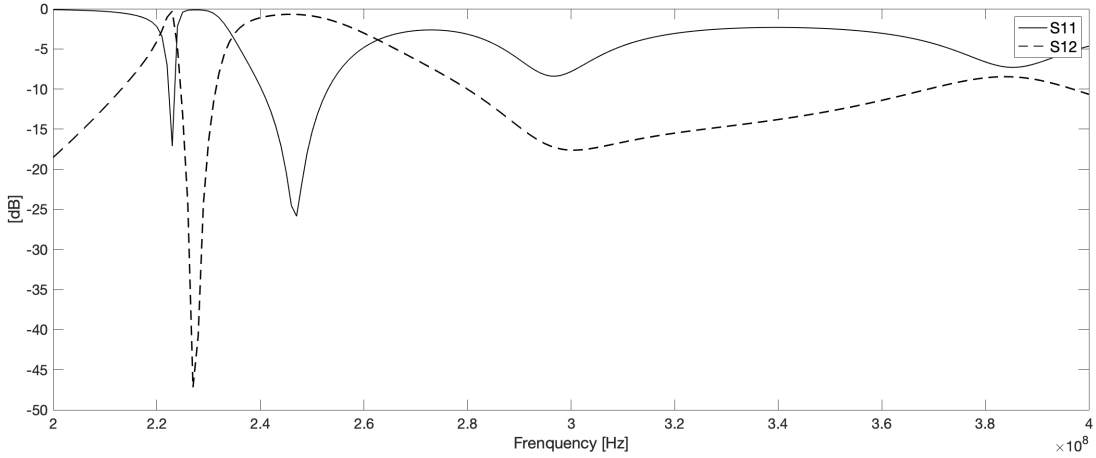


Figure 2.15: S Parameters

Chapter 3

Weight matrix used on the Conventional Birdcage

Chapter 3 outlines the studies that have been conducted in order to focus the fields on the lobes of the brain. After an analysis of the 8-legged Conventional Birdcage, the homogeneity of the fields was adapted with a torus weight matrix in the symmetrical Birdcage. This symmetric case is used to confirm the feasibility of the approach. Then, the Birdcage was modified to be asymmetrical and three different Gaussian weight matrices were used to focus on different regions of the brain. Besides different weight matrices, different SDs are used. The three SDs used in this step are explained in section 2.5 and can be summarized as the weighted SD, the field difference SD and the hybrid version.

Each case is presented as follows: first, the goal of the study is explained and the weight matrix is shown. Then, the results are exposed with the values of the capacitors, the spatial representation of the SAR efficiency defined as $(B^+/(SAR)^{1/2})$ and the spatial representation of the Electric field (E). The S-parameters are used as a posteriori check. Assessing the local SAR in the whole head shows slightly different values for each case. One can conclude that safety is provided as the limit of 4 [W/kg] is respected. Let us note that while the S-parameters go from 200 [MHz] to 400 [MHz], and sometimes show optimized behavior for other frequencies than the frequency of interest 300 [MHz], all fields are the ones obtained for this specific frequency of 300 [MHz].

After that, the results are analyzed and compared with the basic cases. Finally, a conclusion of the study is drawn.

3.1 8-legged Conventional Birdcage

The Basic Birdcage design was presented in section 1.6. However, some parameters were kept as constants to give a more general description. This section specifies the values used in this thesis.

First of all, a high-pass (HP) 8-legged 7T Birdcage was used, meaning N=8 as represented in Figure 3.1. As there are 8 legs, the angle between them is $\varphi = 2\pi/N = \pi/4$. Therefore, this Birdcage design contains 16 capacitors. The positions correspond to the HP configurations i.e. on both the top and bottom end-ring segments but not on the legs. However, at the center of the legs are the inductive excitation ports. While each leg is designed with such a port, only two of them are used. In this way the resonance conditions are respected [22]. All simulations are realized at a frequency of interest of 300 [MHz], equivalent to around 7T.

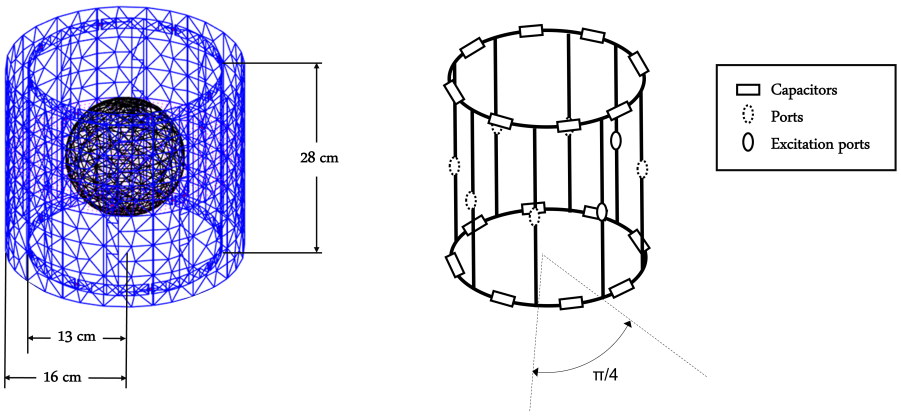


Figure 3.1: 8 legged Birdcage

The dimensions of the Birdcage are indicated in Figure 3.1. It has a height of 28 [cm] with the ports located in the middle i.e. 14 [cm]. While the shield has a radius of 16 [cm], the Birdcage itself has a radius of 13 [cm]. As a result, the end-rings have a circumference of 81.68 [cm] and the Birdcage a total volume of 14866.02 [cm^3]. The symmetric sphere used as a phantom has a radius of 8 [cm] resulting in a volume of 2144.66 [cm^3]. The conductivity (σ) and the relative permittivity (ϵ_r) of the phantom were set to 0.86 [S/m] and 45.3, respectively. The average brain has a length of 15 [cm] and is therefore well approached by the phantom. However, the average brain volume is only 1200 [cm^3].

3.2 Symmetric case

The symmetric case is named so as both the Birdcage, its capacitors values and the used weight matrices are symmetric. Therefore, the Birdcage shown in Figure 3.2 has only 2 capacitors values, C_1 and C_2, repeated in each leg. The symmetry allows faster and lighter computation and is a useful milestone before switching to the non-symmetrical Birdcage. This case is used to analyze the feasibility of the approach described in Chapter 2. Therefore, only the weighted SD, $SD1$, will be used on three different but similar weight matrices.

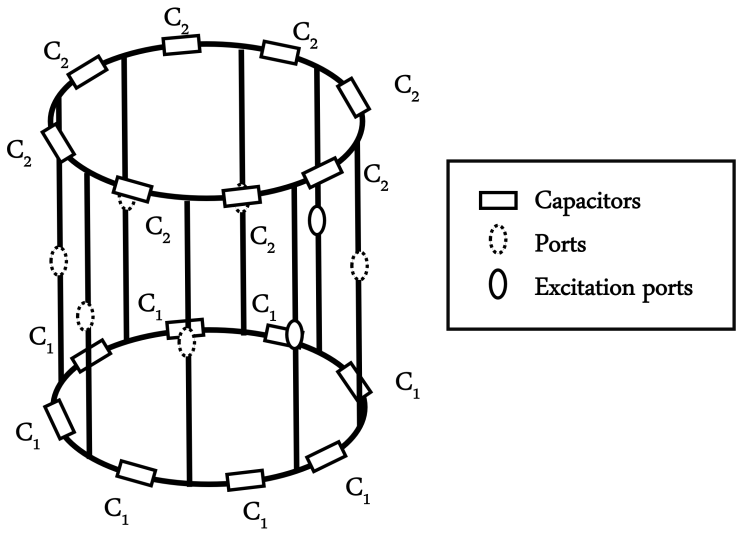


Figure 3.2: Capacitors of symmetric Birdcage

3.2.1 Basic symmetric case

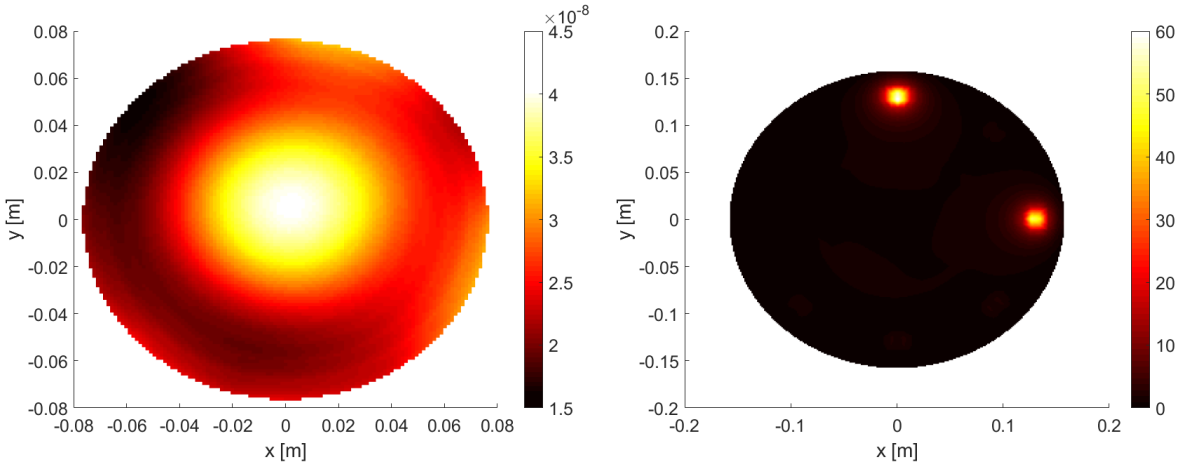
Before tackling a first case using the approach defined in Chapter 2, a quick overview of the basic case will allow the reader to understand where this thesis starts from and some issues associated with it. In this case all capacitors have the same value, but one sits below and one above the horizontal symmetric plane introduced in 1.6.5. Besides this, the metric used in the optimization step is the standard deviation $SD0$ over the whole volume. Hence, no weight matrix is taken into account and no ROI is defined. The goal is to optimize the homogeneity over the whole phantom.

Results and analysis

The resulting SAR efficiency and electric field are represented in Figure 3.3. while its C-values and SD (over the whole region denoted ROA) are presented in Table 3.1.

SD ROA	C_1 [F]	C_2 [F]
0.2298	8.32e-13	8.32e-13

Table 3.1: Basic symmetric case



(a) $\frac{B_1}{SAR^{1/2}}\left[\frac{T}{\sqrt{W/Kg}}\right]$ (b) $E\ [\frac{V}{m}]$

Figure 3.3: SAR efficiency and Electric field distribution of the basic symmetric case

As expected, despite an acceptable global homogeneity (translated by a low SD in the ROA), the SAR efficiency is centered and not homogeneous on the sides as shown in Figure 3.3a. Indeed, two small regions have values of around $3 \cdot 10^{-8}\left[\frac{T}{\sqrt{W/Kg}}\right]$ while the rest of the sides has values around $2 \cdot 10^{-8}\left[\frac{T}{\sqrt{W/Kg}}\right]$. The main cause of this inhomogeneity on the sides are the (active) excitation ports. While they were presented as an advantage to create the resonance above, they create non-negligible hotspots (in yellow) in the E-field on the right and at the top in Figure 3.3b. Those translate into increased SAR efficiency values. An increase in this field does not represent any threat, but its inhomogeneity does. Therefore, the results of an MRI

of the temporal lobes could be impaired.

This basic case is used as a reference when analyzing results obtained with this thesis approach. Both the visual aspect and numerical aspect help understand the improvements brought by the approach.

S-parameters analysis

This is the basic case without any modification. It goes without saying that optimized behavior is expected. Figure 3.4 confirms that it is the first case presented in section 2.7 that is effective here. So it is optimized.

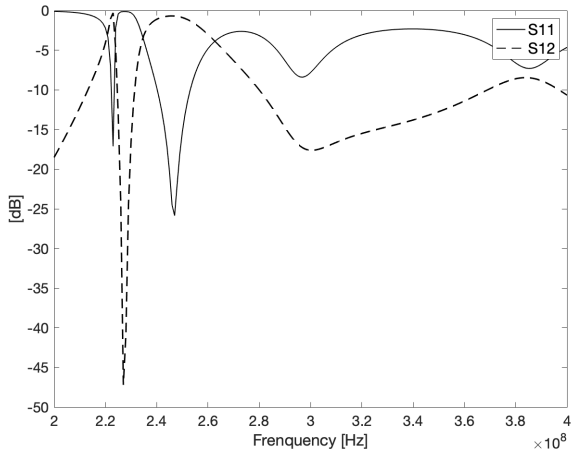


Figure 3.4: S-Parameters

3.2.2 Analysis of the Torus-shaped weight matrix case

The Torus shape is symmetrical and highlights the lobes. Its study can prove that the fields can be focused on the lobes while still using a perfectly symmetrical Birdcage.

Weight matrix

The torus weight matrix is created in two steps. First, a two-dimensional torus shape is created in the plane z=0. In order to keep the properties explained in

section 2.3, the 2D-torus is created with two types of Gaussians :

$$\mathbf{W}(\mathbf{x},\mathbf{y},\mathbf{0}) \begin{cases} exp\Big(-\frac{1}{2\cdot a}(\frac{\delta-d}{\delta})^2\Big) & \text{if d} \leq \delta, \\ exp\Big(-\frac{1}{2\cdot a}(\frac{d-\delta}{D_e})^2\Big) & \text{if } \delta < \text{d} \leq \text{D}\ , \\ 0 & \text{elsewhere}\ . \end{cases}$$

Where D becomes the distance between the center of the brain $C(x_0, y_0, z_0)$ and the edge of the brain in the direction of p(x,y,0), d becomes the distance between the center of the brain p(0,0,0) and the point p(x,y,0), D_e is the distance between the edge of the brain and the center of the torus, δ is the distance between the center of the brain p(0,0,0) and the center of the torus ($\delta = D - D_e$), and a is the attenuation factor. The distances are shown in Figure 3.5.

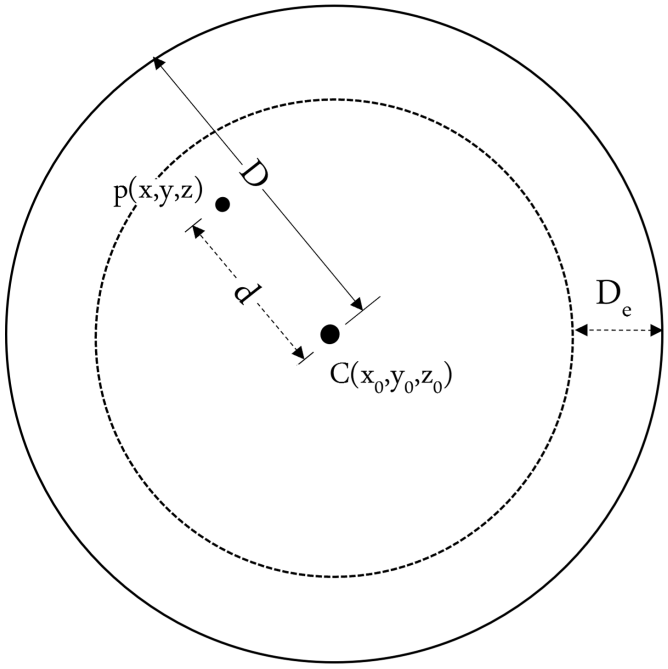
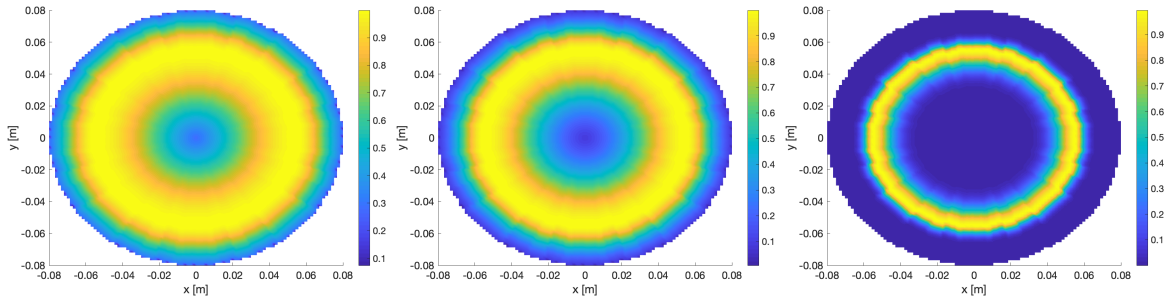


Figure 3.5: Schematic representation of d, D and D_e

The two variables a and D_e can be chosen to adapt the region of interest. Figure 3.6 shows the tree cases that have been studied : $a = 0.65$, $a = 1.25$ and $a = 12.25$. In each case the distance between the center of the phantom and the center of the torus D_e is set to 25 millimeters.



(a) $a = 0.65$ (b) $a = 1.25$ (c) $a = 12.25$

Figure 3.6: Torus weight matrix z=0 plane

The 2D torus is then vertically extended with the following Gaussian :

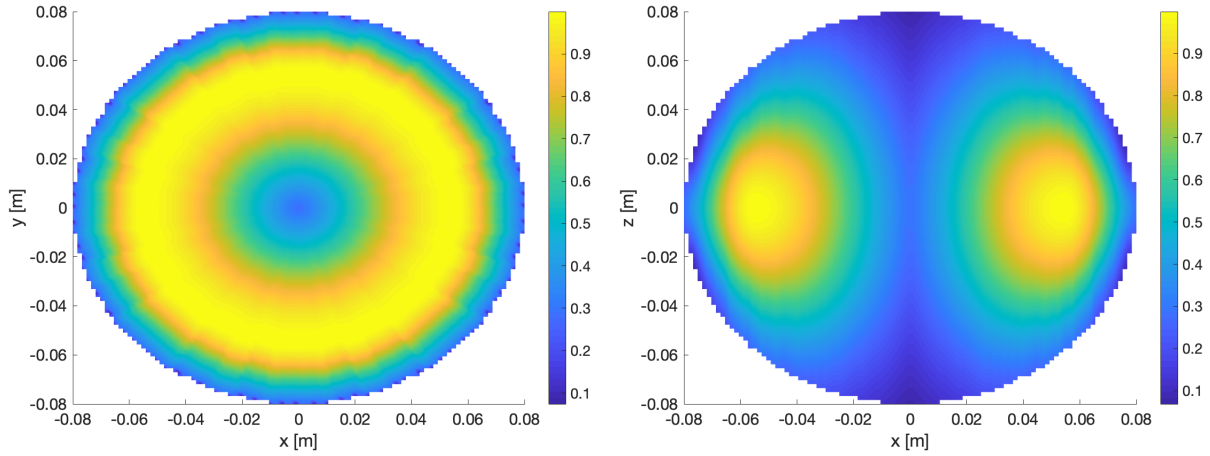
$$W(x, y, z) = W(x, y, 0) \cdot exp\Big(- \frac{1}{2 \cdot a}(\frac{z}{elev(x, y)})^2\Big) \tag{3.1}$$

where $elev(x, y)$ gives the height, z_e, of the edge point $p(x_e, y_e, z_e)$ that is the closest to the point p(x,y,z) in the X-Y domain.

The optimization problem:

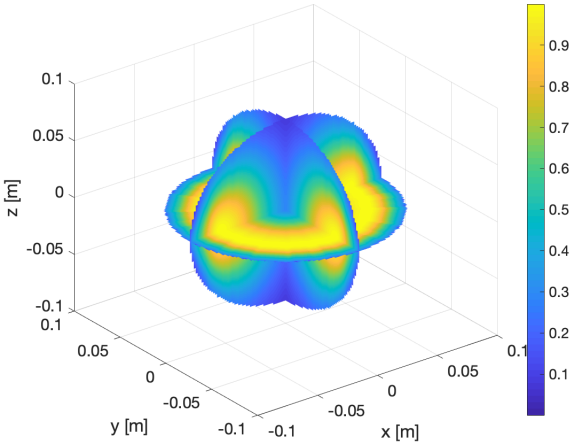
$$\min_{x_e, y_e, z_e} \sqrt{\big(x_e - x\big)^2 + \big(y_e - y\big)^2} \tag{3.2}$$

is solved using Octrees as explained is section 2.3.2.
The Torus weight matrix is so symmetric and adaptable to any convex star-shaped organ. The example of this case is shown in Figure 3.7.



(a) z=0 plane

(b) y=0 plane



(c) 3D representation

Figure 3.7: Torus weight matrix with a=0.65

Results and analysis

As mentioned in the methodology, the weights are used together with the metrics $SD0$, $SD1$, $SD2$ and $SD3$ to optimize the field distributions. At the end of Chapter 2, the use of the normalized SD to compare results was introduced. Indeed, in order to understand the impact of this approach the obtained fields are compared in the regions specified by the weight matrix. The goal of the symmetric case being to investigate if encouraging results are obtained using this approach, only the weighted standard deviation alias $SD1$ was used. For this first case, the optimized values of the capacitors obtained using the MoM code are presented in Table 3.2. The symmetrical configuration of the Birdcage yields identical values for each capacitor. The use of different weight matrices is translated into different capacitors values

for each weight matrix. The capacitors values have slightly increased compared to the Basic case.

Capacitors \ Weights	$D_e = 0.025$ [m] $a = 0.65$	$D_e = 0.025$ [m] $a = 1.25$	$D_e = 0.025$ [m] $a = 12.25$
C_1 [F]	1.03e-12	1.02e-12	1.01e-12
C_2 [F]	1.03e-12	1.02e-12	1.01e-12

Table 3.2: Electronic components value

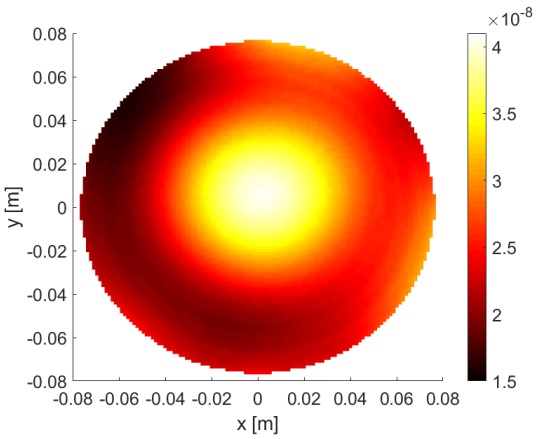
The distributions of the E-field resulting from those capacitor values are represented in Figures 3.8b, 3.8d and 3.8f. The impact of the excitation ports mentioned before is clearly visible.

Besides the E-field, the SAR efficiency is presented in Figures 3.8a, 3.8c and 3.8e. This field can be analyzed in three ways. First, the values are of the same order as the basic case. This is essential in order to obtain images. Secondly, its shape. The already present torus shape is slightly improved, hence following the weight matrix. Lastly, its homogeneity. This is the most important part of the analysis and is done using the SD in different regions. The SD in the ROI for each case is presented in Table 3.3.

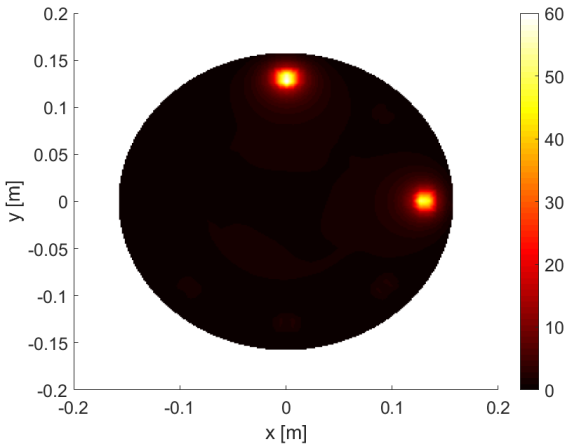
Case \ Weights	$D_e = 0.025$ [m] $a = 0.65$	$D_e = 0.025$ [m] $a = 1.25$	$D_e = 0.025$ [m] $a = 12.25$
Basic case	0.1803	0.1803	0.1803
$SD1$	0.1598	0.1600	0.1601

Table 3.3: Homogeneity in ROI

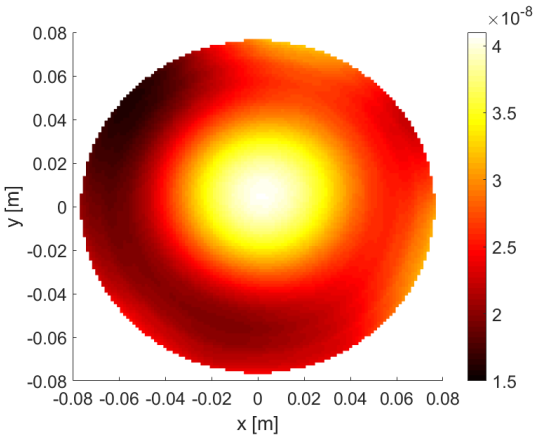
All cases show an increase in homogeneity translated by a decrease of the SD. The difference in attenuation factor a does not affect the SD value in a significant way, as for the three cases an improvement of around 10% is obtained.



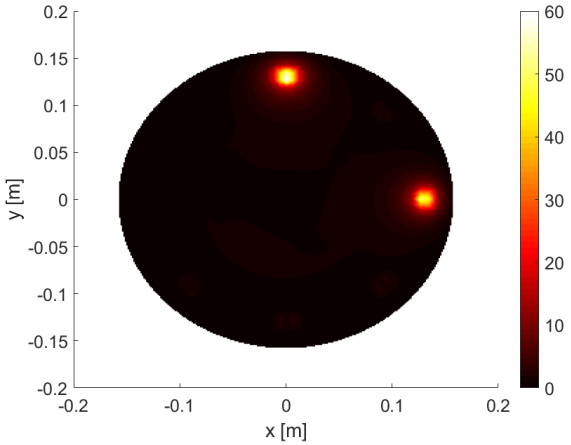
(a) $\frac{B_1}{SAR^{1/2}}\left[\frac{T}{\sqrt{W/Kg}}\right]$ with $a = 0.65$



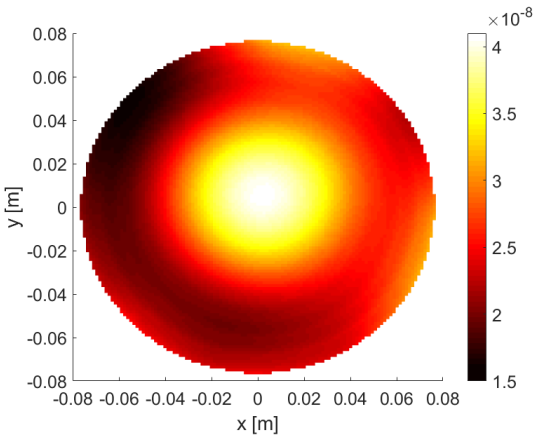
(b) $E\ [\frac{V}{m}]$ with $a = 0.65$



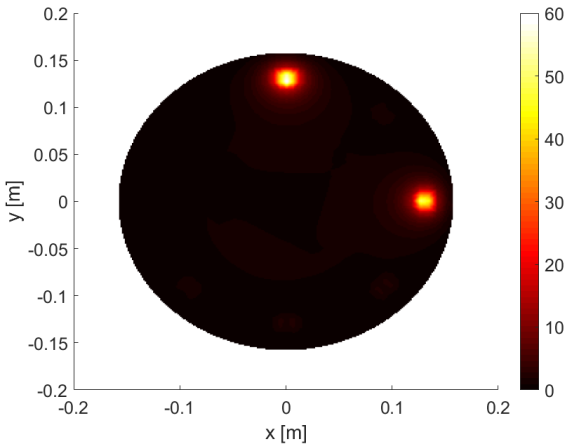
(c) $\frac{B_1}{SAR^{1/2}}\left[\frac{T}{\sqrt{W/Kg}}\right]$ with $a = 1.25$



(d) $E\ [\frac{V}{m}]$ with $a = 1.25$



(e) $\frac{B_1}{SAR^{1/2}}\left[\frac{T}{\sqrt{W/Kg}}\right]$ with $a = 12.25$

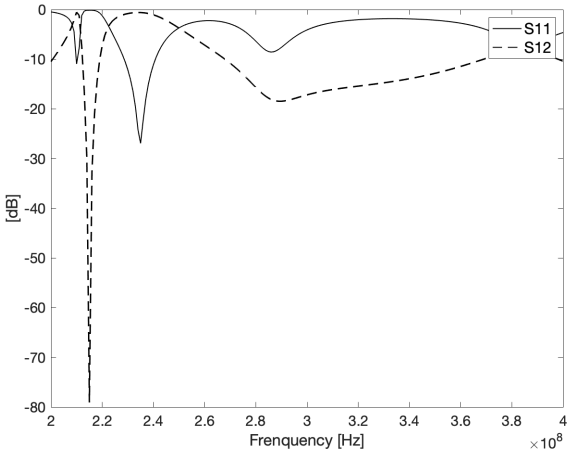


(f) $E\ [\frac{V}{m}]$ with $a = 12.25$

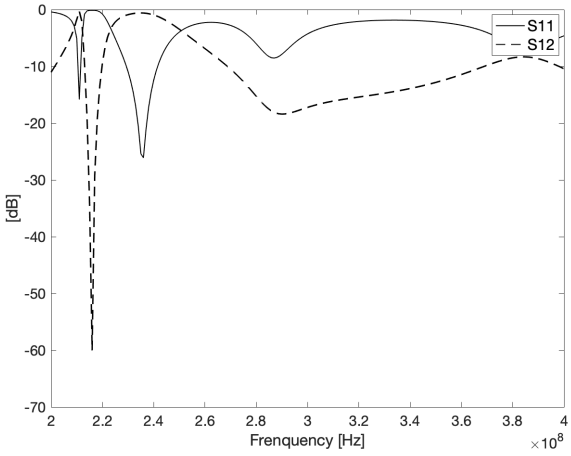
Figure 3.8: SAR efficiency and Electrical field distribution of symmetric torus case

S-parameters analysis

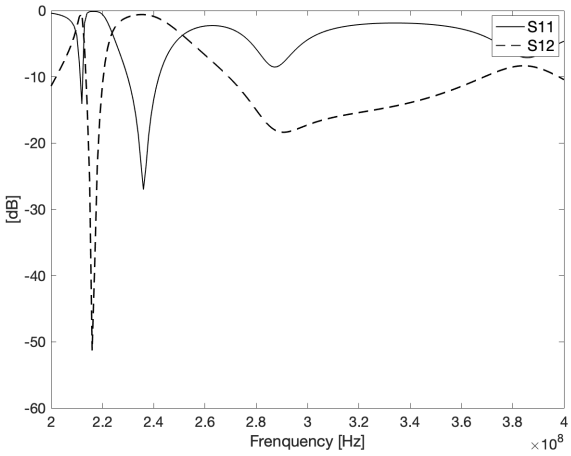
All three cases have similar S-parameters, presented in Figure 3.9. At first glance, they can be considered to be optimized. However, the optimal frequency is a bit off, being here 290 [MHz]. Nevertheless, they remain acceptable.



(a) a=0.65



(b) a=1.25



(c) a=12.25

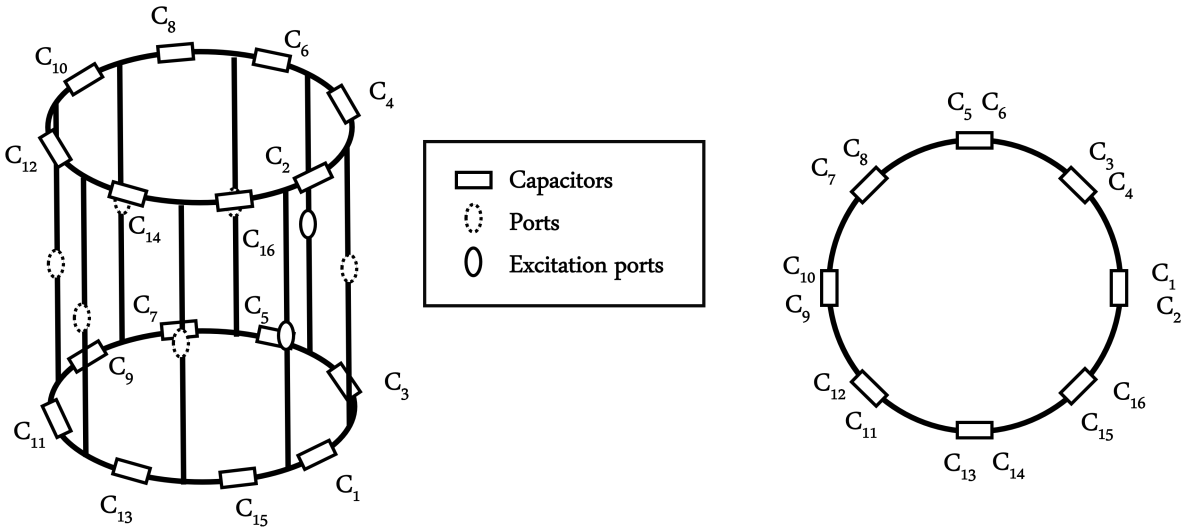
Figure 3.9: S-Parameters

3.2.3 Conclusion

As mentioned before, each case improves the homogeneity by around 10%. It is clear that this approach delivers encouraging results and will be deepened for the asymmetric case. In all three cases, the influence of the excitation ports is present and cannot be counteracted as it is a symmetric case. Besides the homogeneity improvements, the cases remain matched as the S-parameters show.

3.3 Asymmetric case

The symmetric case showed the feasibility of the approach. As shown in Figure 3.10, the Birdcage can be made asymmetric by choosing different values for each capacitor (C_1-C_{16}). The asymmetric case will dive deeper into the possibilities it offers, one of them being the ability to counteract the effect of the excitation ports mentioned in the symmetric case, resulting in an improved homogeneity of the ROI. At the end of this section, various cases highlighting the possibility of locating the homogeneity improvement as desired will have been presented. This will open the door to the application of this approach to concrete cases.



(a) Position of capacitors (b) View from top

Figure 3.10: Capacitors of asymmetric Birdcage

3.3.1 Basic asymmetric case

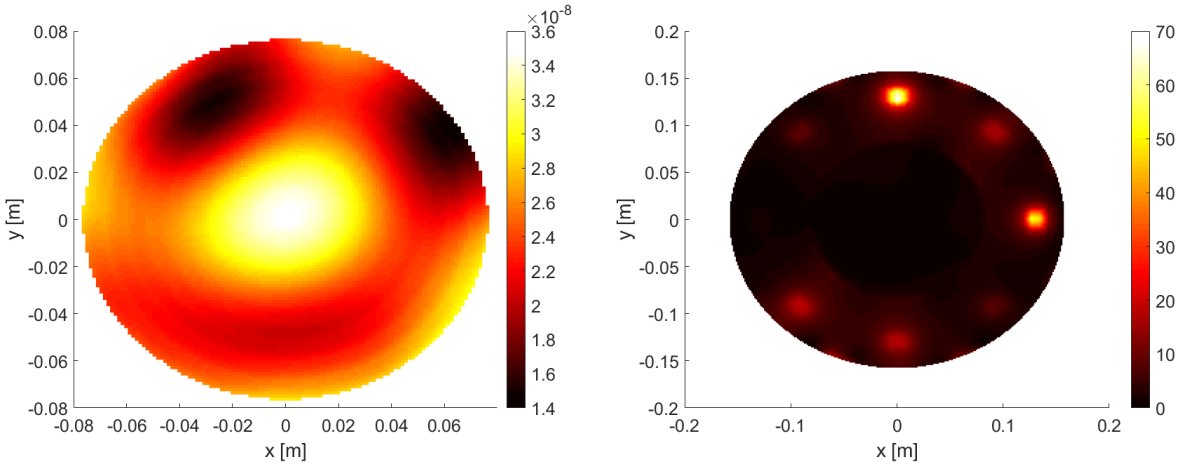
In the same way a basic case was presented in the symmetric part of this chapter, a basic asymmetric case is used as reference when comparing and analyzing results. Both the visual aspect and numerical aspect help understand the improvements brought by the approach.

As in the basic symmetric case, the metric used in the optimization step is the normalized standard deviation over the whole volume. Hence, no weight matrix is taken into account and no ROI is defined. The main goal is to optimize the homogeneity over the whole phantom.

The resulting SAR efficiency is represented in Figure 3.11a. while its C-values are presented in Table 3.4 and SD (over the whole region) in Table 3.5.

C_1 [F]	C_2 [F]	C_3 [F]	C_4 [F]	C_5 [F]	C_6 [F]	C_7 [F]	C_8 [F]
8.69e-14	9.54e-14	6.30e-12	5.92e-13	1.43e-13	8.34e-14	1.70e-12	1.17e-12
C_9 [F]	C_{10} [F]	C_{11} [F]	C_{12} [F]	C_{13} [F]	C_{14} [F]	C_{15} [F]	C_{16} [F]
1.05e-11	2.08e-12	8.35e-13	1.56e-11	5.24e-12	7.05e-13	1.52e-12	1.84e-12

Table 3.4: Electronic components value



(a) $\frac{B_1}{SAR^{1/2}}\left[\frac{T}{\sqrt{W/Kg}}\right]$ (b) $E\ [\frac{V}{m}]$

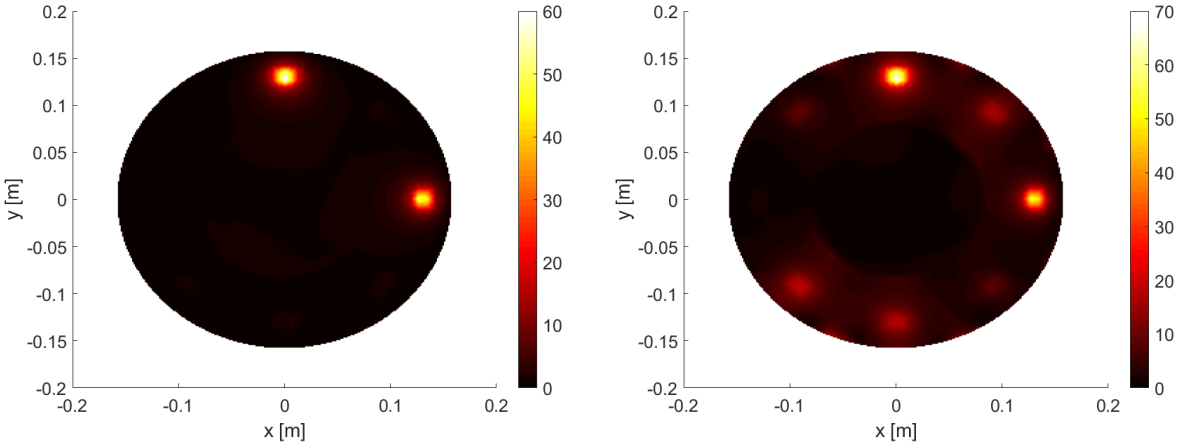
Figure 3.11: SAR efficiency and Electric field distribution of the basic asymmetric case

The main problem mentioned in the symmetric case was the presence of excitation with the Birdcage not being able to counteract their impact. With the asymmetric configuration of the Birdcage however, different C-values are feasible and can be considered as an option to counter this effect. A joint analysis of the numerical values of Table 3.4 and Figure 3.11b shows a correlation between the capacitors values and the value of the E-field.

First, let us clarify that C_1, C_2, C_5 and C_6 are the capacitors of the legs containing the excitation ports and have the lowest values. All the other capacitors are located on legs without excitation ports, and have the highest values. It can be said that

those higher values compensate the already existing hotspots in the E-field, while the lower values increase the least possible the existing hot spots while respecting the resonance conditions of the Birdcage.

While C_3, C_4, C_7, C_8, C_{15} and C_{16} improve the homogeneity near the excitation ports, the other capacitors take care of the rest of the torus-shaped region defined by the weight matrix. The difference between the resulting E-field for the symmetric and asymmetric cases is shown in Figures 3.12a and 3.12b. The average capacitors value for the asymmetric case is 4.01e-12 $[F]$ (without C_1, C_2, C_5 and C_6) while the symmetric case has 8.32e-13 $[F]$ capacitors. This is a factor 4.83 of difference, explaining the difference in E-values and visibility of the spots on the graph.



(a) Symmetric case (b) Asymmetric case

Figure 3.12: Comparison of the Electric field distribution

As Table 3.5 shows, the SD of the whole volume, denoted ROA, has decreased in the asymmetric configuration by 24.06%. It is already a significant improvement obtained thanks to the asymmetric Birdcage.

	Symmetric case	Asymmetric case
ROA	0.2298	0.1745

Table 3.5: SD for both cases

S-parameters analysis

It appears the use of an asymmetric Birdcage has a small impact on the S-parameters. They show an optimization for a frequency slightly higher than the frequency of interest, but it is still considered as an adapted case as the shift is closer than 10 [MHz].

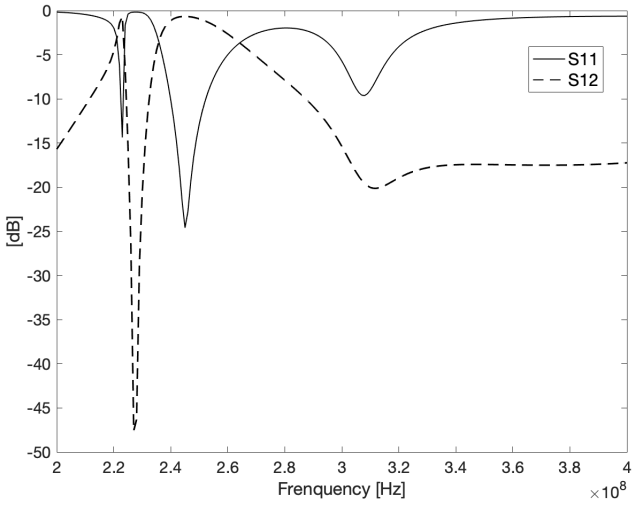


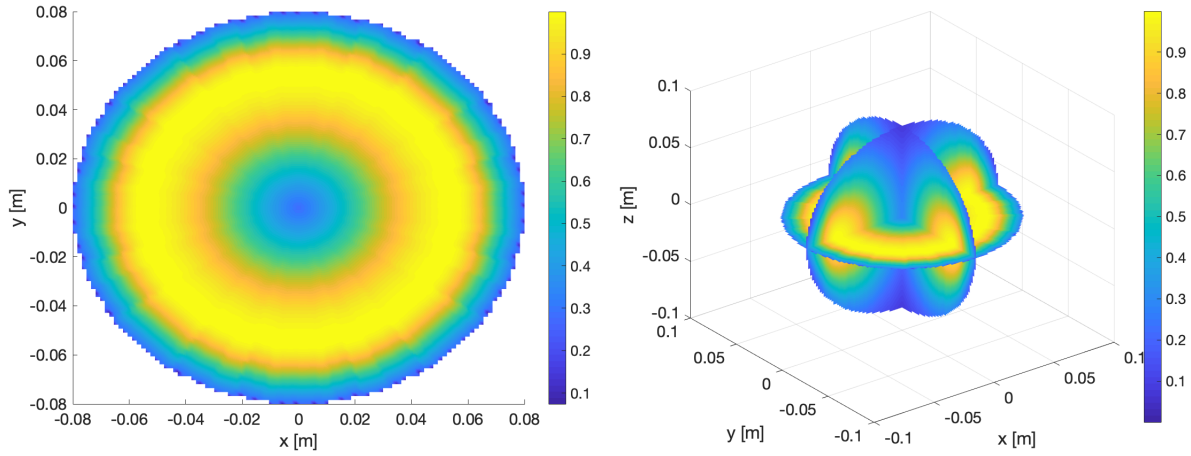
Figure 3.13: S-Parameters

3.3.2 Analysis of the Torus-shaped weight matrix case

Section 3.2.2 demonstrates that the use of weight matrices increases the homogeneity in desired regions. In a second step, the previous section showed that asymmetric Birdcages improve the homogeneity in the whole region. Therefore, the Torus case is repeated to analyze if even when using an asymmetric configuration, weight matrices come in handy and are useful.

Weight matrix

The weight matrix is the torus weight matrix presented in section 3.2.2 and in Figure 3.14. The specific values are $a = 1.25$ and D_e is set to 25 millimeters.



(a) z=0 plane (b) 3D representation

Figure 3.14: Torus weight matrix with a=0.65

Results and analysis

The optimized values of the capacitors obtained using the MoM code are presented in Table 3.6. The asymmetric configuration of the Birdcage is well translated by those values which are all different.

	C_1 [F]	C_2 [F]	C_3 [F]	C_4 [F]	C_5 [F]	C_6 [F]	C_7 [F]	C_8 [F]
$SD1$	3.12e-13	2.99e-12	2.73e-12	3.85e-13	1.86e-12	5.77e-13	1.14e-12	6.08e-13
$SD2$	5.94e-14	2.52e-12	1.11e-12	1.65e-12	8.16e-13	1.14e-12	1.045e-12	1.12e-12
$SD3$	1.01e-12	4.67e-13	2.32e-12	1.43e-12	1.98e-13	2.84e-12	2.20e-12	1.40e-13
	C_9 [F]	C_{10} [F]	C_{11} [F]	C_{12} [F]	C_{13} [F]	C_{14} [F]	C_{15} [F]	C_{16} [F]
$SD1$	4.12e-12	8.74e-14	3.05e-13	6.95e-12	1.90e-12	3.78e-13	3.25e-12	1.28e-13
$SD2$	4.82e-13	1.65e-12	9.18e-14	2.63e-12	1.49e-12	8.98e-14	9.78e-14	4.20e-12
$SD3$	2.77e-13	3.76e-12	1.53e-12	8.59e-13	5.69e-13	1.19e-12	1.39e-12	3.56e-13

Table 3.6: Electronic components value

The asymmetry effect is visible in Figures 3.16b, 3.16d and 3.16f representing the E-field distribution. While the fairly uniform distribution of the amplitude of E is reminiscent of the symmetrical character of the Torus, a variation between the different legs (and capacitors) is present. As explained before, in addition to the clearly visible impact of the excitation port, the asymmetric capacitor values are translated by varying E-fields counteracting the impact of the excitation ports. In Figure 3.16f for example, the impact of both excitation ports is visi-

ble (on the right and at the top) but other legs clearly have a more dominant impact.

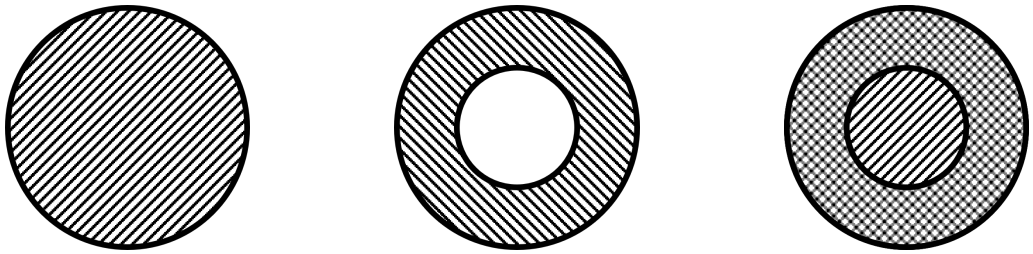
The obtained SAR efficiency, for each SD, is represented in Figures 3.16a, 3.16c and 3.16e. The order of magnitude, for each case, is similar to the basic case. A clear Torus-shaped ROI is visible in all three cases showing the effect of the weight matrix. In fact, the B-field is higher and more constant in the external zone. Moreover, the dark zone in the center of the phantom represents a smaller flux in the region of least interest. This is a noticeable difference with the basic case. Indeed, the maximum was then at the center.

The last aspect provided by the SAR efficiency is homogeneity. Table 3.7 shows the homogeneity values, expressed by SD, for each case as well as the basic case to be able to compare the improvements.

	$SD0$	$SD1$	$SD2$	$SD3$
ROI	0.1502	0.1452	0.1280	0.1483
ROA	0.1745	0.2710	0.2535	0.2690

Table 3.7: Homogeneity in ROI and ROA

Both in the region of interest (ROI) and the whole volume (ROA) a difference in homogeneity is obtained. As shown in Figure 3.15b the evolution of the field homogeneity is analyzed for the ROI which is Torus-shaped in this case. Let us note that the ROI of this shape already has a decent homogeneity compared to the homogeneity of the whole sphere in the basic case (0.1502 compared to 0.1745). Nevertheless, all three SDs increased the homogeneity of the ROI.

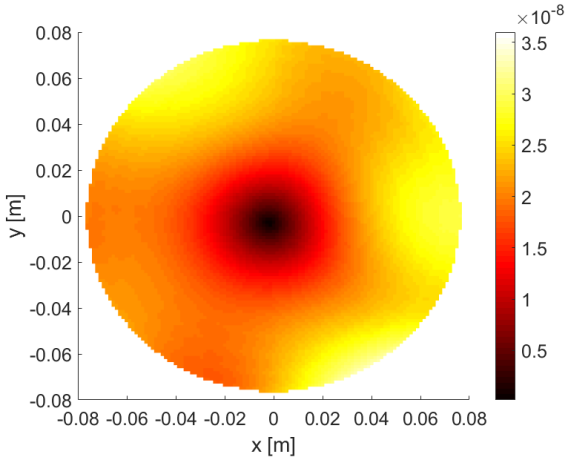


(a) ROA (b) ROI (c) Combination

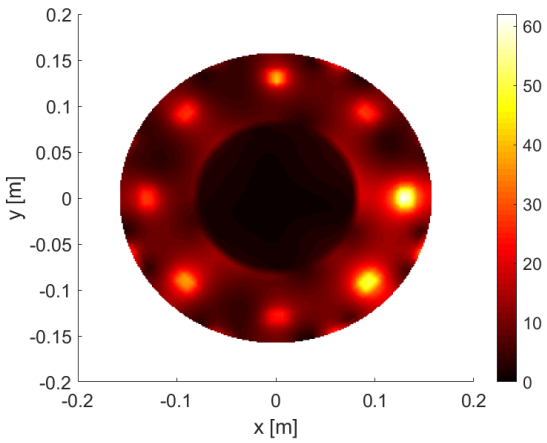
Figure 3.15: Regions of SD

This is translated by a decrease of SD in the ROI. This improvement of homogeneity in the ROI is coupled with a decrease in homogeneity in the ROA. This confirms

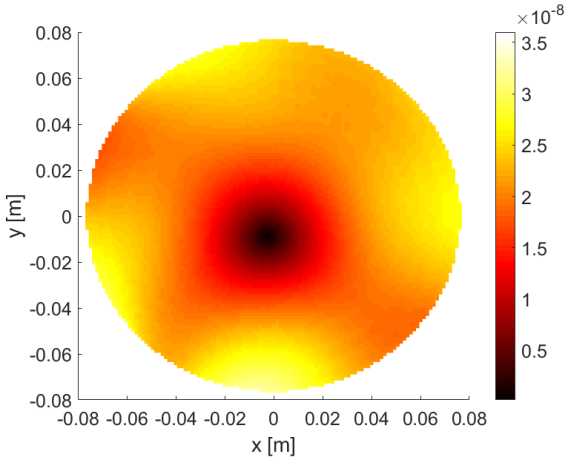
that the improvement in homogeneity is localized in the desired area. The approach used is, therefore, working and will be used in future cases to localize specific areas. Finally, in both the basic case and the analyzed case the use of an asymmetric Birdcage with different values for each capacitor helps to counteract the effect of the excitation pins as explained previously. Indeed, the ROI has a 3.29% decrease of SD for $SD1$, a 14.76% decrease for $SD2$ and a 1.22% decrease for $SD3$. On the other hand, the increase of SD in ROA is 55.32% for $SD1$, 45.27% for $SD2$ and 54.17% for $SD3$. Note that these results are compared to the asymmetric base case which is already an improvement of the symmetric base case.



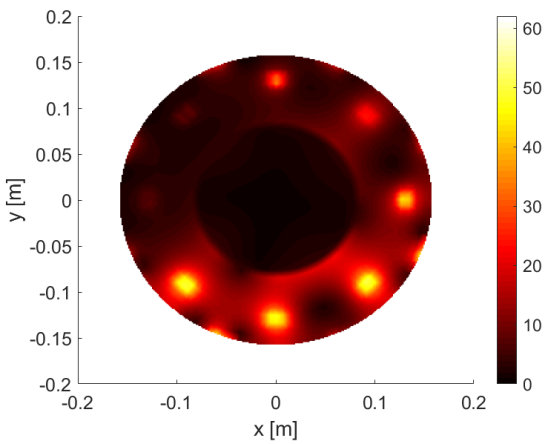
(a) $\frac{B_1}{SAR^{1/2}}\left[\frac{T}{\sqrt{W/Kg}}\right]$ with $SD1$



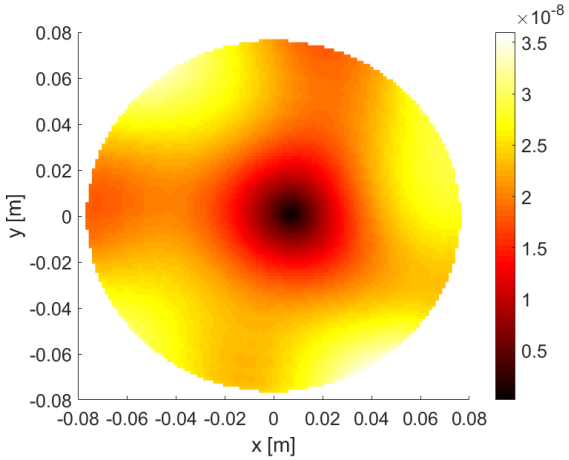
(b) $E\ [\frac{V}{m}]$ with SD1



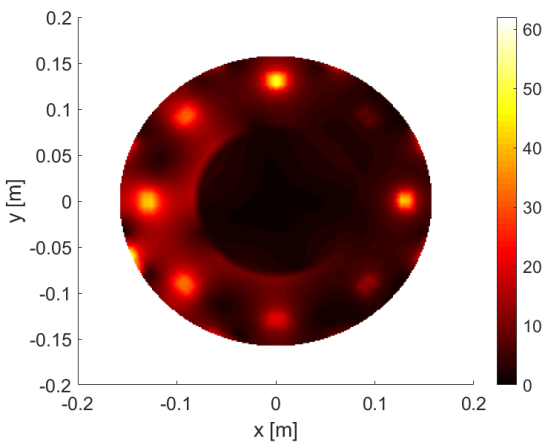
(c) $\frac{B_1}{SAR^{1/2}}\left[\frac{T}{\sqrt{W/Kg}}\right]$ with $SD2$



(d) $E\ [\frac{V}{m}]$ with $SD2$



(e) $\frac{B_1}{SAR^{1/2}}\left[\frac{T}{\sqrt{W/Kg}}\right]$ with $SD3$

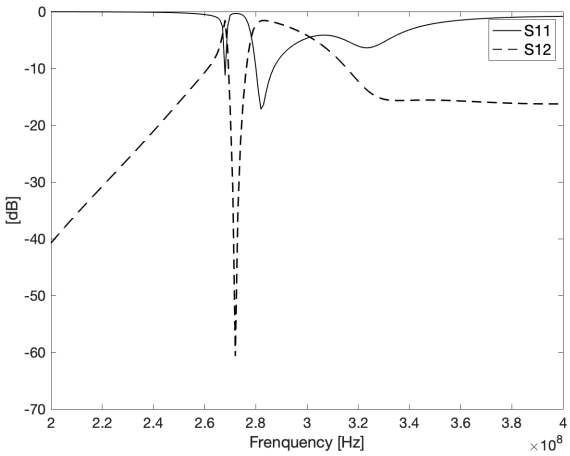


(f) $E\ [\frac{V}{m}]$ with $SD3$

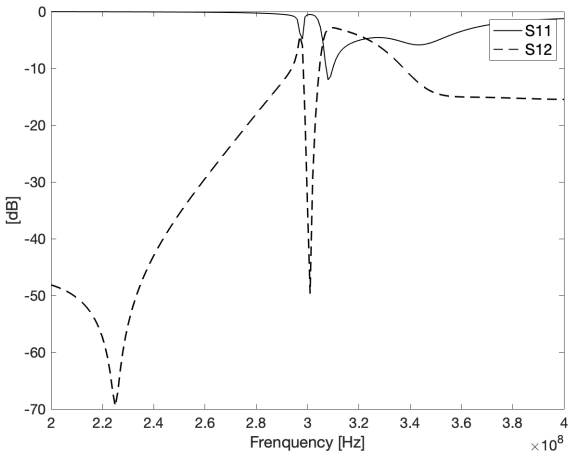
Figure 3.16: SAR efficiency and Electrical field distribution of asymmetric torus case

S-parameters analysis

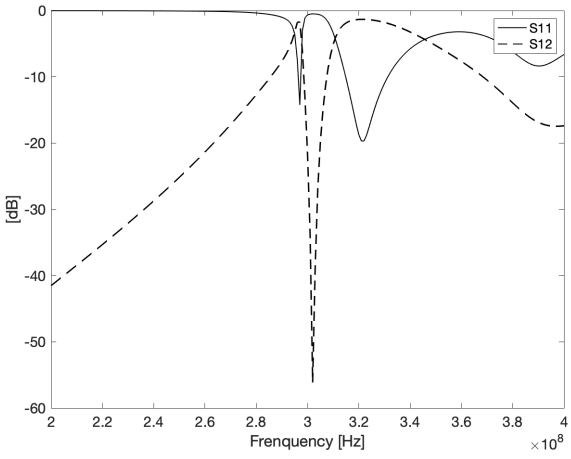
First of all, both for $SD2$ and $SD3$ S_{11} is 0 [dB]. This means both cases are not matched as explained in section 2.7. Hence only $SD1$ can be considered. This case has a low S_{11} meaning there is matching, but S_{12} is high and indicates coupling. Therefore, none of those cases is adapted.



(a) $SD1$



(b) $SD2$



(c) $SD3$

Figure 3.17: S-Parameters

Conclusion

The asymmetrical torus case shows that the combination of the asymmetric Birdcage and the weight matrix can adapt the fields in order to increase the homogeneity

in the ROI. The cost of this improvement is a decrease of the global homogeneity. Besides this, none of the cases are actually optimal as shown by the S-parameters. However, this case is only used for feasibility, so more importance will be given to matching in the following cases.

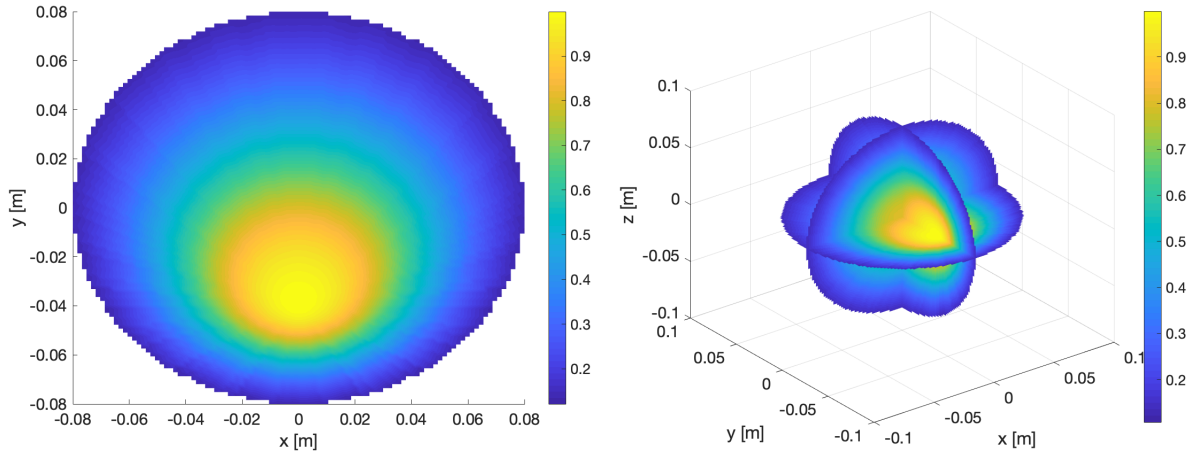
In addition to confirming the utility of this combination, the torus case reaches the first part of the first objective: increasing local homogeneity. In the following three cases, the second part of the first objective is demonstrated: the off-centered localization of the ROI. The studies of three off-centered ROI defined with Gaussian weight matrices can be conducted. The utility for the medical world of localizing fields will be then demonstrated in Chapter 4.

3.3.3 Analysis of the first Gaussian weight matrix case

The first off-centered ROI is located in the left lobe area, located at the bottom of the x-y plane.

Weight matrix

The weight matrix is created with the approach explained in section 2.3. The center of the ROI is the point p(x = 0, y = -$\frac{w}{2}$, z = 0) where w is the half-width of the brain. The attenuation factor is 1.



(a) z=0 plane (b) 3D representation

Figure 3.18: First Gaussian weight matrix

Results and analysis

The optimized values of the capacitors obtained using the MoM code with this weight matrix are given in Table 3.8. The asymmetrical configuration is clear when looking at the values, all being different independently of the SD used.

	C_1 [F]	C_2 [F]	C_3 [F]	C_4 [F]	C_5 [F]	C_6 [F]	C_7 [F]	C_8 [F]
$SD1$	1.16e-12	6.12e-12	8.64e-12	2.22e-13	1.53e-13	1.56e-13	1.41e-12	1.19e-12
$SD2$	6.60e-12	2.47e-13	3.08e-13	2.69e-12	3.88e-13	1.58e-13	6.49e-12	6.99e-14
$SD3$	7.27e-12	2.00e-13	6.54e-13	4.05e-12	1.63e-13	5.89e-14	6.45e-12	4.54e-14
	C_9 [F]	C_{10} [F]	C_{11} [F]	C_{12} [F]	C_{13} [F]	C_{14} [F]	C_{15} [F]	C_{16} [F]
$SD1$	8.13e-12	6.11e-13	2.77e-12	7.35e-13	4.58e-13	4.20e-12	1.50e-12	2.10e-12
$SD2$	1.62e-12	4.74e-12	5.43e-12	6.15e-13	5.20e-13	6.91e-12	8.09e-12	9.96e-14
$SD3$	4.12e-12	1.08e-12	1.54e-12	3.21e-12	4.04e-12	1.64e-12	2.94e-12	9.11e-13

Table 3.8: Electronic components value

Figures 3.20b, 3.20d and 3.20f show the E-field distribution with the asymmetric impact of the capacitors. Besides this asymmetric distribution, the impact of the SD choice is also visible. Different SDs yield different results. Indeed, while Figure 3.20b clearly shows a dominant impact of the excitation ports, 3.20f shows other legs have a bigger impact.

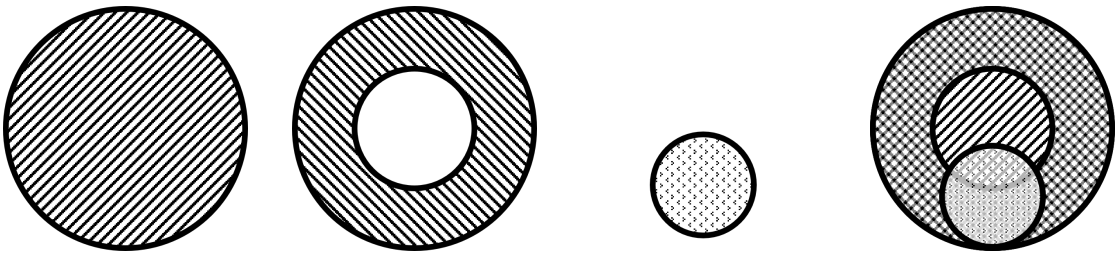
Besides the E-fields distributions, Figures 3.20a, 3.20c and 3.20e show the SAR efficiency. Each case has an order of magnitude similar to the basic one, guarantying quality images. The effect of the weight matrix is first detectable on the images with a clear tendency of the field to migrate to the ROI denoted by the weight matrix, at the bottom of the sphere. On the other hand, the upper part looks less homogeneous with black spots (indicating regions with lover field-values) appearing. A higher field indicated by an orange spot at the top of the phantom is also visible. This can be explained by higher C-values.

The second way to observe the effect of the weight matrix is the homogeneity. Table 3.9 shows the evolution of homogeneity, translated by SD, for each SD as well as the basic case to be able to compare the improvements.

	$SD0$	$SD1$	$SD2$	$SD3$
ROI	0.1436	0.1185	0.1019	0.1041
ROA	0.1745	0.2144	0.2352	0.2015
Torus	0.1502	0.2089	0.2391	0.1828

Table 3.9: Homogeneity in ROI and ROA

The analysis of the homogeneity in a torus-shaped region, indicated in Figure 3.19b, reinforces the observation that the increase in homogeneity is localized and not present in the whole torus-shaped region as in the first case. The specificity of this case and the following two is that a specific region is now targeted. Defined by the weight matrix, the analyzed region is represented in Figure 3.19c. Three distinct regions are compared to analyze the improvement in homogeneity in the ROI, which is the main objective of this thesis. The first region is the whole volume, denoted ROA and indicated in Figure 3.19a. The second one is the torus-shaped region denoted Torus and indicated in Figure 3.19b. Last but not least, the ROI is indicated in Figure 3.19c and is actually part of the Torus.



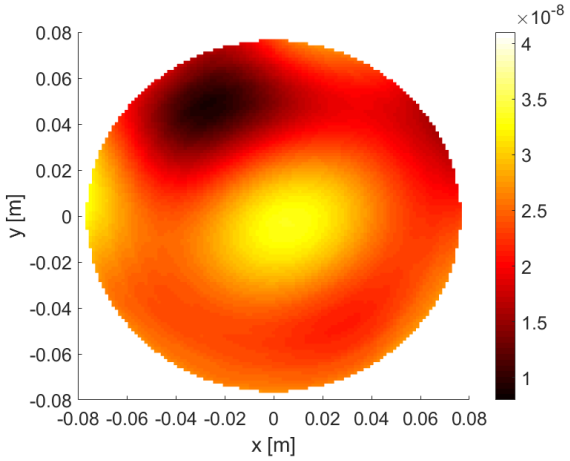
(a) ROA (b) Torus (c) ROI (d) Combination

Figure 3.19: Regions of SD

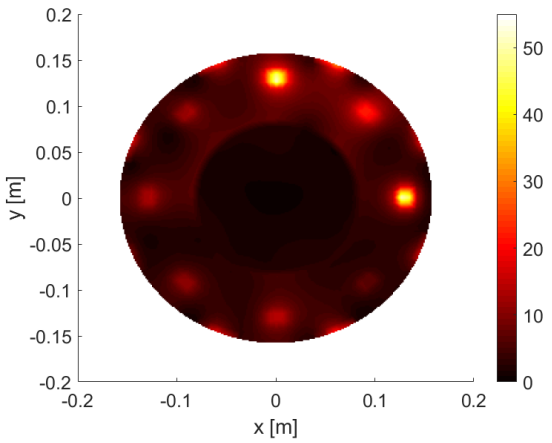
Analyzing these three regions provides us with interesting results. First, only the ROI has a decrease in the metric, meaning an increase in homogeneity as hoped. Second, the Torus, as well as ROA, has an increase in the metric meaning a worsened homogeneity. The combination of those results shows this approach leads to an improved homogeneity in the ROI specifically and not in the Torus. Indeed, the whole volume sees its homogeneity decreasing but this is also true for the Torus which contains the ROI. While this effect proves the ability to localize the improvement, it shows a negative aspect of this approach: the loss of homogeneity outside of the ROI.

Again, the use of different SDs in the optimization step gives different results with $SD2$ giving the best results. In the ROI there is a 17.47% decrease for $SD1$, a

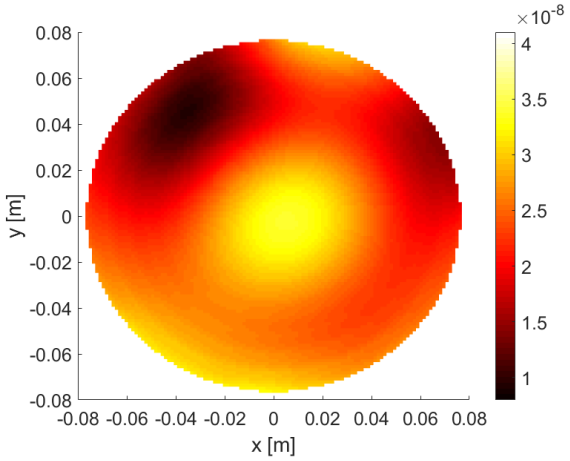
29.04% decrease for $SD2$ and a 27.53% decrease for $SD3$. On the other hand, the increase of SD in ROA is 22.90% for $SD1$, 34.78% for $SD2$ and 15.48% for $SD3$. While $SD1$ clearly is the least effective SD, the main difference between $SD3$ and $SD2$ is the decrease of homogeneity in ROA. Taking this aspect into account, $SD3$ emerges as the best-suited SD for this case. However, if only the ROI is decisive, it is $SD2$ that has the best results.



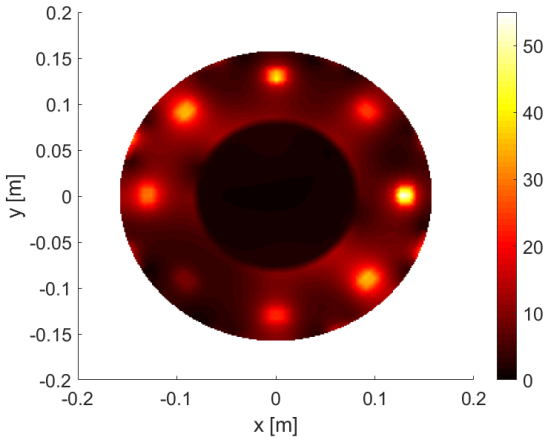
(a) $\frac{B_1}{SAR^{1/2}}\left[\frac{T}{\sqrt{W/Kg}}\right]$ with $SD1$



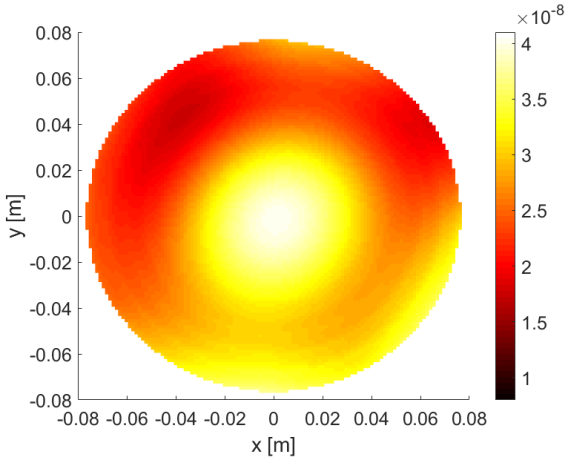
(b) $E\ [\frac{V}{m}]$ with $SD1$



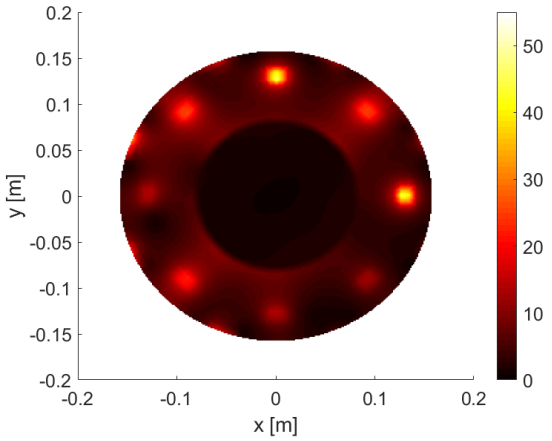
(c) $\frac{B_1}{SAR^{1/2}}\left[\frac{T}{\sqrt{W/Kg}}\right]$ with $SD2$



(d) $E\ [\frac{V}{m}]$ with $SD2$



(e) $\frac{B_1}{SAR^{1/2}}\left[\frac{T}{\sqrt{W/Kg}}\right]$ with $SD3$

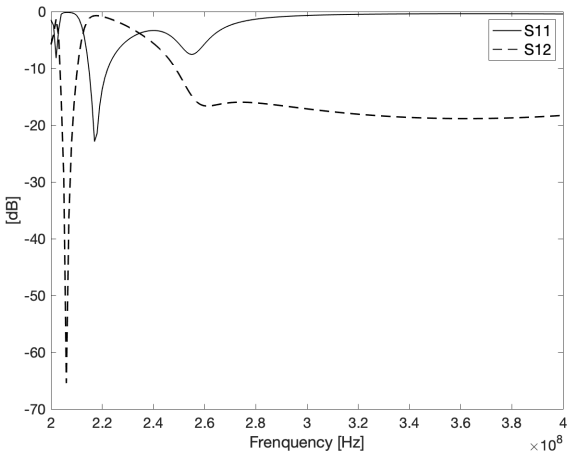


(f) $E\ [\frac{V}{m}]$ with $SD3$

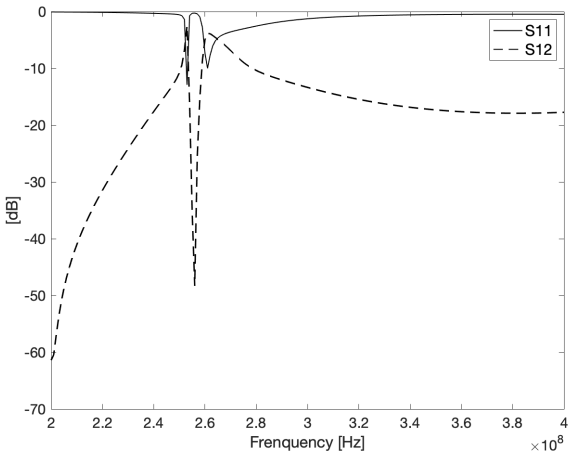
Figure 3.20: SAR efficiency and Electrical field distribution of first Gaussian case

S-parameters analysis

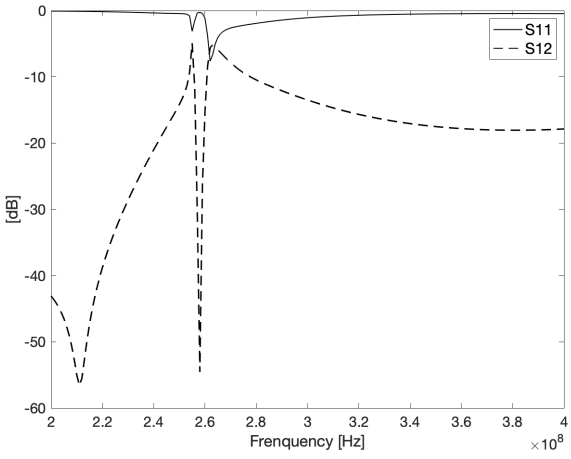
The use of this first Gaussian weight leads to a frequency shift for $SD1$ and could be tuned, however it is a bigger shift than 10 [MHz]. A matching circuit might be a solution here, as for the frequency of interest (300 [MHz]) S_{12} has a good value. For both other cases there appears to be no resonance, and are not usable as such.



(a) $SD1$



(b) $SD2$



(c) $SD3$

Figure 3.21: S-Parameters

Conclusion

The first Gaussian case shows interesting results. The homogeneity is improved in the left lobe area and the fields are of the same order of magnitude as in the

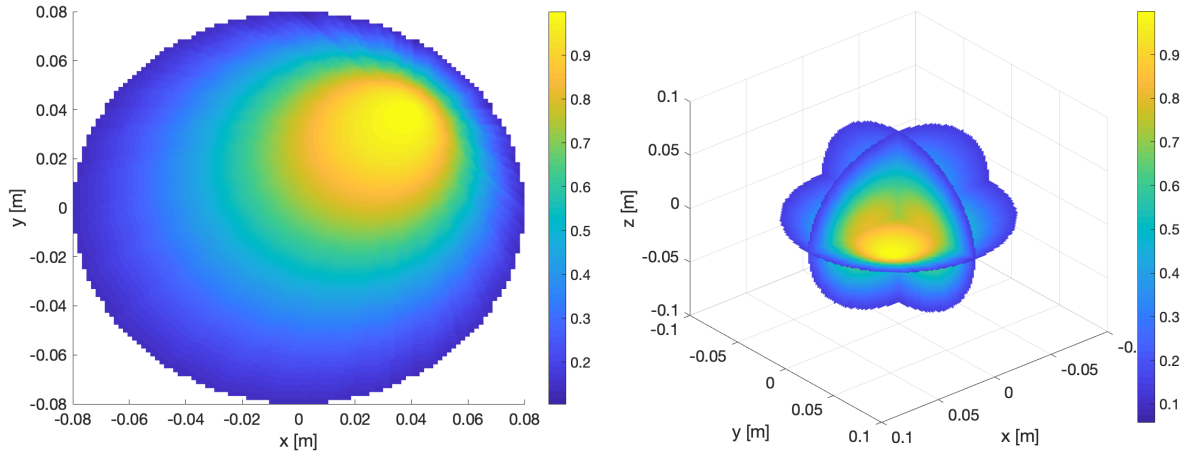
basic asymmetric case. With these results, the approach is reaching one of the aims of the thesis. However, as in the torus case, the cost of this improvement is a decrease of the global homogeneity. Again, S-parameters show the absence of resonance for two cases but only a frequency shift for the first one. Therefore, $SD1$ can be considered the best option in this case offering a 17.47% decrease in the ROI and a 22.90% increase in the ROA.

3.3.4 Analysis of the Second Gaussian weight matrix case

For the purpose of knowing if the approach is able to focus the field on any part of the brain, the second ROI is more off-centered and closer to the excitation ports. This ROI is also a first step to analyze the effect of the distance between the excitation ports and the ROI on the local standard deviation.

Weight matrix

The weight matrix is created with the approach explained in the methodology section 2.3. The center of the ROI is the point p(x = $\frac{l}{2}$, y = $\frac{w}{2}$, z = 0) where l and w are respectively the half-length and the half-width of the brain. The attenuation factor is 1.



(a) z=0 plan (b) 3D representation

Figure 3.22: Second Gaussian weight matrix

Results and analysis

The results are presented in the same way as in the previous case. Table 3.10 contains the optimized capacitor values for the three used metrics, using the MoM

code with this weight matrix.

	C_1 [F]	C_2 [F]	C_3 [F]	C_4 [F]	C_5 [F]	C_6 [F]	C_7 [F]	C_8 [F]
$SD1$	2.29e-12	7.89e-14	3.13e-13	2.80e-12	1.28e-12	4.65e-13	9.82e-13	6.24e-13
$SD2$	2.38e-13	4.74e-12	2.32e-12	3.02e-13	1.65e-12	1.83e-13	3.48e-13	5.74e-14
$SD3$	3.83e-13	8.55e-12	1.23e-12	7.39e-13	1.07e-13	1.09e-12	1.48e-13	1.08e-12
	C_9 [F]	C_{10} [F]	C_{11} [F]	C_{12} [F]	C_{13} [F]	C_{14} [F]	C_{15} [F]	C_{16} [F]
$SD1$	1.52e-12	2.99e-13	1.67e-13	5.80e-12	3.01e-12	9.12e-13	1.70e-12	1.41e-12
$SD2$	1.47e-12	1.13e-12	5.41e-12	1.71e-12	1.30e-13	6.87e-12	2.91e-12	5.31e-13
$SD3$	1.33e-12	1.32e-12	1.26e-12	2.40e-12	7.40e-13	1.08e-12	1.47e-12	1.09e-12

Table 3.10: Electronic components value

The resulting E-fields for each case are presented in Figures 3.24b, 3.24d and 3.24f. The field distribution shows the asymmetric behavior of the Birdcage, also visible in the Table. Again, the use of different SDs results in different C-values and different ways to counteract and take into account the impact of the excitation ports.

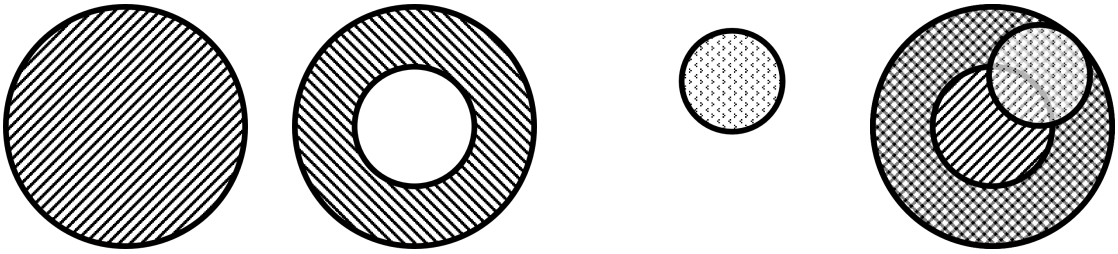
Furthermore, Figures 3.24a, 3.24c and 3.24e show the SAR-efficiency for each case where localized homogeneous regions seem to correspond with the weight matrix described above. Indeed, the homogeneous regions are located in the top right part of the phantom. In the other parts of the phantom, regions of lower (black) and higher (yellow) values are intermingled, indicating an inhomogeneity. Besides the "shape" of the fields, its values are respectable and sufficient.

The actual homogeneity of the regions mentioned above is analyzed using the SD. Table 3.11 shows the evolution of it. The values in this Table correspond to the three different regions presented in Figure 3.23.

	$SD0$	$SD1$	$SD2$	$SD3$
ROI	0.1794	0.0898	0.0548	0.0801
ROA	0.1745	0.2538	0.3007	0.3432
Torus	0.1502	0.1571	0.3066	0.3169

Table 3.11: Homogeneity in ROI and ROA

When comparing this case with the basic one, the same rhetoric can be applied as previously. If there is an increase in homogeneity in the ROI but a decrease in homogeneity in every other region, even though they contain the ROI, it can be said that the improvement of homogeneity is indeed localized. Again, in all three cases this is true confirming the fact the approach works. On the other hand, this case also suffers from a decrease of homogeneity in some regions.

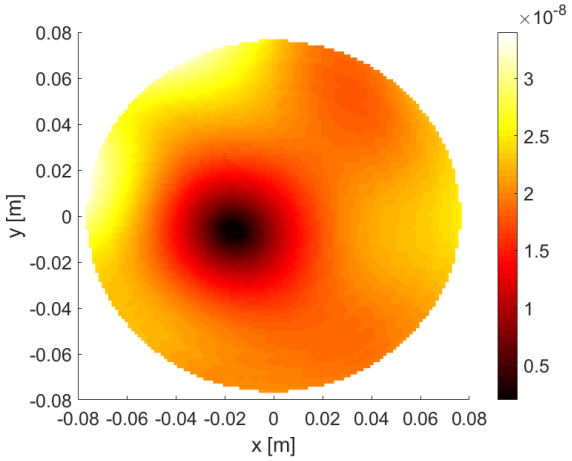


(a) ROA (b) Torus (c) ROI (d) Combination

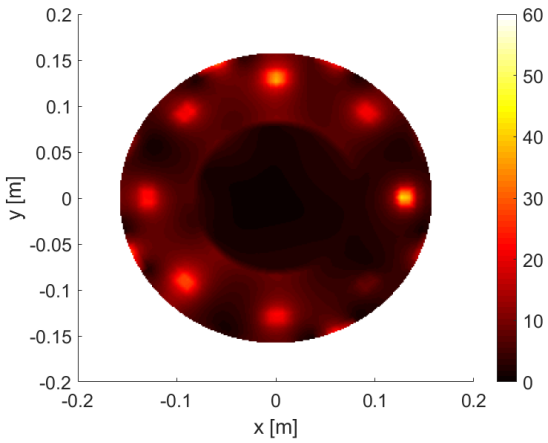
Figure 3.23: Regions of SD

The biggest improvement in the ROI is obtained by the $SD2$ with a 69.42% decrease of the metric, followed by $SD3$ with a 55.34% decrease and finally $SD1$ with a 49.94% decrease. In the ROA the biggest increase comes from $SD3$ with 96.67%, followed by $SD2$ with 72.31% and $SD1$ with 45.48%. The best compromise is therefore $SD2$.

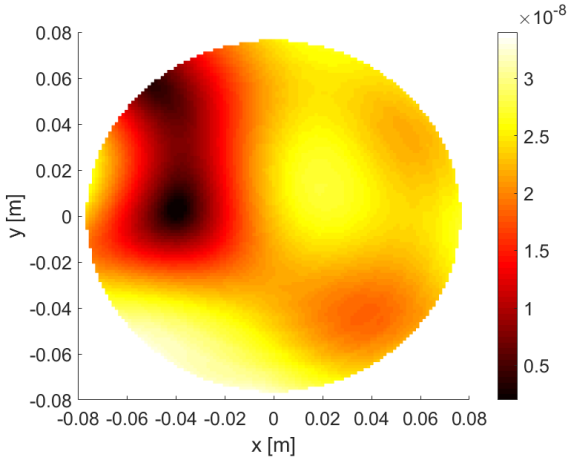
While the use of an asymmetric Birdcage counteracted the impact of the excitation ports in the first cases, it is now also used as an advantage. Indeed, the ROI is situated between and near those ports. As explained before those ports can not be removed, hence being able to define a ROI permits optimizing the use of the Birdcage and its features. The higher SAR efficiency created near the ports correspond now almost with the ROI.



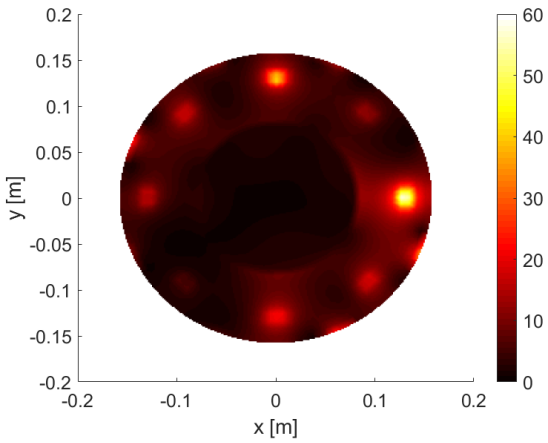
(a) $\frac{B_1}{SAR^{1/2}}\left[\frac{T}{\sqrt{W/Kg}}\right]$ with $SD1$



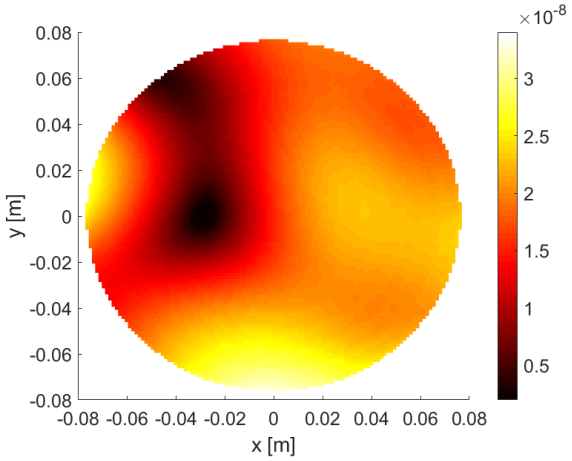
(b) $E\ [\frac{V}{m}]$ with $SD1$



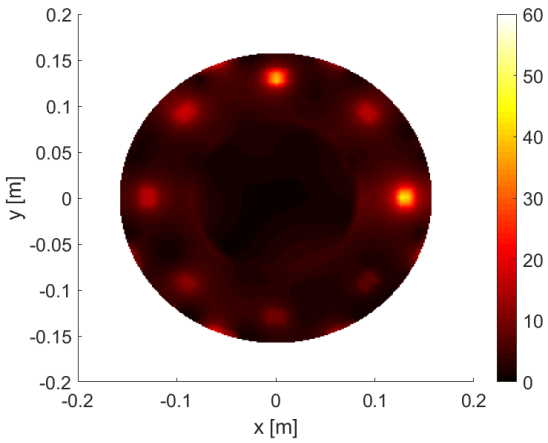
(c) $\frac{B_1}{SAR^{1/2}}\left[\frac{T}{\sqrt{W/Kg}}\right]$ with $SD2$



(d) $E\ [\frac{V}{m}]$ with $SD2$



(e) $\frac{B_1}{SAR^{1/2}}\left[\frac{T}{\sqrt{W/Kg}}\right]$ with $SD3$

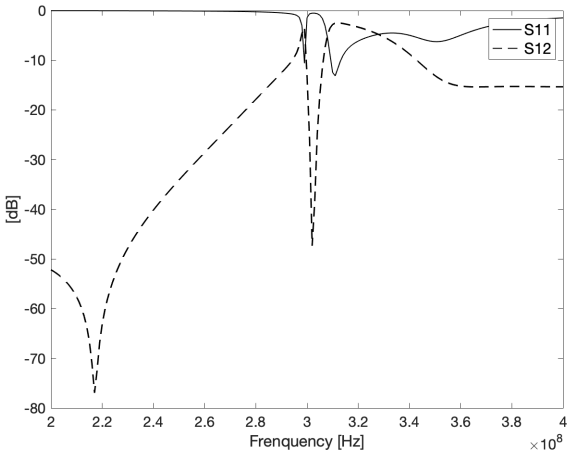


(f) $E\ [\frac{V}{m}]$ with $SD3$

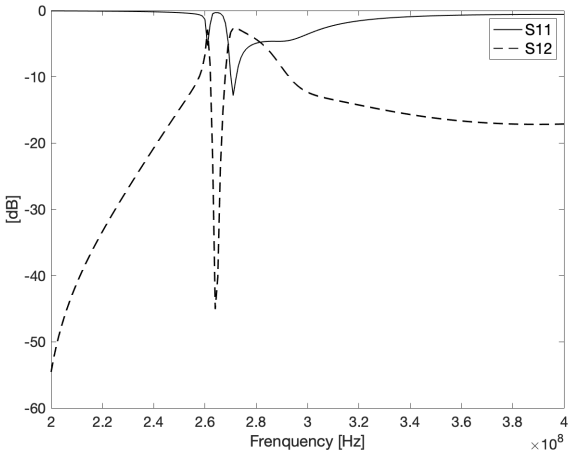
Figure 3.24: SAR efficiency and Electrical field distribution of second Gaussian case

S-parameters analysis

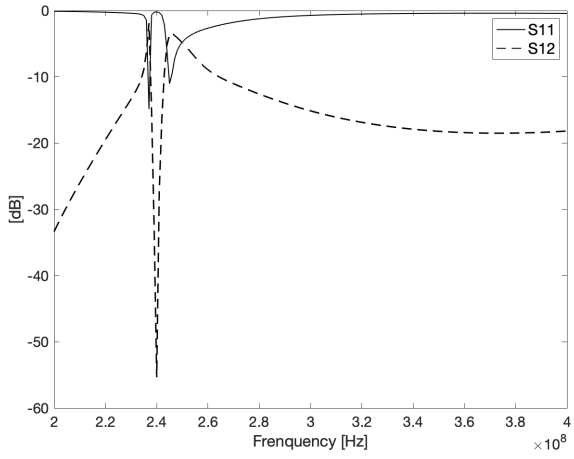
With this weight matrix, the different SDs have different results looking at their S-parameters. $SD1$ has a zero S_{11} and therefore is not matched. The same applies to $SD3$. $SD2$ on the other hand has both a low S_{11} and S_{12}. This case is adapted and shows no resonance.



(a) $SD1$



(b) $SD2$



(c) $SD3$

Figure 3.25: S-Parameters

Conclusion

The approach gives very good results in this case. In fact, the local standard deviation, when using $SD2$, decreased by 69.42% in the ROI. In the ROA it

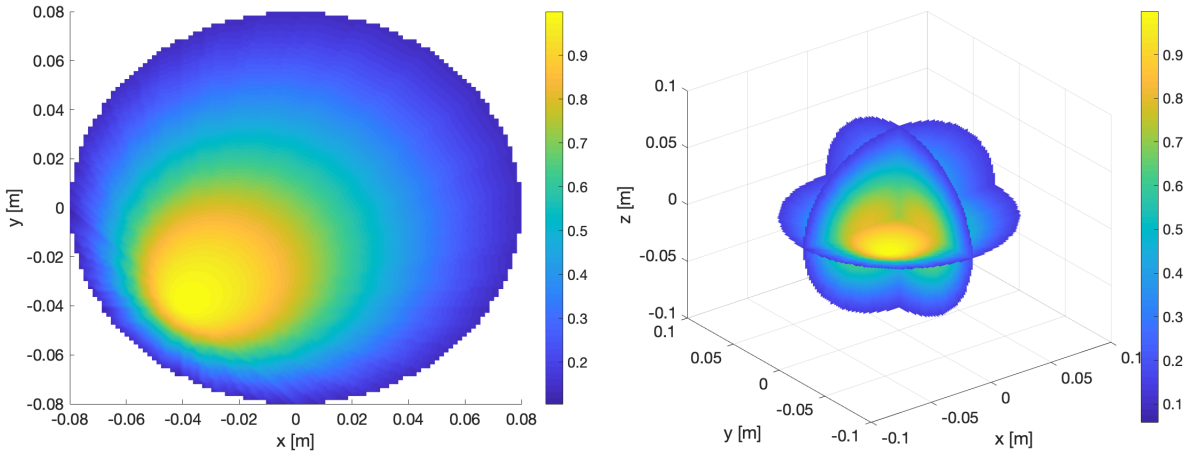
increased with 72.31%. The SAR efficiency is of the same order of magnitude as in the base case. This study shows that the SAR efficiency is more homogeneous when the ROI is closer to the excitation ports. Besides this, the S-parameters indicate $SD2$ is matched.

3.3.5 Analysis of the third Gaussian weight matrix case

The third ROI is located at the opposite of the second ROI and is therefore far from the excitation ports. This study is the second step to analyze the effect of the distance between the excitation ports and the ROI on the local standard deviation.

Weight matrix

The weight matrix is created with the approach explained in section 2.3. The center of the ROI is the point p(x = -$\frac{l}{2}$, y = -$\frac{w}{2}$, z = 0) where l and w are respectively the half-length and the half-width of the brain. The attenuation factor is 1.



(a) z=0 plan (b) 3D representation

Figure 3.26: Third Gaussian weight matrix

Results

The optimized values of the capacitors obtained using the MoM code with this weight matrix are given in Table 3.12. The asymmetrical configuration is clear when looking at the values, all being different independently of the SD used.

Figures 3.28b, 3.28d and 3.28f show the E-field distribution with the asymmetric impact of the capacitors. Beside this asymmetric distribution, the impact of the SD

	C_1 [F]	C_2 [F]	C_3 [F]	C_4 [F]	C_5 [F]	C_6 [F]	C_7 [F]	C_8 [F]
$SD1$	3.93e-13	4.35e-12	4.70e-12	1.73e-13	1.34e-13	1.21e-13	1.10e-12	3.65e-12
$SD2$	7.47e-12	5.53e-14	1.16e-13	3.03e-12	8.96e-14	3.39e-13	4.53e-12	2.47e-13
$SD3$	2.27e-12	2.32e-13	1.53e-13	2.70e-12	4.34e-13	6.29e-14	1.89e-12	1.08e-12
	C_9 [F]	C_{10} [F]	C_{11} [F]	C_{12} [F]	C_{13} [F]	C_{14} [F]	C_{15} [F]	C_{16} [F]
$SD1$	4.92e-12	4.37e-13	5.27e-12	5.58e-13	1.34e-12	2.94e-12	2.59e-13	2.49e-12
$SD2$	5.53e-12	7.49e-13	3.71e-13	1.71e-11	2.06e-12	3.63e-12	3.99e-12	3.94e-14
$SD3$	2.78e-12	3.77e-12	7.58e-13	3.36e-12	6.96e-13	6.65e-12	4.19e-12	2.38e-13

Table 3.12: Electronic components value

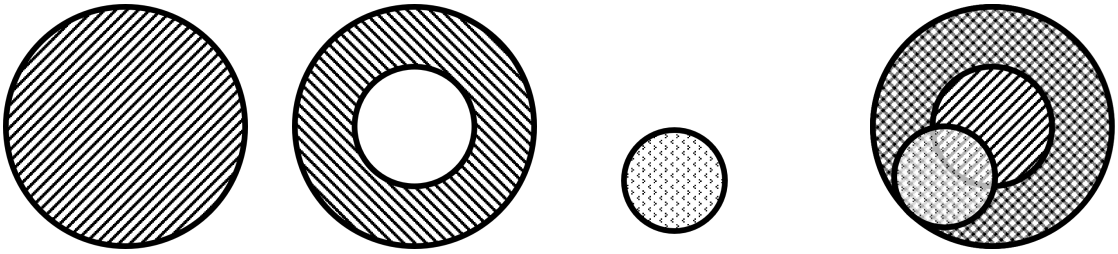
choice is also visible. Indeed, while Figure 3.28f clearly shows a dominant impact of the excitation ports, 3.28d shows other legs have a bigger impact. In fact, there is a third hotspot at the bottom left.

Furthermore, Figures 3.28a, 3.28c and 3.28e show the SAR-efficiency for each case where localized homogeneous regions seem to correspond with the weight matrix described above. Indeed, the homogeneous regions are located in the bottom-left part of the phantom. Besides the "shape" of the fields, its values are sufficient.

	$SD0$	$SD1$	$SD2$	$SD3$
ROI	0.0902	0.0862	0.0841	0.0863
ROA	0.1745	0.2010	0.1966	0.2358
Torus	0.1502	0.1889	0.1837	0.2476

Table 3.13: Homogeneity in ROI and ROA

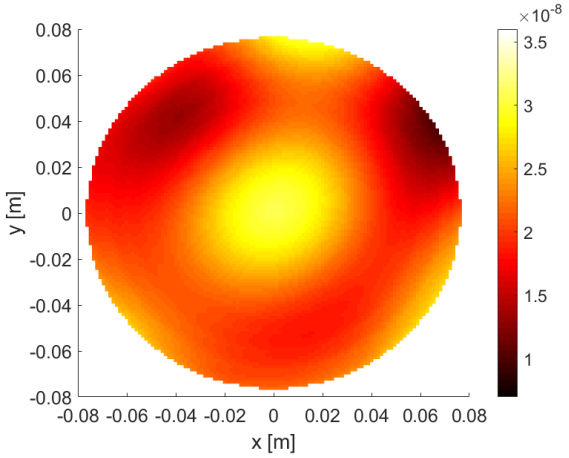
Compared to previous cases, the difference between the SDs in Table 3.13 is quite small. However, the rhetoric used before prevails as there still is an increase of homogeneity in the ROI and a decrease in all the other regions. Adding to this the acceptable field values, in ROI but also ROA, supports the statement that the approach of this thesis is adaptable to a wide range of cases. The impact of the excitation ports has less importance in this case as the ROI is located on the opposite of those ports.



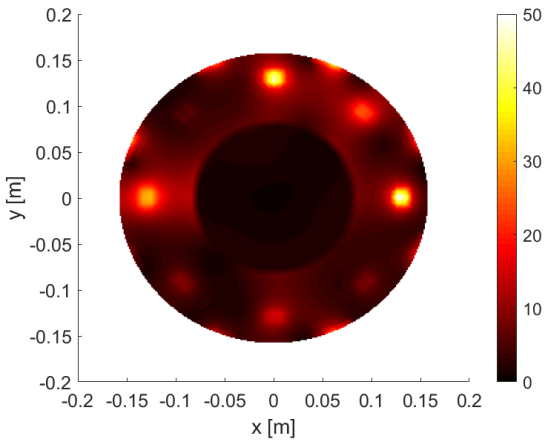
(a) ROA (b) Torus (c) ROI (d) Recap

Figure 3.27: Regions of SD

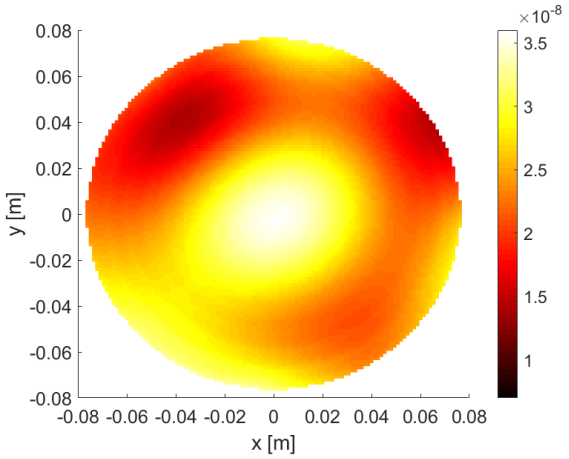
The three regions used in Table 3.13 are presented in Figure 3.27. The biggest improvement in the ROI is obtained by the $SD2$ with a 6.75% decrease of the metric, followed by $SD1$ with a 4.41% decrease and finally $SD3$ with a 4.26% decrease. In the ROA the biggest increase comes from $SD3$ with 35.15%, followed by $SD1$ with 15.22% and $SD2$ with 12.67%. The best compromise is therefore $SD2$.



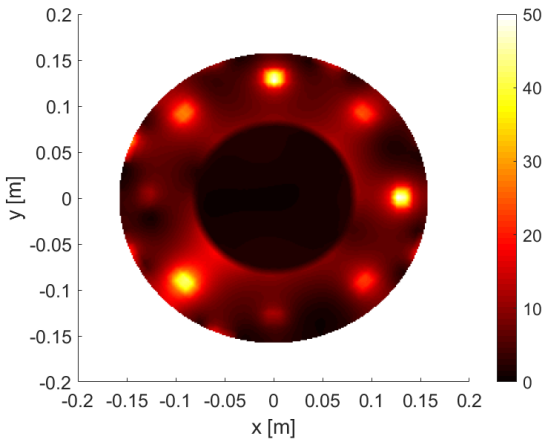
(a) $\frac{B_1}{SAR^{1/2}}\left[\frac{T}{\sqrt{W/Kg}}\right]$ with $SD1$



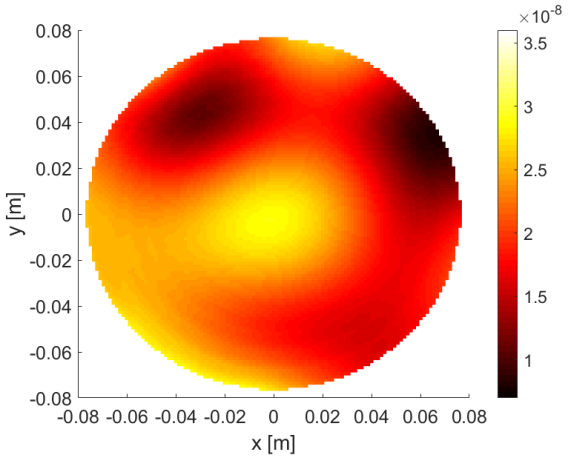
(b) $E\ [\frac{V}{m}]$ with $SD1$



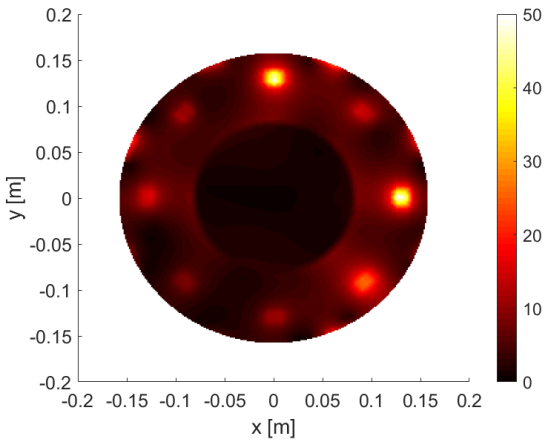
(c) $\frac{B_1}{SAR^{1/2}}\left[\frac{T}{\sqrt{W/Kg}}\right]$ with $SD2$



(d) $E\ [\frac{V}{m}]$ with $SD2$



(e) $\frac{B_1}{SAR^{1/2}}\left[\frac{T}{\sqrt{W/Kg}}\right]$ with $SD3$

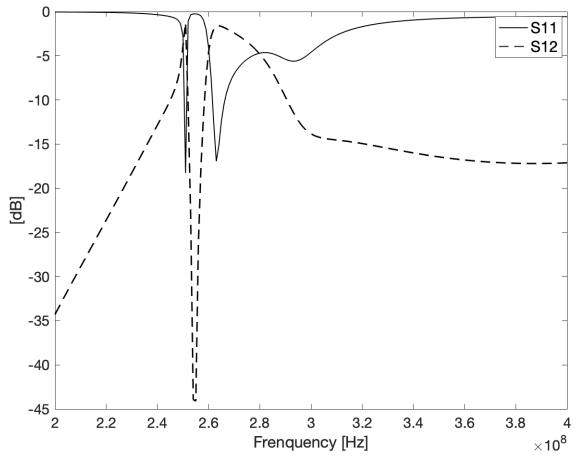


(f) $E\ [\frac{V}{m}]$ with $SD3$

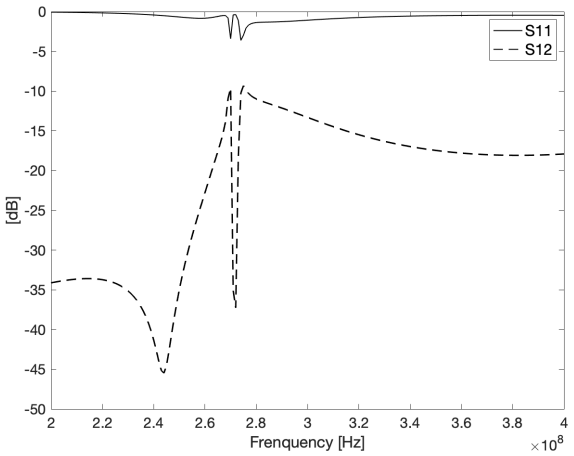
Figure 3.28: SAR efficiency and Electrical field distribution of third Gaussian case

S-parameters analysis

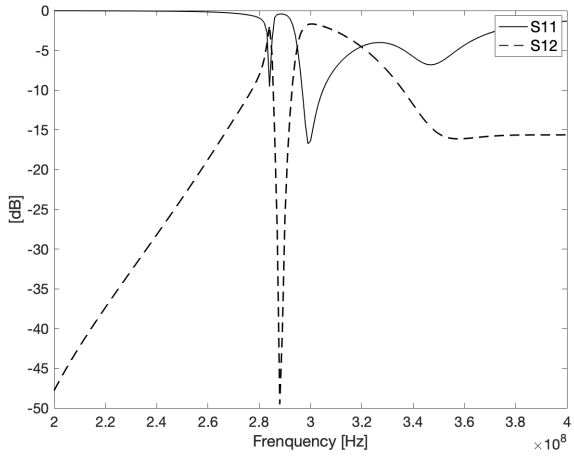
Looking at the S-parameters, $SD1$ shows a tendency to be optimized for the frequency of interest. The local minimum of S_{11} is less marked than in previous examples of adapted cases. Nevertheless, resonance is present and no coupling interferes with it. $SD3$ on the other hand has coupling and $SD2$ has no resonance.



(a) $SD1$



(b) $SD2$



(c) $SD3$

Figure 3.29: S-Parameters

Conclusion

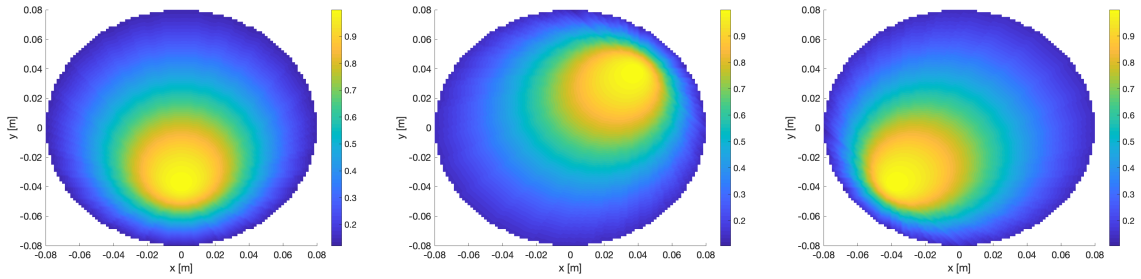
Although the approach improves the local homogeneity in this case, the decrease of the local standard deviation is smaller than in the second Gaussian case. This study

confirms that the SAR efficiency are more homogeneous when the ROI is closer to the excitation port. The importance of posterior checks using the S-parameters is once again demonstrated. Taking those into account, $SD1$ becomes the best option for this case.

3.3.6 Conclusion - Comparison between cases

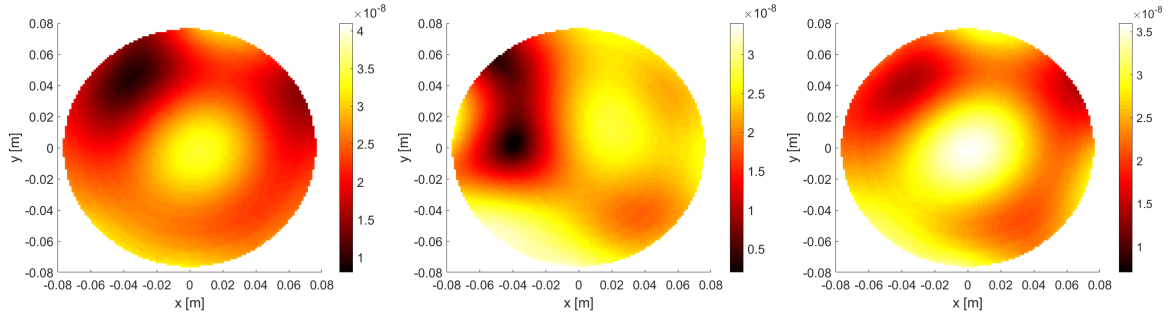
The torus study shows that the fields can be focused on external zones with the asymmetric Birdcage. However, this case does not represent a major interest from a medical point of view.

The three Gaussian studies prove that the asymmetric Birdcage can increase the local homogeneity on a specific off-centered ROI. As presented in Figure 3.31, the fields are focused on the desired area. Moreover, The ROI is defined by the weight matrix and so can be chosen by doctors.



(a) First Gaussian (b) Second Gaussian (c) Third Gaussian

Figure 3.30: Weight Matrix



(a) First Gaussian (b) Second Gaussian (c) Third Gaussian

Figure 3.31: SAR efficiency $\frac{B_1}{SAR^{1/2}}\left[\frac{T}{\sqrt{W/Kg}}\right]$

The study of the second Gaussian optimized using $SD2$ gives the most successful results with an increase of 69.42% in the ROI while keeping the same order of magnitude of the magnetic flux compared to the basic asymmetrical case. In addition to this, the S-parameters show that the case is adapted. Therefore, the first objective of the thesis is reached. In fact, the approach proves that the MRI of temporal lobes can be improved by adding a weight matrix in the MoM code. Moreover, the results are improved when the ROI and the excitation ports are close to each other. Let us not forget however that a couple of cases were not adapted due to the lack of resonance or presence of coupling. After analyzing the different SDs for different cases, as well as their S-parameters, an optimal case is achievable for each ROI using the thesis approach.

Chapter 4

Functional Imaging

4.1 Introduction

The proper functioning and the benefits of the approach have been demonstrated in Chapter 3. Although the first goal of this master thesis is already reached, this fourth chapter goes deeper by tackling a more complex medical application of MRI introduced in section 1.5.4; Functional Imaging. The approach is originally not designed for such a complex case but the results of this chapter show the already existing improvements as well as the direction in which it can be improved to suit the medical field. Instead of the homogeneity of the fields analyzed in previous chapter, the actual desired shape of the fields is now the focus. This shifts the thesis objective in this second part. To do so, a newly used metric is introduced in section 4.3. The objective function is now only described by $SD2$, not taking the homogeneity anymore in account.

As this application is more practical, only the most convincing results are presented. Those resulting in bad S-parameters or having other issues are not presented.

4.2 Low and high inflow regions

The primary source of energy of the brain is glucose. Besides the inflow of oxygen mentioned in section 1.5.4, a higher blood flow means also the transport of more glucose. This glucose is consumed in different brain regions, affecting the BOLD (Blood Oxygen Level Dependent) sensitivity. The glucose consumption is referred to as cerebral blood flow (CBF). Concerning CBF, two regions can be discerned. The first one has more inflow than consumption of glucose. This region will be named Region 1 in the rest of this chapter and contains the amygdala, basal ganglia, thalamus and cingulate cortex, all shown in Figure 4.1. Those are recruited for

fast responses [42].



(a) Amygdala (b) Basal ganglia (c) Thalamus (d) Cingulate cortex

Figure 4.1: Region 1

The second region, called Region 2 in this chapter, has a lower incoming flow than consumption. This region contains the lateral frontal and lateral parietal lobes, shown in Figure 4.2.[42]



(a) Frontal lobe (b) Parietal lobe

Figure 4.2: Region 2

While the first region can be approximated by a central circle, the second region is approximated by two ellipses as shown in Figure 4.3. Those two regions are the cases considered in this chapter. But before diving deeper into those cases, the use of ellipse-shaped weight matrices is introduced.

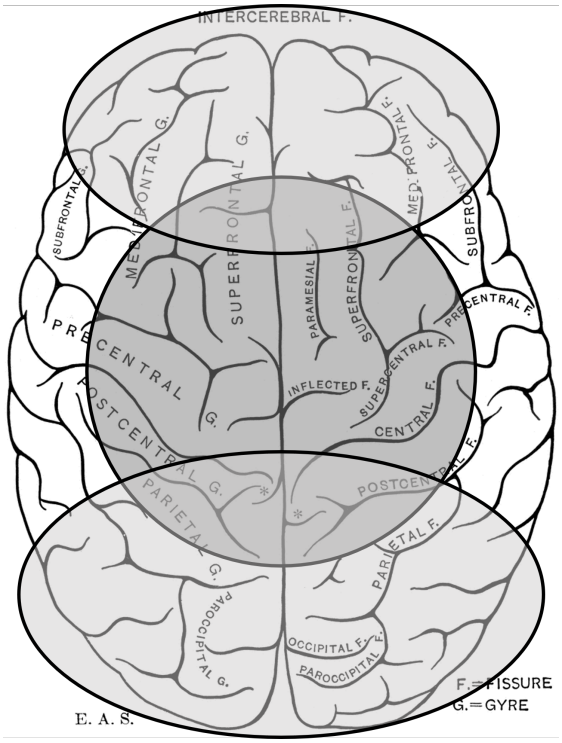


Figure 4.3: Approximated Region 1 and 2

4.3 Shape of the field

Besides the novelty of using ellipse-shaped regions, a new metric is used to analyze the resulting fields. It takes the difference between the obtained field F and the desired field F_d and is denoted $DIFF$ in this thesis. Let us note that the obtained field is normalized to match the desired field, described by the already normalized weight matrix.

$$DIFF = \frac{\sum_{i=1}^{N} |F'_i - F'_{d,i}|}{N} \tag{4.1}$$

$$F'_i = \frac{F_i - min(F)}{max(F) - min(F)} \tag{4.2}$$

$$F'_{d,i} = \frac{F_{d,i} - min(F_d)}{max(F_d) - min(F_d)} \tag{4.3}$$

As this chapter again uses the asymmetrical conventional Birdcage the basic case remains the same, namely the one presented in section 3.3.1. The shape of the field being now of interest, $SD2$ comes in as the best suited SD.

4.4 Analysis of ellipse-shaped weight matrix

This first analyzed region is an upper ellipse. This case shows the feasibility of the new adapted approach before tackling the more complex case of the functional imaging. This ellipse is a fine first case because it is close to the excitation ports. Therefore, the fields should be easier to adapt.

Weight matrix

The ellipse-shaped weight matrix presented in Figure 4.4, is created with the approach presented in section 2.3. The ROI is an ellipse centered in p(x=0,y=$\frac{l}{2}$,z=0) where l is the half-length of the brain. The semi-major axis and the semi-minor axis are respectively set to 0.04 [m] and 0.02 [m].
Inside the ellipse, the weights are set to 1. Outside the ROI, the weights are defined by the Gaussian based on the distance between the edge of the ROI and the edge of the Brain. The attenuation factor is 1. The ellipse-shaped weight matrix actually combines homogeneity and shape of the field as the ellipse region is homogeneous compared to the rest of the desired field.

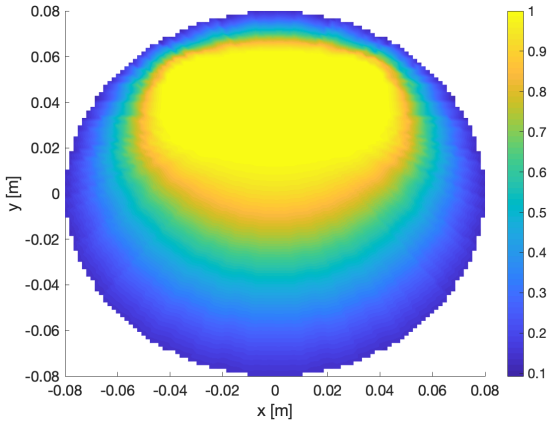


Figure 4.4: ellipse-shaped weight matrix

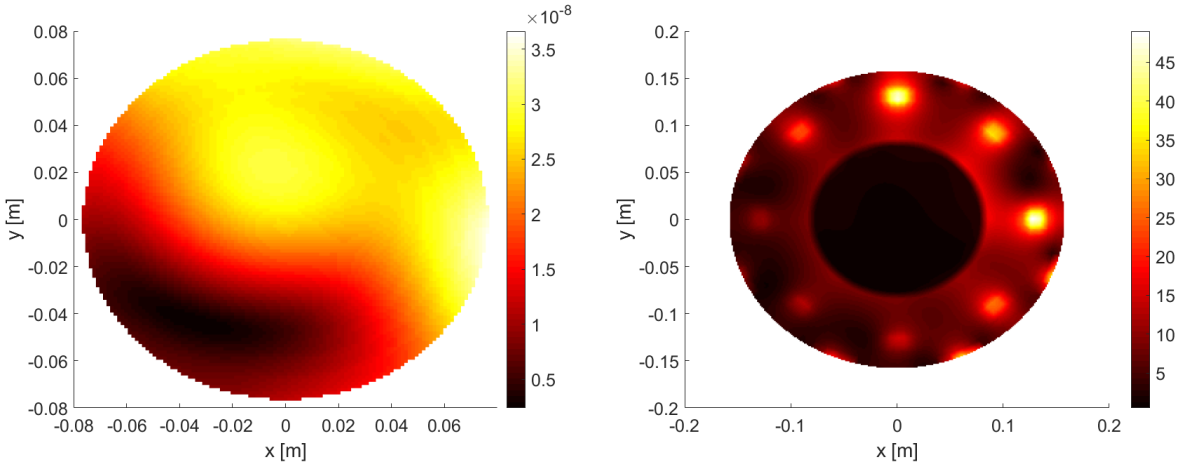
Results

The optimized values of the capacitors obtained using the MoM code with this weight matrix and $SD2$ are given in Table 4.1. The asymmetrical configuration is still present and is clear when looking at the values, all being different.

	C_1 [F]	C_2 [F]	C_3 [F]	C_4 [F]	C_5 [F]	C_6 [F]	C_7 [F]	C_8 [F]
$SD2$	2.80e-12	2.54e-12	8.26e-14	4.72e-12	3.97e-14	3.11e-12	4.89e-14	1.17e-11
	C_9 [F]	C_{10} [F]	C_{11} [F]	C_{12} [F]	C_{13} [F]	C_{14} [F]	C_{15} [F]	C_{16} [F]
$SD2$	1.25e-13	3.07e-13	2.08e-12	6.25e-12	1.42e-13	8.32e-12	2.67e-13	4.15e-12

Table 4.1: Electronic components value

Figure 4.5b shows the E-field distribution with the asymmetric impact of the capacitors. The impact of the excitation ports is visible, as it was the case in Chapter 3.



(a) $\frac{B_1}{SAR^{1/2}}$ $\left[\frac{T}{\sqrt{W/Kg}}\right]$ (b) E $[\frac{V}{m}]$

Figure 4.5: Field distribution of Ellipse-shaped region

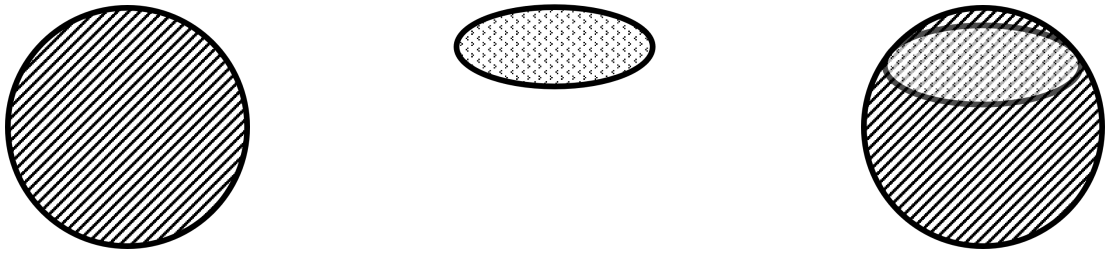
Furthermore, Figure 4.5a shows the SAR efficiency corresponding with the weight matrix described above. Indeed, the ellipse-shaped region is clearly located in the top part of the phantom. There is a non-negligible influence of the excitation ports, but it doesn't cause too much damage as the ROI is located close by. Besides the shape of the fields, its values are sufficient.

Table 4.2 gives the values of the metrics used to analyze the results. First of all, $DIFF$ in the ROA describes the difference, over the whole phantom, between both fields. In a perfect case this would be zero. This $DIFF$ will be used throughout this chapter as it describes how well the desired field was obtained. As, in this

	$SD0$	$SD2$
$DIFF$ ROA	0.3105	0.2309
SD ROI	0.1472	0.0418

Table 4.2: Fields fitting and homogeneity

specific case, a big part of the region is described by a homogeneous ellipse an additional metric is used. The specific region of the ellipse is analyzed using the SD from previous chapter. This will not be the case in the rest of the chapter as the main goal is now the shape of the field and not its homogeneity.



(a) ROA (b) ROI (c) Combination

Figure 4.6: Regions of SD and $DIFF$

The two regions used in Table 4.2 are presented in Figure 4.6. First of all, the ROA shows an improvement in $DIFF$ with a decrease of 25.63%. This translates perfectly the fact the desired field approaches the expected field. In the ROI an improvement of a 71.60% decrease of the SD is obtained. In addition to adapting the capacitors to fit the general field, it is noticeable that areas of high homogeneity are also well approached by this thesis approach. Besides this, if a region defined as homogeneous by the weight matrix improves its homogeneity it can be considered in the same way an improvement of $DIFF$ in this particular region.

S-parameters analysis

The posterior check using the S-parameters shows no sign of coupling. However, the values obtained for the capacitors are optimal for a frequency of 277 [MHz]. In conclusion, this result is optimal for a different frequency, but it is acceptable in this case and could be tuned.

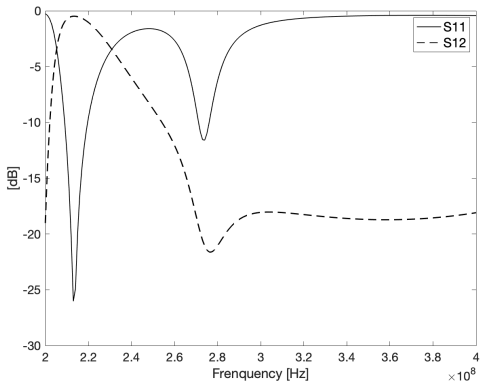


Figure 4.7: S-parameters Ellipse

4.5 Analysis of Region 1

The first zone has a quite simple approximation. The centralized Gaussian describes a field, over the whole phantom, almost similar to the field obtained in the basic asymmetric case. Therefore, it can be considered as an advantage but also a disadvantage. Indeed, there is a high probability to match the field well, but since the basic Birdcage optimized the homogeneity of the fields on all the phantom, it gets complicated to improve it.

Weight matrix

The weight matrix is created with the approach explained in the methodology (section 2.3). The center of the ROI is the point p(0,0,0). The attenuation factor is 1.

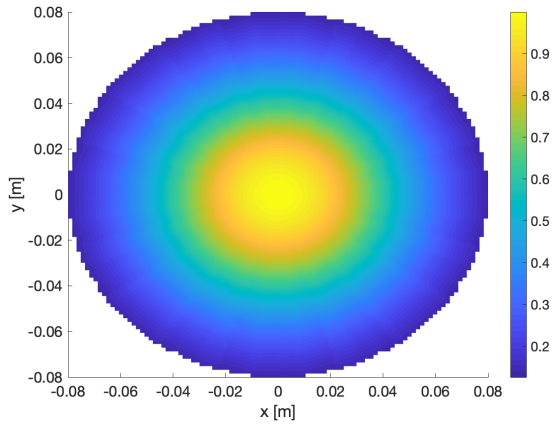


Figure 4.8: Centered Gaussian weight matrix

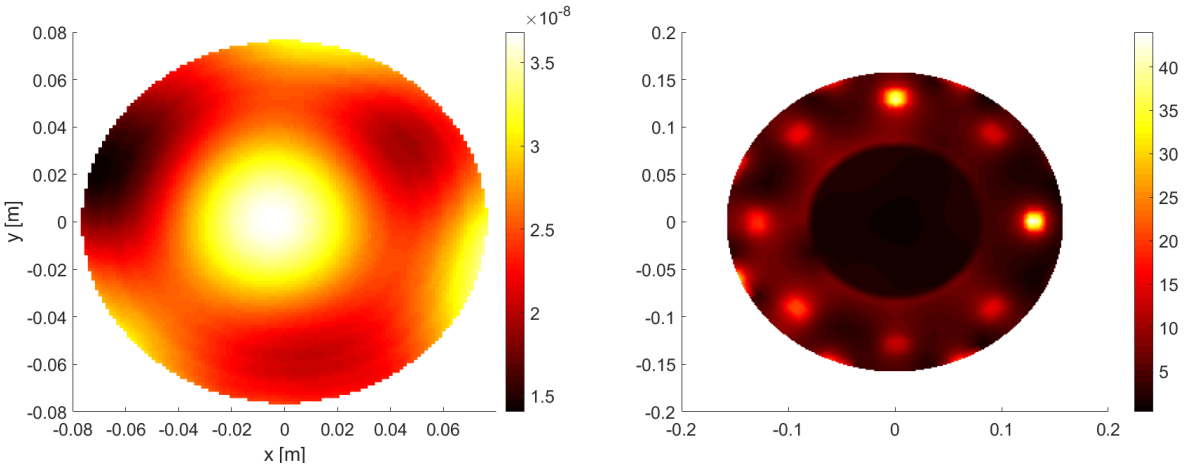
Results

The results are presented in the same way as previous case. Table 4.3 contains the optimized capacitor values for $SD2$, using the MoM code with this weight matrix. The asymmetrical configuration is still present and is clear when looking at the values, all being different independently of the case.

	C_1 [F]	C_2 [F]	C_3 [F]	C_4 [F]	C_5 [F]	C_6 [F]	C_7 [F]	C_8 [F]
$SD2$	1.78e-12	3.45e-12	5.53e-13	2.30e-12	3.46e-13	5.94e-13	3.91e-12	4.07e-12
	C_9 [F]	C_{10} [F]	C_{11} [F]	C_{12} [F]	C_{13} [F]	C_{14} [F]	C_{15} [F]	C_{16} [F]
$SD2$	3.61e-13	4.16e-12	6.45e-12	3.44e-12	5.49e-12	2.02e-12	1.44e-12	2.94e-12

Table 4.3: Electronic components value

Figure 4.9b shows the E-field distribution with the asymmetric impact of the capacitors. This impact however is almost not visible looking at the field distribution. As for the basic case, the advantage of the asymmetry is to counteract the impact of the excitation ports.



(a) $\frac{B_1}{SAR^{1/2}}$ $\left[\frac{T}{\sqrt{W/Kg}}\right]$ (b) E $[\frac{V}{m}]$

Figure 4.9: Field distributions of Region 1

This way symmetric desired fields can be obtained. Figure 4.9a shows the SAR-efficiency corresponding with the weight matrix described above. Region 1 is indeed symmetrical and an almost symmetrical field is obtained. Besides the shape of the fields, its values are sufficient. Table 4.4 gives the values of the metrics used to

	$SD0$	$SD2$
$DIFF$ ROA	0.2398	0.2272

Table 4.4: $DIFF$ in ROA

analyze the results. As this fourth chapter focuses on the adaptability of the desired field, only the ROA is analyzed. First of all, the ROA shows an improvement in $DIFF$ with a decrease of 5.24%. This is a small improvement compared to previous case and shows the disadvantage of such a case. Applying it to a field fairly similar to the desired field will only result in a small improvement.

S-parameters analysis

A similar conclusion as previous case is reached regarding the S-parameters. The posterior check using the S-parameters shows again no sign of coupling. The values obtained for the capacitors are optimal for a frequency of 280 [MHz]. In conclusion, this result is optimal for a different frequency, but it is acceptable.

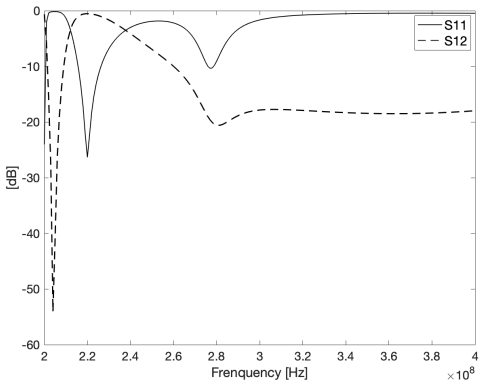


Figure 4.10: S-parameters Region 1

4.6 Analysis of Region 2

Region 2 is approximated by two ellipse-shaped regions. The feasibility of fitting a field to an ellipse-shaped desired field has been discussed at the start of this chapter. However, an additional challenge is present in this case. Indeed, two separate regions are present. This adds complexity and reaches the limit of this thesis approach.

Weight matrix

The weight matrix is the sum of two ellipse-shaped weight matrices presented in section 4.4. The first ROI is centered in p(x=0,y=$\frac{l}{2}$,z=0) where l is the half-length of the brain. The semi-major axis and the semi-minor axis are respectively set to 0.04 [m] and 0.02 [m].

The second ROI is centered in p(x = 0,y=$\frac{-l}{2}$,z=0) where l is the half-length of the brain. The semi-major axis and the semi-minor axis are respectively set to 0.06 [m] and 0.02 [m]. Both of the attenuation factors are set to 1.

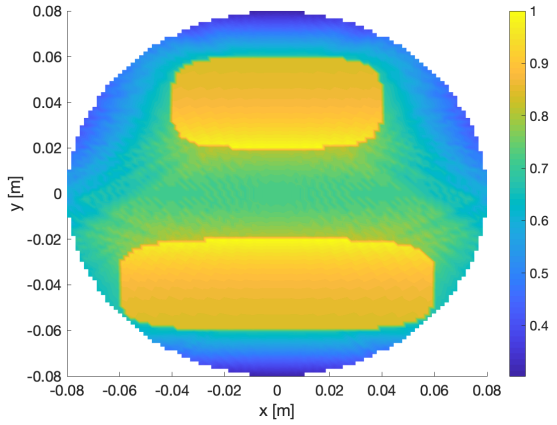


Figure 4.11: Functional weight matrix

Results

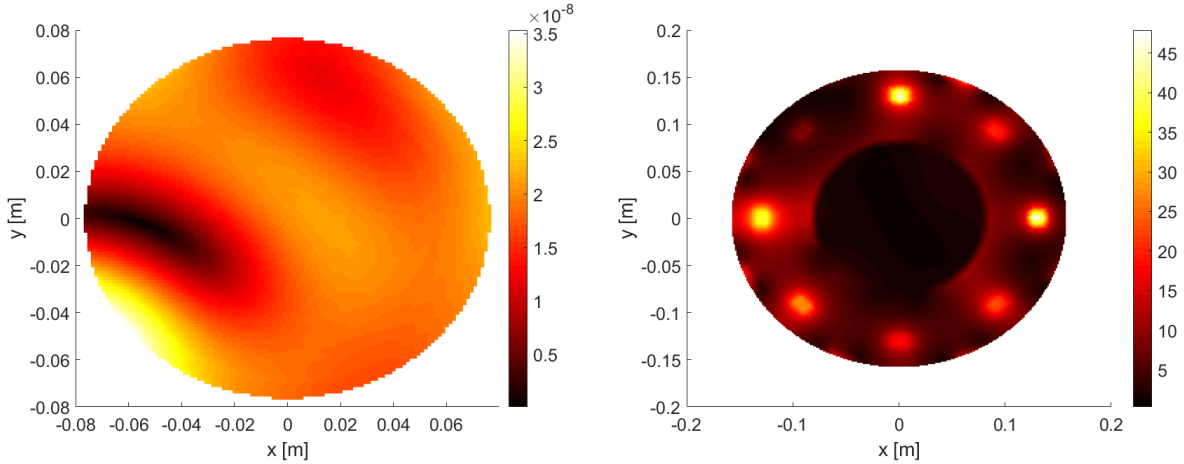
The optimized values of the capacitors obtained using the MoM code with this weight matrix are given in Table 4.5. The asymmetrical configuration is clear when looking at the values, all being different. Those results were obtained using $SD2$.

	C_1 [F]	C_2 [F]	C_3 [F]	C_4 [F]	C_5 [F]	C_6 [F]	C_7 [F]	C_8 [F]
$SD2$	3.62e-13	1.91e-12	1.61e-11	8.02e-14	8.36e-13	1.29e-12	7.87e-14	8.04e-13
	C_9 [F]	C_{10} [F]	C_{11} [F]	C_{12} [F]	C_{13} [F]	C_{14} [F]	C_{15} [F]	C_{16} [F]
$SD2$	1.85e-14	1.67e-12	9.75e-13	1.57e-12	8.80e-12	1.14e-12	2.49e-12	3.91e-12

Table 4.5: Electronic components value

While $SD2$ did deliver interesting results concerning the $DIFF$, coupling is still present as will be shown later. This hints that adding an extra ellipse adds too

much complexity. Both field distributions are presented in Figure 4.12. The impact of the excitation ports, as well as the asymmetry is visible in the E-field.



(a) $\frac{B_1}{SAR^{1/2}}\left[\frac{T}{\sqrt{W/Kg}}\right]$ (b) $E\ [\frac{V}{m}]$

Figure 4.12: Field distributions of Region 2

Concerning the SAR efficiency, a slight resemblance with the desired field is noticeable. An ellipsoid region is present at the top, but slightly offset to the right. This is probably due to the excitation ports. The second ellipse at the bottom has an even bigger offset, to the left this time. All in all it can be said the use of $SD2$ and the weight matrix had an impact. Nonetheless, it is not as successful as in Chapter 3. The added complexity of the additional ellipse prohibits getting better results.

	$SD0$	$SD2$
$DIFF$ ROA	0.3797	0.2992

Table 4.6: $DIFF$ in ROA

Besides the offset of the field, its values are acceptable and still yield an improvement. Table 4.6 shows $DIFF$ over the ROA for this case. A 21.19% decrease means that the obtained field fits the desired field better than in the basic case.

S-parameters analysis

The S-parameters are presented in Figure 4.13. Coupling is present for the frequency of interest. Therefore the case is not feasible as such. To be used as a medical application, the Birdcage has to be adapted to be matched and avoid coupling.

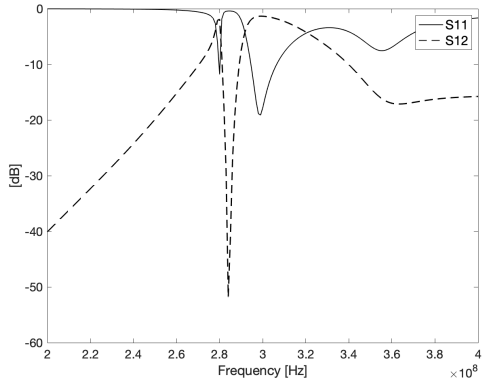


Figure 4.13: S-parameters Region 2

4.7 Conclusion

This chapter shows that the approach can already improve the results of a complex medical application. In fact, section 4.4 proves that the approach permits to choose the shape of the field while this shape stays simple.
However, this chapter also shows the limitations of the approach. Section 4.5 shows that the approach cannot significantly improve the basic case of the centered Gaussian field. Moreover, section 4.6 indicates that the approach cannot focus the fields on two distinct zones at the same time.
These limitations were expected as the approach was developed to focus on precise off-centered zones such as the lobes. When the ROI becomes bigger it looks more efficient to optimize the global homogeneity.

Chapter 5

Connected Birdcage

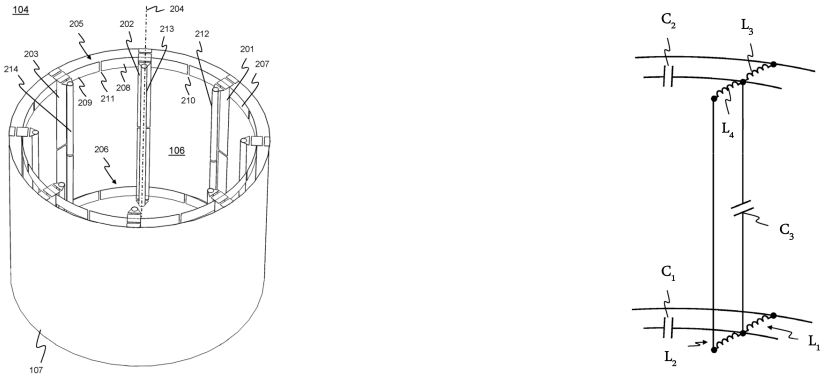
5.1 Introduction

To finish this thesis and go a step further, the adaptability of the approach to a different Birdcage model is introduced. In fact, adapting the morphology of the Birdcage could improve the results of the Chapter 4. The goal being to investigate if the use of a weight matrix works with another Birdcage morphology, only the symmetrical use of the Birdcage is analyzed. The same torus-shaped weight matrix will be used and, contrary to Chapter 4, the metric used is the SD and not the $DIFF$ anymore.

5.2 Connected Birdcage

The Connected Birdcage (CBC) used in this chapter can be described as a conventional Birdcage with an additional segment or "layer". It was invented in 2021 by Craeye, Park and Tihon [9]. The summary of the invention is as follows: *"There is a need for an improved radiofrequency transducer assembly based on an antenna structure of the Birdcage type that allows obtaining a radiofrequency magnetic field that is relatively homogeneous, which may improve magnetic resonance imaging."*[9]

While it is still made out of 8 identical sectors, each leg is doubled as shown in Figure 5.1. This gives the possibility to add a capacitor to each sector, as well as inductors. These 4 inductors are more precisely located, at the top and bottom, between each leg and between the shield and the legs, as shown in Figure 5.1b.



(a) Complete structure (b) Individual element

Figure 5.1: Structure of CBC [9]

5.3 Analysis of the weight matrix on a Connected Birdcage

Similar to what was done at the start of Chapter 2, the basic case is presented and will be used to compare the resulting fields when using the weight matrix. The weight matrix used will be the same torus used for the asymmetric case in Chapter 3.

5.3.1 Basic symmetric case

The resulting SAR efficiency and electric field are represented in Figure 5.2 while its C-values and inductors are presented in Table 5.1. The C-values are identical for each leg of the CBC.

C_1 [F]	C_2 [F]	C_3 [F]	L_1 [H]	L_2 [H]	L_3 [H]	L_4 [H]
7.00e-13	7.00e-13	2.83e-14	7.91e-11	3.72e-8	7.91e-11	3.72e-8

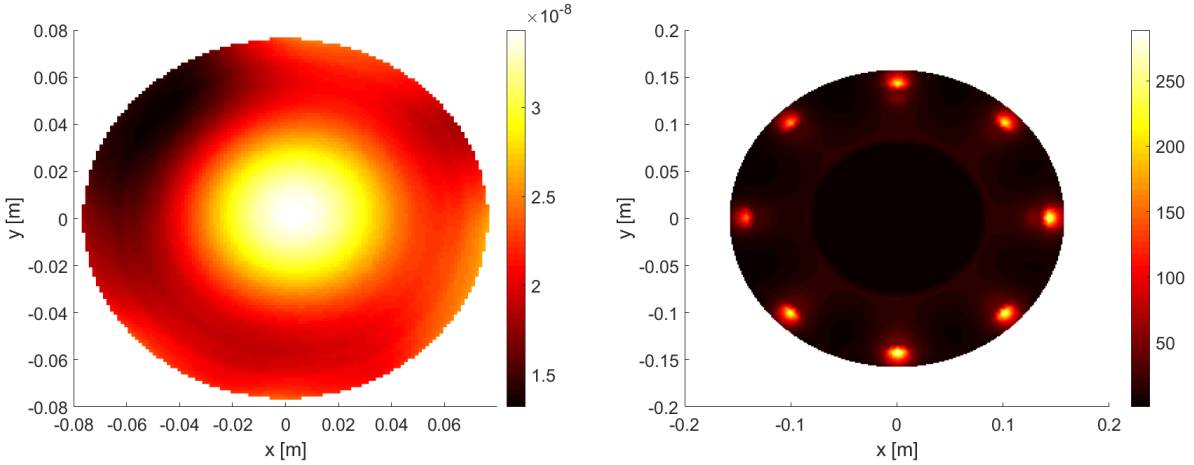
Table 5.1: Electric components value

As expected, the E-field is symmetrical. The SAR efficiency is centered and almost homogeneous on the sides. A comparison of the homogeneity with the conventional Birdcage, over the whole volume ROA, is given below.

ROA_{CBC}	ROA_{sym}	ROA_{asym}
0.2088	0.2298	0.1745

Table 5.2: Comparison in homogeneity

Table 5.2 shows an increased homogeneity in comparison with the basic symmetrical case. ROA_{CBC}, ROA_{sym} and ROA_{asym} stand respectively for the basic (symmetric) CBC, the basic symmetric Conventional Birdcage and the basic asymmetric Conventional Birdcage. As mentioned before, a good basic case leaves less room for improvement. However, the asymmetrical conventional Birdcage from Chapter 3 remains better judging on the global homogeneity only.



(a) $\frac{B_1}{SAR^{1/2}}\left[\frac{T}{\sqrt{W/Kg}}\right]$ (b) $E\ [\frac{V}{m}]$

Figure 5.2: SAR efficiency and Electric field distribution of the basic case

This basic case is used as reference when analyzing results obtained by this thesis approach. Both the visual aspect as numerical aspect help understand the improvements brought by the approach.

S-parameters analysis

Being the basic case without any influence from weight matrices, no coupling is expected for the frequency of interest. Figure 5.3 shows the S-parameters of the basic case, confirming the absence of coupling and optimization for the frequency of interest.

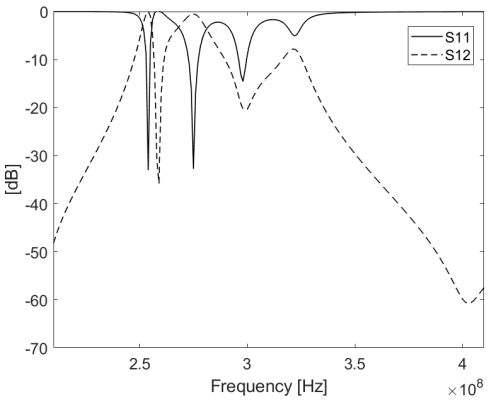


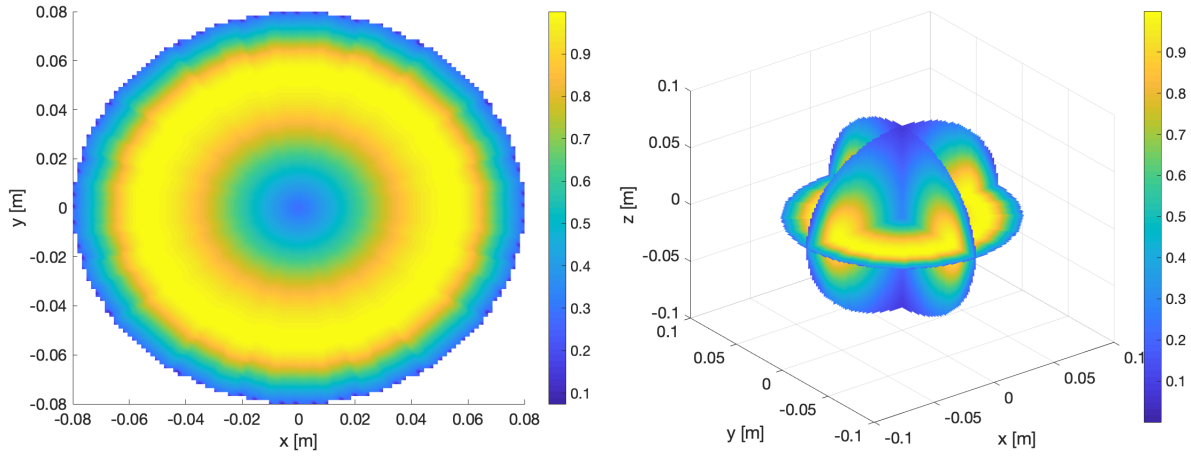
Figure 5.3: S-parameters basic case

5.3.2 Analysis of the Torus-shaped weight matrix case

The Torus shape is symmetrical and highlights the lobes. Its study can prove that the fields can be focused on the lobes while still using the symmetrical Birdcage. In Chapter 3, encouraging results were obtained concerning the evolution of the homogeneity in the torus region using $SD1$. However, in the asymmetrical case coupling was present as indicated by the S-parameters. It was then concluded that it is possible to improve local homogeneity but coupling remains an issue.

Weight matrix

The weight matrix is the torus weight matrix presented in section 3.2.2 and in Figure 5.4. The specific values are a=1.25 and D_e is set to 25 millimeters.



(a) z=0 plan (b) 3D representation

Figure 5.4: Torus weight matrix with a=0.65

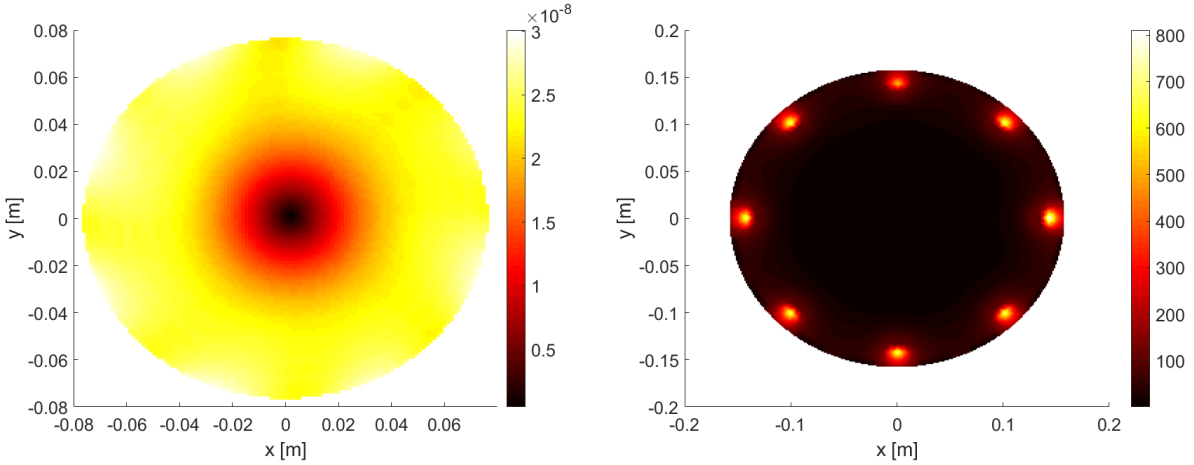
Results and analysis

For this case, the optimized values of the capacitors and inductors obtained using the MoM code using $SD1$ are presented in Table 5.3. The symmetrical configuration of the bird cage yields identical values for each leg, with C_1 and C_2 being identical.

	C_1 [F]	C_2 [F]	C_3 [F]	L_1 [H]	L_2 [H]	L_3 [H]	L_4 [H]
$SD1$	3.76e-14	3.76e-14	2.32e-12	6.74e-12	6.91e-12	6.74e-12	6.91e-12

Table 5.3: Electric components values

The distribution of the E-field resulting from those capacitors values is represented in Figure 5.5b. A logical symmetric distribution is visible, confirming each leg is indeed equivalent.



(a) $\frac{B_1}{SAR^{1/2}}\left[\frac{T}{\sqrt{W/Kg}}\right]$ (b) $E\ [\frac{V}{m}]$

Figure 5.5: SAR efficiency and Electric field distribution of the Torus case

Beside the E-field, the SAR efficiency is presented in Figure 5.5a. At first glance, the homogeneous region on the torus is encouraging. However, the centralized minimum suggests the presence of a coupling effect as in Chapter 3. This will be analyzed below using the S-parameter. Besides this, this field can be analyzed in three ways. First, the values are of the same order as the basic case. This is essential in order to obtain images. Secondly, its shape. The torus shape region is present (visible in yellow), hence following the weight matrix. Lastly, its homogeneity. This is the most important part of the analysis and is done using the SD in different regions. The SD in the ROI and ROA are presented in Table 5.4 (ROA_{CBC} and ROI_{ROI}). In addition to those values, the obtained results for $SD1$ with the same weight matrix in the conventional Birdcage are also repeated (ROI_{sym} and ROI_{asym}). In this way, a short comparison between both Birdcages is made.

	$SD0$	$SD1$
ROA_{CBC}	0.2088	0.2392
ROI_{CBC}	0.1347	0.0863
ROI_{sym}	0.1803	0.1600
ROI_{asym}	0.1502	0.1452

Table 5.4: Homogeneity in ROI and ROA

All cases show an increase in homogeneity translated by a decrease of the SD. The CBC yields the best results. Even more interesting is the already very homogeneous

ROI when using the CBC. Without applying any weight matrix better results are obtained compared to using $SD1$ with the Conventional Birdcage. Still, using $SD1$ on the CBC improves the homogeneity drastically with a decrease of 35.90%. This decrease of SD in the ROI is coupled with an increase in the ROA of 14.55%. Using the previously used rhetoric from Chapter 3 this shows a localized increase in homogeneity. Let us not forget however the presence of coupling.

S-parameters analysis

The S-parameters are presented in Figure 5.6. An identical situation to that of the asymmetric case in Chapter 3 appears. A low S_{11} indicates the antenna is not matched.

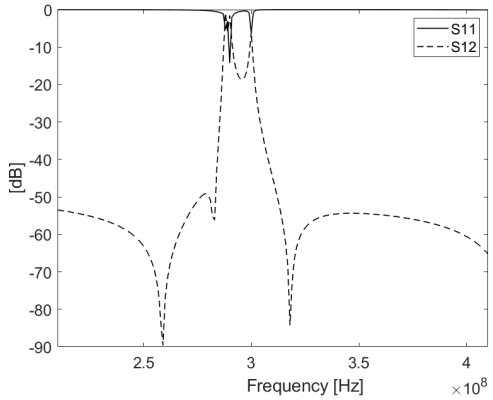


Figure 5.6: S-parameters Torus

5.3.3 Conclusion

The main objective of this chapter was to investigate the adaptability of the thesis approach on a different Birdcage. While the homogeneity significantly improved in the ROI, it still is not an optimal result. Indeed, as for the torus cases of the Chapter 3, the Birdcage is not matched and cannot be used as such. On another note the results can be seen as encouraging. While the cases in Chapter 3 had no practical utility, it did not prevent successful results when applying the same approach in a different case. Such as for the conventional Birdcage, this study shows that the fields can be adapted using the approach on the CBC. These results are very encouraging for the study of the approach on improved Birdcage morphologies.

Chapter 6

Conclusions and perspectives

To the day, few literature provide numerical and experimental data on the non-central location of the area of interest and its increase in homogeneity. The medical world has stated its interest, and therefore the aim of this thesis was to provide more insights into the possibilities offered by the Birdcage.

The approach, presented in Chapter 2, consisted of understanding and adapting the Birdcage design using GMSH. The understanding of the MoM code and its main principles (Method of Moments, Equivalent principles, Optimization step and Open circuit pattern) helped to clarify the possibilities of improvement. In order to define the ROI and the desired field, Gaussian distributed weight matrices were presented. Therefore, the MoM code was adapted to incorporate and take them into account. Finally, the modified objective functions as well as metrics were defined.

Chapter 3 shows the feasibility to localize a homogeneous ROI using weight matrices. While the symmetric Birdcage shows improvement, the real breakthrough is obtained with the asymmetric configuration. The torus-shaped weight matrix brings into light the importance of the resonance and the non-negligible impact of the coupling effect which outweighs its good results in terms of homogeneity. The three Gaussian studies prove that the asymmetric Birdcage can increase the local homogeneity on a specific off-centered ROI and therefore reaching the first objective of this thesis. In addition, the Gaussian weight matrices delivered results without coupling effect. This introduces the first improvement perspective which is the reduction of the coupling effect in the other cases. Finally, the use of the advantage of the excitation ports proved to be successful.

Furthermore, Chapter 4 tackled a more complex and concrete medical application of the approach. The interest not only in the homogeneity but also the shape of the

fields led to the introduction of a new metric in this chapter. Even when adding a complexity with an additional ROI, the approach delivered encouraging results. This reached the second goal of the thesis.

With constantly evolving technology, the Birdcage is deemed to go through several evolutionary changes in the years to come. The adaptability of the approach to different Birdcage models therefore appeared as an important topic. Chapter 5 analyzed this adaptability to the Connected Birdcage in the symmetric state. Once more encouraging results were obtained leading to future perspectives.

Finally, as mentioned through the manuscript, different perspectives of this thesis exist. (i) Adapting other Birdcages, as was introduced with the CBC, by implementing the asymmetric version could lead to a comparison and search for the best suited Birdcage. (ii) Moving from a 2D optimization to 3D, which will probably require more time and resources. (iii) Investigate the tuning of capacitors to combine several cases on a same Birdcage.

Appendices

Appendix A

Simplified electrical representation of a Birdcage

This Appendix is a summary and a rephrasing of Nikulin's way to define the capacitance of low-pass (LP) and high-pass (HP) Birdcage coils [34]. The idea is to take the loop present in a Birdcage, shown in Figure A.1, and to apply Kirchhoff's laws. This allows the fundamental mode ($k = 1$) to be tuned to the operating frequency. The voltage law gives:

$$U_n^r - U_n^l + U_{n+1}^l = 0 \tag{A.1}$$

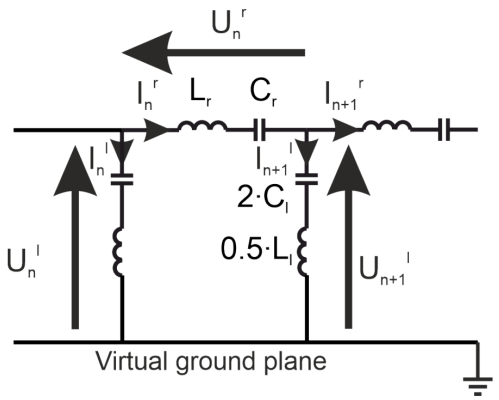


Figure A.1: Calculation of the Birdcage coil [34]

With n the rung number while U_n^r and U_n^l are the rung and leg voltage drops:

$$U_n^r = i\omega \cdot \left(L_s^r I_n^r + \sum_{m=1}^{N-1} I_{n+m}^r M_{n,m}^r \right) + \frac{I_n^r}{i\omega C_r}, \tag{A.2}$$

$$U_n^l = \frac{i\omega}{2} \cdot \left(L_s^l I_n^l + \sum_{m=1}^{N-1} I_{n+m}^l M_{n,m}^l \right) + \frac{I_n^l}{2i\omega C_r} \tag{A.3}$$

It must be noted that $U_N^{r,l} = U_0^{r,l}$ as the first and last rung are connected [34]. Besides the voltage law, the current law gives:

$$I_n^l = I_{n+1}^r - I_n^r \tag{A.4}$$

Again, the connected end and start rung lead to $I_N^{r,l} = I_0^{r,l}$. At the resonant frequency the current distribution is given as follows (A.4):

$$I_n^r = I_0 e^{\frac{2i\pi kn}{N}} \tag{A.5}$$

where I_0 is the maximum current intensity, k is the mode number and N is the total number of unit cell. The combination of Eq. A.4 and A.5 results in:

$$I_n^r = I_0 e^{\frac{2i\pi kn}{N}} \left(e^{\frac{2i\pi k}{N}} - 1 \right) \tag{A.6}$$

Equation A.2 and A.3 can be simplified using effective inductances L^r and L^l:

$$U_n^r = i\omega I_n^r L^r + \frac{I_n^r}{i\omega C_r}, \tag{A.7}$$

$$U_n^l = \frac{1}{2} i\omega I_n^l L^l + \frac{I_n^l}{i_l} \tag{A.8}$$

The effective inductances are defined as:

$$L_m^{r,l} = \hat{L}_m^{r,l} + \sum_{n=0, n\neq m}^{N-1} M_{nm}^{r,l} e^{2i\pi k \frac{n-m}{N}} \tag{A.9}$$

with $\hat{L}_m^{r,l}$ the self-impedance of ring or leg m. Equation A.9 takes into account the mutual coupling $M_{nm}^{r,l}$. Having a symmetrical Birdcage results in having identical legs and rungs and therefore $M_{nm}^{r,l} = M_{n-m}^{r,l}$. Therefore, the previous expression becomes:

$$L_m^{r,l} = \hat{L}_m^{r,l} + \sum_{n=0, n\neq m}^{N-1} M_{nm}^{r,l} cos\left(2\pi k \frac{n-m}{N} \right) \tag{A.10}$$

Combining equations A.4, A.2 and A.3, it comes.

$$\left(L_r\omega - \frac{1}{C_r\omega}\right) \cdot I_n^r = \frac{1}{2}\left(L_l\omega - \frac{1}{C_l\omega}\right) \cdot \left(I_{n-1}^r + I_{n+1}^r - 2I_n^r\right) \tag{A.11}$$

The last step is to replace the current by equation A.5. This results in a relation between the capacitances, the order k of the mode and the frequency:

$$\frac{L_r\omega - \frac{1}{C_r\omega}}{L_l\omega - \frac{1}{C_l\omega}} = -2sin^2\left(\frac{\pi k}{N}\right) \tag{A.12}$$

This expression is valid for a band-pass (BP) configuration containing both capacitors C_r and C_l. Besides BP, low-pass (LP) and high-pass (HP) configurations also exist as described in section 1.6.4.
Equation A.12 can be rewritten for both the LP and HP, and describes the capacitance to obtain the $k = 1$ mode at the angular frequency ω. For the HP Birdcage, C_{HP} is given by:

$$C_{HP} = \frac{1}{\omega^2\left(L_r + 2sin^2\left(\frac{\pi}{N}\right)L_l\right)} \tag{A.13}$$

While the capacitance C_{LP} for a LP becomes:

$$C_{LP} = \frac{2sin^2\left(\frac{\pi}{N}\right)}{\omega^2\left(L_r + 2sin^2\left(\frac{\pi}{N}\right)L_l\right)} \tag{A.14}$$

Nikulin then goes on and considers 3 types of Birdcages to prove the proposed theory and compare it to the conventional approach [34]. Those 3 types of both LP and HP Birdcages are composed of 4, 8 and 16 rungs. Their sizes, such as, radii (130 [mm] and 155 [mm] for the shield), length (240 [mm]), and widths (10 [mm] rungs and legs), are chosen to be the same. As it was designed for head imaging at 7T, the frequency is of approximately 300 MHz. The inductances for 4, 8 and 16 rungs Birdcages are presented in Table A.1.

Inductance type (nH)	4 rungs	8 rungs	16 rungs
Legs (L_l)	132.60	146.59	173.97
Rings (L_r)	149	86.05	42.09

Table A.1: Effective inductances of 3 different Birdcages at 300MHz [34]

The values of capacitances to tune the $k = 1$ mode are shown in Table A.2.

Capacitance type (nH)	4 rungs	8 rungs	16 rungs
C_{HP} or (C_r)	1	2.18	5.09
C_{LP} or (C_l)	1	0.64	0.39

Table A.2: Ring and leg capacitances of the 3 different types of Birdcages [34]

Nikulin then concludes that *"LP Birdcage calculation process leads to not feasible values of capacitance in order to tune the k = 1 mode at the frequency of 300 MHz. Indeed these values are below the self-parasitic capacitance [31]. Hence, at such a high frequency, the HP topology is preferable."*

Appendix B

Transmission line-based approach

Another approach by Nikulin is the use of transmission line [34]. Figure B.1 shows the Birdcage as a transmission line (TL) with unit cells. Each unti cell represented ($i-1$, i, $i+1$) has a leg admittance Y and an end-ring segment impedance Z. Again using the symmetry of the Birdcage, a simplified, but equivalent, circuit with three elements can be used for the analysis. Not that their values are adapted to $2Y_i$ and $Z_i/2$ to correspond.

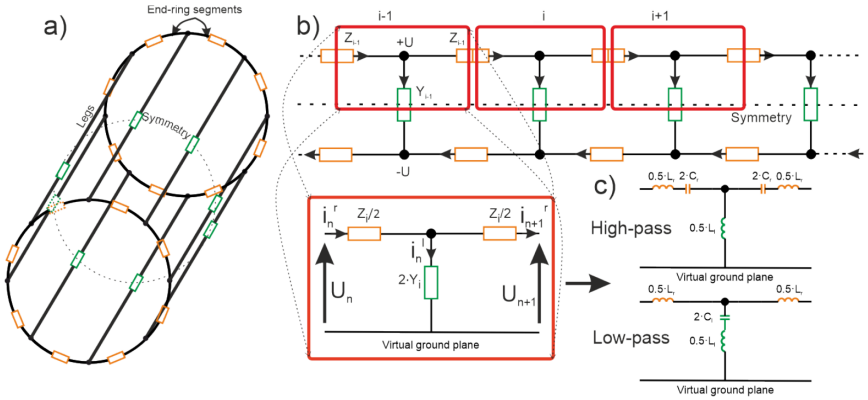


Figure B.1: (a) General view of a Birdcage coil composed of eight rungs. (b) Simplified equivalent circuit of a Birdcage coil segment. (c) The HP or LP unit cells in terms of inductances and capacitances.[34]

Next, the Transfer matrix T_i is used to find the Bloch impedance and the phase shift of a unit cell [6], [31]. Such a 2 by 2 complex matrix links the input and

output current and voltages, respectively U_n, I_n and U_{n+1}, I_{n+1}:

$$\begin{pmatrix} U_{n+1} \\ I_{n+1} \end{pmatrix} = T_i \cdot \begin{pmatrix} U_n \\ I_n \end{pmatrix} \tag{B.1}$$

Applying this to Figure B.1(b) gives following transfer matrix B.1 of the i^{th} cell:

$$T_i = \begin{pmatrix} 1 + Z_i Y_i & -\frac{Z_i^2 Y_i + 2Z_i}{2} \\ -2Y_i & 1 + Z_i Y_i \end{pmatrix} \tag{B.2}$$

The admittance and impedance for the HP unit cell are given by:

$$Z_i = \frac{1}{i\omega C_{r,i}} + i\omega L_{r,i} \tag{B.3}$$

$$Y_i = \frac{1}{i\omega L_{l,i}} \tag{B.4}$$

And in case of the LP unit cell:

$$Z_i = i\omega L_{r,i} \tag{B.5}$$

$$Y_i = \frac{1}{i\omega L_{l,i} + \frac{1}{i\omega C_{l,i}}} \tag{B.6}$$

With $C_{r,i}$ and $C_{l,i}$ the ring and leg capacitance, $L_{l,i}$ and $L_{r,i}$ the leg and end-ring effective inductance. Those are all for the i_{th} unit cell and ω is the angular frequency.

The phase shift $\delta\varphi_i$ corresponds to the eigenvalues of matrix T_i [6] given in equation B.2:

$$\delta\varphi_i = cos^{-1}(1 + Z_i Y_i) \tag{B.7}$$

This provides the phase of the nodes of the unit cells. Besides this, the amplitude and phase of the current on the legs I_n^l are also important parameters. Indeed, they generate the magnetic field and can be derived from the current on rings I_n^r and I_{n+1}^r:

$$I_n^l = I_{n+1}^r - I_n^r \tag{B.8}$$

Assuming a different phase for each rung, it becomes:

$$I_n^l = e^{i\varphi_{n+1}} - e^{i\varphi_n} = 2ie^{i\frac{\varphi_{n+1}+\varphi_n}{2}} sin\left(\frac{\varphi_{n+1} + \varphi_n}{2}\right) \tag{B.9}$$

The Bloch impedance is obtained from eigenvector analysis [6] of the transfer matrix and characterizes the unit cell. It is the ratio between voltage and current at the nodes, and is identical for each cell. This is the result of the symmetry of the Birdcage. The impedance is expressed as follows:

$$Z_b^i = \frac{1}{2}\sqrt{Z_i^2 + \frac{2Z_i}{Y_i}} \tag{B.10}$$

The condition of identical unit cells is important. This way reflections of the progressive mode are avoided between the unit cells. Therefore cells should be made identical.

Nikulin ends this approach by giving solutions of leg inductance and ring capacitance for HP cells [34]:

$$L_l = \frac{4Z_b^2(1 - cos\phi) - 2L_r Z_b |sin\phi|\omega}{2Z_b|sin\phi|(1 - cos\phi)\omega - L_r sin^2\phi^2} \tag{B.11}$$

$$C = \frac{L_r(cos\phi + 1)\omega - 2Z_b|sin\phi|}{L_r^2(cos\phi + 1)\omega^3 + Z_b^2(4cos\phi - 4)\omega} \tag{B.12}$$

He then concludes that *"Consequently, to keep the same impedance but varying the phase shift, one has not only to change the capacitance but also change the leg inductance, i.e., the width of the legs."*

Bibliography

[1] Sheikh Faisal Ahmad, Young Cheol Kim, Ick Chang Choi, and Hyun Deok Kim. Recent Progress in Birdcage RF Coil Technology for MRI System. *Diagnostics*, 10(12), 2020.

[2] Enzo Barberi, Sabiha Gati, Brian Rutt, and Ravi Menon. A transmit-only/receive-only (TORO) RF system for high-field mri/mrs applications. pages 284 – 289, 02 2000.

[3] J Martin Bland and Douglas G Altman. Statistics notes: Measurement error. *BMJ*, 312(7047):1654, 1996.

[4] F. Bloch. Nuclear Induction. *Phys. Rev.*, 70:460–474, Oct 1946.

[5] H.M. Borsboom, T. Claasen-Vujčić, and H.J.G. Gaykema. Low-frequency quadrature mode birdcage resonator. *MAGMA*, 5:33–37, 1997.

[6] Christophe Caloz and Tatsuo Itoh. *TL Theory of MTMs*, chapter 3, pages 59–132. John Wiley Sons, Ltd, 2005.

[7] Chih-Liang Chin, Christopher Collins, Shizhe Li, Bernard Dardzinski, and Michael Smith. BirdcageBuilder: Design of Specified-Geometry Birdcage Coils with Desired Current Pattern and Resonant Frequency. *Concepts in Magnetic Resonance*, 15:156 – 163, 06 2002.

[8] C. Craeye and David González-Ovejero. A review on array mutual coupling analysis. *Radio Science*, 46(2), April 2011.

[9] Christophe Craeye, Chan-Sun Park, Denis Tihon, and et. al. improved birdcage antenna. https://dial.uclouvain.be/pr/boreal/fr/object/boreal2021.

[10] Xavier Dardenne. *Method of Moments Simulation of Infinite and Finite Periodic Structures and Application to High-Gain Metamaterials Antennastt.* PhD thesis, March 2007.

[11] Nicholas De Zanche. Birdcage Volume Coil Design. *eMagRes ONLINE or Encyclopedia of Magnetic Resonance*, December 2011.

[12] Marc Dubois, Lisa Leroi, Zo Raolison, Redha Abdeddaim, Tryfon Antonakakis, Julien de Rosny, Alexandre Vignaud, Pierre Sabouroux, Elodie Georget, Benoit Larrat, Gérard Tayeb, Nicolas Bonod, Alexis Amadon, Franck Mauconduit, Cyril Poupon, Denis Le Bihan, and Stefan Enoch. Kerker Effect in Ultrahigh-Field Magnetic Resonance Imaging. *Phys. Rev. X*, 8:031083, Sep 2018.

[13] M Arcan Erturk, Xiufeng Li, Pierre-Francois Van de Moortele, Kamil Ugurbil, and Greg Metzger. Evolution of uhf body imaging in the human torso at 7t: Technology, applications, and future directions. *Topics in Magnetic Resonance Imaging*, 28:101–124, 06 2019.

[14] GE Healthcare Systems | GE Healthcare.

[15] Christophe Geuzaine and Jean-François Remacle. Gmsh: A 3-D Finite Element Mesh Generator with Built-in Pre- and Post-Processing Facilities. *International Journal for Numerical Methods in Engineering*, 79:1309 – 1331, 09 2009.

[16] Frederick W.´ Grover. Dover Phoenix Edition, 2015.

[17] Axel Haase, Florian Odoj, Markus Von Kienlin, Jan Warnking, Florian Fidler, Alexander Weisser, Mathias Nittka, Eberhard Rommel, Titus Lanz, Bernhard Kalusche, and Mark Griswold. NMR probeheads for in vivo applications. *Concepts in Magnetic Resonance*, 12(6):361–388, 2000.

[18] Cecil E. Hayes. The development of the birdcage resonator: A historical perspective. *NMR in biomedicine*, 22, 11 2009.

[19] Cecil E. Hayes, William A. Edelstein, John F. Schenck, Otward M. Mueller, and Matthew Eash. An efficient, highly homogeneous radiofrequency coil for whole-body NMR imaging at 1.5 T. *Journal of Magnetic Resonance (1969)*, 63(3):622–628, 1985.

[20] Konstantin Huhn, Tobias Engelhorn, Ralf Linker, and Armin Nagel. Potential of Sodium MRI as a Biomarker for Neurodegeneration and Neuroinflammation in Multiple Sclerosis. *Frontiers in Neurology*, 10:84, 02 2019.

[21] John David Jackson and John Wiley. *Classical Electrodynamics Third Edition.* Technical report, 1998.

[22] Young Kim, Hyun Kim, Byoung-Ju Yun, and Sheikh Faisal Ahmad. A Simple Analytical Solution for the Designing of the Birdcage RF Coil Used in NMR Imaging Applications. *Applied Sciences*, 10:2242, 03 2020.

[23] D. Klomp, M. van der Graaf, and M. Willemsen. Transmit/receive headcoil for optimal H MR spectroscopy of the brain in paediatric patients at 3 T. *MAGMA*, 17:1–4, 2004.

[24] ML Lauzon. A Beginner's Guide to Bloch Equation Simulations of Magnetic Resonance Imaging Sequences, 2020.

[25] IntechOpen Limited. Metamaterials in application to improve antenna parameters.

[26] Loop Coils - Siemens Healthineers Global.

[27] M. Lupu, J. Dimicoli, and A. Volk. An efficient design for birdcage probes dedicated to small-animal imaging experiments. *MAGMA*, 17:333–371, 2004.

[28] M-One. Metamaterial head coil for ultra-high field MRI.

[29] Xianglun Mao. PARALLEL TRANSMISSION (PTX) TECHNIQUES AND APPLICATIONS ON A TRANSCEIVER COIL ARRAY IN HIGH-FIELD MRI. 10 2019.

[30] Joël Mispelter and Mihaela Lupu. Homogeneous resonators for magnetic resonance: A review. *Comptes Rendus Chimie*, 11(4):340–355, 2008.

[31] Joël Mispelter, Mihaela Lupu, and André Briguet. *NMR probeheads for biophysical and biomedical experiments theoretical principles practical guidelines.* Imperial College Press ; Distributed by World Scientific, London : Hackensack, NJ, 2nd ed. edition, 2015.

[32] O. C. Morse and J. R. Singer. Blood Velocity Measurements in Intact Subjects. *Science*, 170(3956):440–441, 1970.

[33] MRI RF Coils | Bruker.

[34] Anton Nikulin. *Volume RF coils based on metamaterials for ultra-high field magnetic resonance imaging.* PhD thesis, 10 2020.

[35] R. Pascone, T. Vullo, J. Farrelly, and PT. Cahill. Explicit treatment of mutual inductance in eight-column birdcage resonators. Magn Reson Imaging. 10(3):401 – 410, 1992.

[36] Frank Peeters. Lecture notes in Medical imaging - LGBIO2050, October-December 2021.

[37] J.B. Pendry, A.J. Holden, D.J. Robbins, and W.J. Stewart. Low frequency plasmons in thin-wire structures. *J.Phys Condens. Matter*, 10:4785–4809, 1998.

[38] J.B. Pendry, A.J. Holden, D.J. Robbins, and W.J. Stewart. Magnetism from conductors and enhanced nonlinear phenomena. *IEEE Transactions on Microwave Theory and Techniques*, 47(11):2075–2084, Nov 1999.

[39] Rolf Pohmann, Oliver Speck, and Klaus Scheffler. Signal-to-noise ratio and MR tissue parameters in human brain imaging at 3, 7, and 9.4 tesla using current receive coil arrays. *Magnetic Resonance in Medicine*, 75, 2016.

[40] Xavier Radu. *Metamaterial devoted to magnetic resonance imaging : numerical analysis and experimental validation.* PhD thesis, October 2009.

[41] Kazem Sabet. Basic principles of the method of moments.

[42] Huettel Scott A. and Songand Gregory McCarthy Allen W. Functional Magnetic Resonance Imaging. *The Yale Journal of Biology and Medicine*, 82(4):233, 2009.

[43] Vladimir M. Shalaev. Optical negative-index metamaterials. *Nature Photon*, 1:41–48, January 2007.

[44] RA Shelby, D Smith, and S Schultz. Experimental verification of a negative index of refraction. *Science (New York, N.Y.)*, 292, 05 2001.

[45] D. R. Smith, Willie J. Padilla, D. C. Vier, S. C. Nemat-Nasser, and S. Schultz. Composite Medium with Simultaneously Negative Permeability and Permittivity. *Phys. Rev. Lett.*, 84:4184–4187, May 2000.

[46] Daniel Speicher, T. Bartscherer, F.J. Becker, J.W. Jenne, K. Mrosk, C. Degel, M. Günther, and S. Tretbar. MRI Compatible Ultrasound Transducers for Simultaneous Acquisition of Coregistered Ultrasound to MRI Data. *Physics Procedia*, 70:1002–1006, 2015. Proceedings of the 2015 ICU International Congress on Ultrasonics, Metz, France.

[47] Anja van der Kolk, Jeroen Hendrikse, Jaco Zwanenburg, Fredy Visser, and Peter Luijten. Clinical applications of 7 T MRI in the brain. *European journal of radiology*, 82, 09 2011.

[48] J.T. Vaughan, M. Garwood, C.M. Collins, W. Liu, L. DelaBarre, G. Adriany, P. Andersen, H. Merkle, R. Goebel, M.B. Smith, and K. Ugurbil. 7T vs. 4T: RF power, homogeneity, and signal-to-noise comparison in head images. *Magnetic Resonance in Medicine*, 46(1):24–30, 2001.

[49] J.T. Vaughan and John R. Griffiths. *RF coils for MRI.* Wiley, 2012.

[50] Viktor G. Veselago. The electrodynamics of substance with simultaneously negative values of ϵ and μ. *Soviet physics uspekhi*, 10(4):509–514, 1958.

[51] Dwight Vincent, Tianhao Wang, Thalia Magyar, Peni Jacob, Richard Buist, and Melanie Martin. Birdcage volume coils and magnetic resonance imaging: A simple experiment for students. *Journal of Biological Engineering*, 11, 11 2017.

[52] A.G. Webb. Dielectric materials in magnetic resonance. *Concepts in Magnetic Resonance Part A*, 38A(4):148–184, 2011.

UNIVERSITÉ CATHOLIQUE DE LOUVAIN
École polytechnique de Louvain
Rue Archimède, 1 bte L6.11.01, 1348 Louvain-la-Neuve, Belgique | **www.uclouvain.be/epl**